



ulm university universität
uulm

**Fakultät für
Naturwissenschaften**

Institute of Theoretical
Physics

The Effects of Casimir Interactions in Experiments on Gravitationally-induced Entanglement

Bachelor Thesis

Submitted by:

Jan Bulling
jan.bulling@uni-ulm.de
1109395

Supervised by:

Marit O. E. Steiner, Julen S. Pedernales, Martin B. Plenio

Name: Jan Bulling

Matriculation number: 1109395

Declaration

I hereby declare that I wrote this bachelor thesis independently and used no other aids than those cited. The passages in the thesis that are taken from other works in terms of wording or meaning have been identified by stating the source.

December 18, 2024

Jan Bulling

Acknowledgements

First and foremost, I would like to thank Martin Plenio for giving me the opportunity to conduct my bachelor's thesis at his institute and to be part of a cutting-edge research group. The topic he provided me with for my thesis was very interesting and I really enjoyed working on it.

I would also like to thank my supervisors, Julen and Marit, for their guidance, support, and dedication throughout my project. They were both always there for me - right up to the last days - and were eager to help me with any questions I had. During my time at the institute, I not only gained a deeper understanding of physics from them but also valuable insights that extended beyond the academic realm. Thank you for making this journey possible.

Abstract

The quantum nature of gravity remains an unresolved question in modern physics, despite significant advances in both quantum theory and general relativity. The detection of gravitational entanglement between two massive particles has recently been considered a crucial step towards establishing the non-classical nature of gravity. To realize this, some theoretical proposals suggest using solids in the nano- and microscale regime interacting purely gravitationally in a controlled laboratory setup. Often considered configurations place the center-of-mass of each particle in a Schrödinger-cat-like state, which results in the generation of entanglement between the positional degrees of freedom of the interacting particles. In this approach, it is generally desired to place the masses as close as possible in order to enhance their gravitational coupling. To mitigate unwanted entanglement caused by electromagnetic interactions, such as short-range Casimir interactions at close particle separation, the use of a conductive Faraday shield between the masses has been proposed. This work investigates the impact of Casimir forces arising between the particles and the newly introduced shield on entanglement generation. It is shown that stochastic variations in the initial placement of the particles over multiple experimental runs can destroy measurable entanglement. In addition, the effects of thermal vibrations of the Faraday shield are analyzed, providing important insights into experimental feasibility and requirements. These results contribute to ongoing efforts in designing realistic experiments that probe the quantum nature of gravity.

Contents

1	Introduction	7
2	A first look	8
2.1	Time evolution under a gravitational potential	11
2.2	Entanglement measures	12
2.3	Issues with the idealized experimental procedure	16
3	Casimir effect	18
3.1	Proximity force approximation	20
3.2	Casimir forces between a conducting plate and a dielectric sphere	22
3.3	Imperfect surfaces of the plate and the sphere	25
4	The particle in front of a static shield	28
4.1	Entanglement generation	31
4.2	The optimal setup	36
4.2.1	Orientation	36
4.2.2	Separation, mass and superposition size	42
4.3	Trapping the particle	45
4.4	Discussions	47
5	The consequences of a thermal shield	51
5.1	Thickness and size of the shield	51
5.1.1	Shielding Coulomb-Interactions	52
5.1.2	Shielding Casimir-Interactions	54
5.1.3	Gravitational effects of the shield	55
5.2	Thermal shield vibrations	55
5.3	Entanglement in front of a thermal shield	58
5.3.1	Analytic dynamics	62
5.3.2	Small shields	67
5.4	Discussions of the effects of the thermal shield	68
6	Discussion and outlook	70
	Bibliography	73
A	Ancillary calculations	80
A.1	Evolution under a gravitational Hamiltonian	80

Contents

A.2	Exemplary calculation of E_N	81
A.3	Polarizability of a dielectric sphere	82
A.4	Blocking of the shield	82
A.5	Thermal harmonic oscillator	84
B	Primary calculations	85
B.1	Entanglement in different orientations	85
B.2	Density matrix with stochastic placement variations	86
B.3	Density matrix for particles in front a vibrating plate	88
B.4	Time evolution of two particles in front of a thermal plate	89
C	Additional figures	91

1 Introduction

Understanding nature’s weakest fundamental force - gravity - has been a persistent challenge ever since Newton formulated the laws of gravitational force in 1687 [1]. Newton’s equations were groundbreaking, providing unprecedented accuracy in predicting planetary motion and establishing mathematics as the universal language of physical description. In 1774, Maskelyne conducted the first measurement of gravitational attraction between objects other than astronomical bodies, solidifying the concept of the interaction of masses across multiple orders of magnitude [2, 3]. Cavendish measured the gravitational constant G using a torsion pendulum in 1798, providing the first quantitative determination of the weak gravitational coupling [4]. Einstein revolutionized our understanding of gravity with his theory of general relativity, offering a geometric interpretation of spacetime [5]. Yet, the fundamental nature of gravity remains elusive. Whether gravity is purely classical or fundamentally quantum is one of the most pressing and debated questions in modern physics and many different theories for unifying general relativity and quantum mechanics have emerged [6–8]. The extraordinary success of quantum field theory for electromagnetic, weak, and strong interactions suggests that gravity may also have a quantum foundation.

Building on Feynman’s ideas from 1957 [9, 10], several subsequent works [11–14] have proposed searching for gravitationally induced entanglement as a key signature of the quantum nature of gravity that would experimentally establish the necessity for a new theory of gravity. Advances in quantum optomechanics have led to several recent experimental proposals [15–17], that outline concrete roadmaps for conducting such experiments e.g. with levitated nanoparticles. In chapter 2 of this thesis, the arguments and assumptions behind these proposals are discussed and the general experimental setup is explained. A useful framework of later employed methods is outlined. The necessity of a Faraday shield in the experiments is explained as well as potential occurring issues due to Casimir interactions [18] between the introduced shield and the particles. Chapter 3 introduces the Casimir force and establishes approximation models for short- and long-range interactions. The effect of rough and uneven surfaces is studied.

The decoherence effect and the consequent loss of entanglement caused by stochastic variations in the experimental initialization are analyzed in-depth in chapter 4. Potential modifications in the setup and the proposed parameter-space as well as the ability to trap and levitate the particles close to the shield is discussed. Chapter 5 estimates the required size and thickness of the Faraday shield to sufficiently suppress unwanted interactions between the masses. Additionally, effects of thermal vibrations of the shield on entanglement generation are calculated and analyzed.

2 A first look

Testing the quantum nature of gravity is no easy task and many proposals seek to detect gravitationally induced entanglement between two masses [15–17, 19, 20] as a form of proof. For all these proposals, gravity is assumed to be mediated by a gravitational field - either classical, described by the metric tensor in general relativity or by a quantum entity. During a time evolution, this field (like any other external field) can only perform local operations (LO) on the states of the test masses. This has repeatedly been seen in different experiments like in the observation of the gravitational Aharonov-Bohm effect [21] or in gravitationally induced quantum interference with neutrons influenced by earth’s gravitational field [22]. If gravity is now assumed to behave classically, its propagation between masses can be described by a classical communication (CC) channel [23]. These LOCC operations however cannot turn an initially unentangled state into an entangled one [24, 25]. It immediately follows, that if one measures the involved masses to be entangled after a mutual gravitational interaction, gravity necessarily has to be non-LOCC in some way. Whether this directly implies the *quantum nature of gravity* is a hot topic of debate [26]. It is important to note, that the opposite of this statement is not true. Measuring unentangled masses does not directly imply the classicality of the gravitational field. This can be seen by considering operations that are non-LOCC and also produce unentangled states like for example the swap operation $|\psi\rangle_A |\phi\rangle_B \rightarrow |\phi\rangle_A |\psi\rangle_B$. This operation obviously can’t induce entanglement to initially unentangled states, but requires the exchange of quantum information between them - which is not possible using classical communication alone. In other words: If one prepares masses initially in a pure product state and measures *any* state which cannot be obtained by LOCC-operations after some finite time evolution, it is impossible for gravity to be classical. One can even go so far and define the term ***quantum gravity*** as any interaction mediated by gravity, that cannot be described by LOCC operations alone [23].

A plausible and logical idea for an experiment to test for gravitationally induced entanglement was suggested by Feynman during a discussion session at the 1957 “Conference on the Role of Gravitation in Physics” at Chapel Hill, North Carolina [9, p. 247-260] and is described in this chapter. It requires the generation of coherent quantum superpositions of the center-of-mass degree of freedom for two massive objects either in so-called Schrödinger-cat states or squeezed gaussian states [15, 27]. Both masses are separated by a small distance L such that gravity has a notable effect after a set time. Ignoring non-gravitational couplings, the mutual gravitational interaction should entangle the masses - of course only *if gravity behaves quantum*. There exist criticizing arguments,

that entanglement generation does not strictly require a quantum nature of gravity and other classical mechanisms could induce entanglement as well [28]. In the low energy limit $E \lesssim m_p c^2 \sim 10^{19}$ GeV and for close separations, the gravitational interaction can be described by an instantaneous Newtonian $1/r$ potential acting on the center-of-mass positions [27, 29, 30]. Spatial superpositions lead to superpositions of the metric and consequently - in the non-relativistic limit - to a superposed Newtonian potential. The interaction Hamiltonian \hat{H}_G is described by

$$\hat{H}_G = -\frac{Gm^2}{|L - (\hat{x}_A - \hat{x}_B)|}, \quad (2.1)$$

where $G = 6.6743 \times 10^{-11} \text{ m}^3 \text{ kg}^{-1} \text{ s}^{-2}$ is the gravitational constant. The positions x_A and x_B of the both masses A and B have been canonically quantized. The particles are initially delocalized in the spatial cat-states $|\psi\rangle = 1/\sqrt{2} (|\psi^{(1)}\rangle + |\psi^{(2)}\rangle)$. If $L \gg |\hat{x}_A - \hat{x}_B|$, the denominator of \hat{H}_G can be expanded up to second order in $\hat{x}_A - \hat{x}_B$. In this thesis, L will be in the $10 \mu\text{m}$ regime and the spatial extension Δx is around 500 nm [31], making this expansion always justified. The zeroth order term is just an overall energy offset, the first order term $\propto (\hat{x}_A - \hat{x}_B)$ as well as the terms \hat{x}_i^2 result only in a local interaction for each mass separately. The coupling term $-(\hat{x}_A \hat{x}_B + \hat{x}_B \hat{x}_A) = -2\hat{x}_A \hat{x}_B$ however couples both masses and thus can mediate entanglement. An exemplary calculation of this is demonstrated in appendix A.1.

The observable entanglement is however very weak as it depends on the gravitational coupling strength $\sim G$ and thus, typically coherence times in order of 100 ms to 100 s are required, imposing a huge experimental challenge. As will be shown in the next section the entanglement rate between two massive particles increases with the spatial width of the wave functions Δx and their mass M . To contextualize: The most massive object ever put into a spatial superposition in matter-wave interferometry is in the order of $4 \times 10^{-23} \text{ kg}$ [31] whereas the smallest object whose gravitational field has been measured was just below 100 mg [32] - a difference of 19 orders of magnitude. Levitated particles pose a promising platform for bridging this gap: As the name suggests, the test masses are levitated and are therefore well-decoupled from their environment in ultra high vacuums, where even collisions with single air molecules can be prevented. Furthermore, there are multiple proposals on how to prepare the spatial superpositions required experimentally [15–17]. One possibility is to use spin degrees of freedoms in a Stern-Gerlach apparatus with a magnetic field gradient [15]. Alternatively, a 1D harmonic potential [17] or a double-well potential can be used for trapping levitated particles and ground-state cooling can create spatially delocalized states. In this thesis, it is assumed that all required states and superpositions can be prepared experimentally.

One of the most prominent proposals to test gravity for quantum features is described in Ref. [15] and is depicted in fig. 2.1. Two massive bodies with masses M_A and M_B are initially separated by a center-to-center distance $2L$. The masses are prepared in a coherent delocalized quantum superposition of Schrödinger-cat-like states in an orientation, where they are perfectly parallel to each other as seen in fig. 2.1. The spatial

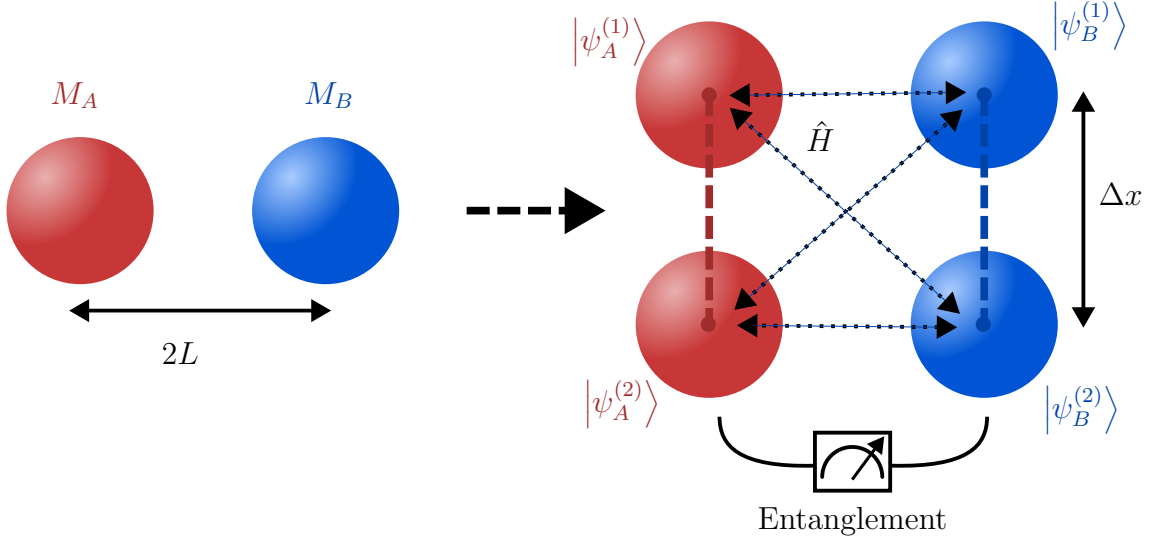


Figure 2.1: Schematic figure of the proposed experiment with two masses prepared in a spatial superposition state. The gravitational interaction \hat{H} induces different phases to each of the superpositions due to the different distances between all masses. This results in measurable entanglement after some time evolution.

extension size of the superposition is denoted by Δx . With the notation introduced in fig. 2.1, the initial state at $t = 0$ is given by

$$|\psi(t=0)\rangle = \frac{1}{2} \left(|\psi_A^{(1)}\rangle + |\psi_A^{(2)}\rangle \right) \otimes \left(|\psi_B^{(1)}\rangle + |\psi_B^{(2)}\rangle \right). \quad (2.2)$$

The state evolves under a Hamiltonian \hat{H}_G and after some time the position of each mass is measured and checked for entanglement. For now it is assumed that all other interactions except gravity are negligible. In reality, electromagnetic forces and Casimir-Polder interactions [18, 33] need to be considered. On the time scales of the experiment, the acceleration of the masses due to the mutual gravitational attraction can be neglected¹. Therefore, the gravitational potential can be assumed to be static and $|L - (\hat{x}_A - \hat{x}_B)|$ can be replaced by the distance operator \hat{L}

$$\hat{V} = -\frac{GM_A M_B}{|\hat{L}|}. \quad (2.3)$$

\hat{L} represents the separation between two states $|\psi_A^{(i)}\rangle$ and $|\psi_B^{(j)}\rangle$ ($i, j = 1, 2$) and acts on the state $|\psi_A^{(i)}\rangle \otimes |\psi_B^{(j)}\rangle$ like $\hat{L} |\psi_A^{(i)}\psi_B^{(j)}\rangle = 2L^{(ij)} |\psi_A^{(i)}\psi_B^{(j)}\rangle$ with $2L^{(ij)}$ being the distance

¹Take for example a silica sphere ($\rho = 2648 \text{ kg/m}^3$) with $R = 10^{-5} \text{ m}$ separated by $2L = 4R$. The mutual gravitational acceleration for each sphere is around $a = GM/(2L)^2 = 5 \times 10^{-13} \text{ m/s}^2$ which, for $t \sim 1 \text{ s}$, results in a displacement of $\sim 10^{-13} \text{ m}$ which is much smaller than typical variances of the ground state $\Delta x \sim 100 \text{ nm}$ [31].

between the associated cat-states. During time evolution, the different parts of the superpositions build up different local phases according to their separation distance. In the following section, the time evolution of the state in eq. (2.2) under this Newtonian potential will be analyzed.

2.1 Time evolution under a gravitational potential

The time evolution of a quantum system is governed by the Schrödinger equation

$$i\hbar \frac{\partial}{\partial t} |\psi(t)\rangle = \hat{H} |\psi(t)\rangle \quad (2.4)$$

where in this case the interaction Hamiltonian responsible for the entanglement dynamics is given by $\hat{H} = \hat{V}$ in eq. (2.3). The eigenbasis of \hat{V} is given by $\{|\psi_A^{(1)}\rangle, |\psi_A^{(2)}\rangle\} \otimes \{|\psi_B^{(1)}\rangle, |\psi_B^{(2)}\rangle\}$, as all these states are eigenstates of the distance operator \hat{L}

$$\hat{V} |\psi_A^{(i)}\rangle \otimes |\psi_B^{(j)}\rangle = -\frac{GM_A M_B}{2L^{(ij)}} |\psi_A^{(i)}\rangle \otimes |\psi_B^{(j)}\rangle. \quad (2.5)$$

The Schrödinger equation for the diagonal Hamiltonian \hat{H} can be directly solved for the initial state eq. (2.2) with the solution given by

$$|\psi(t)\rangle = \frac{1}{2} \sum_{i,j \in \{1,2\}} \exp\left\{\frac{i}{\hbar} \frac{GM_A M_B}{2L^{(ij)}} t\right\} |\psi_A^{(i)} \psi_B^{(j)}\rangle \quad (2.6)$$

where the tensor product \otimes was omitted. It is possible to express the state using the dynamically accumulated phases $\phi^{(ij)}$ which build-up after a mutual interaction as

$$|\psi(t)\rangle = \frac{1}{2} \left(e^{i\phi^{(11)}} |\psi_A^{(1)} \psi_B^{(1)}\rangle + e^{i\phi^{(12)}} |\psi_A^{(1)} \psi_B^{(2)}\rangle + e^{i\phi^{(21)}} |\psi_A^{(2)} \psi_B^{(1)}\rangle + e^{i\phi^{(22)}} |\psi_A^{(2)} \psi_B^{(2)}\rangle \right). \quad (2.7)$$

The phases $\phi^{(ij)}$ in the specific setup shown in fig. 2.1 are given by

$$\phi \equiv \phi^{(11)} = \phi^{(22)} = \frac{GM_A M_B}{2\hbar L} t \quad \text{and} \quad \phi^{(12)} = \phi^{(21)} = \frac{GM_A M_B}{\hbar \sqrt{4L^2 + (\Delta x)^2}} t. \quad (2.8)$$

By expanding the phases for small superposition sizes $\Delta x \ll L$, the global phase ϕ can be factored out of the evolved state

$$\phi^{(12)} = \phi^{(21)} \approx \frac{GM_A M_B}{\hbar} \left[\frac{1}{2L} - \frac{(\Delta x)^2}{16L^3} \right] t \equiv \phi - \Delta\phi, \quad (2.9)$$

which ultimately can be written in the form

$$|\psi(t)\rangle = e^{i\phi} \frac{1}{\sqrt{2}} \left[|\psi_A^{(1)}\rangle \otimes \frac{|\psi_B^{(1)}\rangle + e^{-i\Delta\phi} |\psi_B^{(2)}\rangle}{\sqrt{2}} + |\psi_A^{(2)}\rangle \otimes \frac{e^{-i\Delta\phi} |\psi_B^{(1)}\rangle + |\psi_B^{(2)}\rangle}{\sqrt{2}} \right]. \quad (2.10)$$

It can be seen that in general, the resulting state is not expressible as a product state, hence it is entangled. This is of course only the case, if $\Delta\phi \neq k\pi$, $k \in \mathbb{N}$.

In order to assess quantitatively how entangled the state $|\psi(t)\rangle$ is after time t , a more sophisticated measure is required. One possible measure is the “logarithmic negativity”, which is introduced in the next section and used in the rest of this work.

2.2 Entanglement measures

Checking whether an arbitrary state ρ is entangled or not is no easy task. In fact, this problem is known to be NP-hard [34]. A state $\rho_{AB} \in \mathcal{H}_A \otimes \mathcal{H}_B$ is called entangled, if it is **non-separable**, that is, it cannot be expressed as a tensor product of two subsystems $\rho_A \in \mathcal{H}_A$ and $\rho_B \in \mathcal{H}_B$. Only for specific cases - like the case of two qubits or qubit-qutrit - a simple sufficient criterion for determining the separability of a general mixed state is known: The positive partial transpose (PPT) criterion states, that if the partial transpose of the density matrix is positive ($\rho^{\Gamma_A} \geq 0$)², the state ρ is separable [24, 25]. In other words, if ρ^{Γ_A} has negative eigenvalues, ρ is guaranteed to describe an entangled state. The inverse is true, if and only if the dimension of $\rho_A \otimes \rho_B$ is 2×2 or 3×2 [24] - otherwise, only having non-negative eigenvalues doesn't necessarily result in an unentangled system. The partial transpose with respect to a subsystem i can be understood in the same way as the partial trace, where the operation (in this case the transform) is performed only on indices corresponding the subsystem ρ_i . It is defined for an arbitrary density matrix $\rho = \sum_{ijkl} p_{kl}^{ij} |i\rangle\langle j| \otimes |k\rangle\langle l|$ as $\rho^{\Gamma_A} = \sum_{ijkl} p_{kl}^{ji} |i\rangle\langle j| \otimes |k\rangle\langle l|$. To see the necessity of the PPT criterion, consider a separable mixed state ρ , which can be generally expressed as

$$\rho = \sum p_i \rho_A^{(i)} \otimes \rho_B^{(i)}. \quad (2.11)$$

The partial transpose is in this case trivial:

$$\rho^{\Gamma_A} = \sum p_i (\rho_A^{(i)})^T \otimes \rho_B^{(i)}. \quad (2.12)$$

Since the transpose preserves eigenvalues, the transposed subsystem A is still positive, $(\rho_A^{(i)})^T \geq 0$, and describes again a valid quantum state. It follows, that ρ^{Γ_A} is positive as well. If somehow ρ^{Γ_A} has any negative eigenvalues, this can only mean that the initial state ρ is not separable and cannot be expressed in the form of eq. (2.11) and the necessity of the criterion is shown.

For quantifying entanglement in a more precise way, a sophisticated **entanglement measure** can be used. A good measure should be able to capture the essential features of entanglement. One can axiomatically state what properties such a measure $E(\rho)$ should have [24, 25]:

²An $n \times n$ hermitian matrix M is defined as positive (“positive semi-definite”), if $\mathbf{z}^* M \mathbf{z} \geq 0$ for all $\mathbf{z} \in \mathbb{C}^n \setminus \{0\}$; i.e. if and only if all eigenvalues are non-negative.

Normalization An entanglement measure should be a map from a state to a positive real number:

$$\rho \rightarrow E(\rho) \geq 0 \quad (2.13)$$

where usually the maximally entangled state has $E = 1$.

Monotonicity under LOCC E should not increase under local operations and classical communications. This is the most important postulate for an entanglement measure and often cited as the *only* required postulate.

Vanishing on separable states $E(\rho) = 0$ if ρ is separable.

Often one finds additional properties useful like *convexity* $E(\sum p_i \rho_i) \leq \sum p_i E(\rho_i)$ or (full) *additivity* $E(\rho \otimes \sigma) = E(\rho) + E(\sigma)$.

A function that satisfies these conditions is often called an *entanglement monotone*.

The **negativity** \mathcal{N} is such an entanglement monotone [25, 35] that uses the PPT criterion to determine if a state is entangled or not. It is defined as

$$\mathcal{N} = \frac{\|\rho^{\Gamma_A}\|_1 - 1}{2} \quad (2.14)$$

where $\|A\|_1 = \text{tr} |A| = \text{tr} \sqrt{A^\dagger A}$ is the trace norm. The negativity however is not additive and a more universally applicable and widely used entanglement measure is the **logarithmic negativity** [36]

$$E_N(\rho) = \log_2 \|\rho^{\Gamma_A}\|_1. \quad (2.15)$$

The monotonicity of the logarithm implies that E_N is an entanglement monotone as well. Furthermore, it is noteworthy, that $\|\rho^{\Gamma_A}\|_1 = \|\rho^{\Gamma_B}\|_1$ as will be shown below. Therefore, the logarithmic negativity is symmetric under exchange of the subsystem.

Proposition 2.1. a) The partial transpose w.r.t. subsystem A is equal to the transposed partial transpose w.r.t. subsystem B : $\rho^{\Gamma_A} = (\rho^{\Gamma_B})^T$. b) The trace norms of partially transposed density operators w.r.t. any subsystem are equal: $\|\rho^{\Gamma_A}\|_1 = \|\rho^{\Gamma_B}\|_1$.

Proof. a) A general density matrix ρ can be expressed as

$$\rho = \sum_{i,j,k,l} \rho_{ij,kl} |i\rangle\langle j|_A \otimes |k\rangle\langle l|_B.$$

The partial transpose with respect to subsystem B is then defined as

$$\rho^{\Gamma_B} \equiv \sum_{i,j,k,l} \rho_{ij,kl} |i\rangle\langle j|_A \otimes (|k\rangle\langle l|_B)^T = \sum_{i,j,k,l} c_{ij,kl} |i\rangle\langle j|_A \otimes |l\rangle\langle k|_B.$$

The complete transpose of this is

$$(\rho^{\Gamma_B})^T = \sum_{i,j,k,l} \rho_{ij,kl} (|i\rangle\langle j|_A)^T \otimes (|l\rangle\langle k|_B)^T = \sum_{i,j,k,l} c_{ij,kl} |j\rangle\langle i|_A \otimes |k\rangle\langle l|_B \equiv \rho^{\Gamma_A}.$$

b) Clear by a) and by using lemma 2.1 and the fact that the eigenvalues of a square matrix A and A^T are equal. \square

The logarithmic negativity is very easy to calculate compared to other entanglement measures. If the eigenvalues of ρ are known, the logarithmic negativity can be directly computed, as will be demonstrated below. Since this thesis focuses on low-dimensional 4×4 systems, single eigenvalues can be determined with low effort analytically as well as numerically with great stability.

Lemma 2.1. *The trace norm $\|A\|_1 \equiv \text{tr} \sqrt{A^\dagger A}$ of a hermitian matrix A is equal to the sum of the absolute eigenvalues of A .*

Proof. This can be immediately seen by the spectral decomposition $\lambda(A) = \{\lambda_1, \dots\}$ and the hermitian property $A^\dagger A = AA^\dagger = A^2$:

$$\text{tr} \sqrt{A^\dagger A} = \text{tr} \sqrt{A^2} = \text{tr} \left\{ U \sqrt{\text{diag}(\lambda_1, \dots)^2} U^\dagger \right\} = \sum_i \sqrt{\lambda_i^2} = \sum_i |\lambda_i|.$$

\square

Proposition 2.2. *The negativity eq. (2.14) is given as the absolute sum of all negative eigenvalues of ρ^Γ :*

$$\mathcal{N}(\rho) \equiv \frac{\|\rho^\Gamma\|_1 - 1}{2} = \left| \sum_{\lambda_i < 0} \lambda_i \right|. \quad (2.16)$$

Proof. The proof is in parts given by Vidal and Werner [35]. It is known that the density matrix is hermitian: $\rho = \rho^\dagger$. Using lemma 2.1, the trace norm of the density matrix is given as $\|\rho\|_1 = \sum \lambda_i = \text{tr} \rho = 1$. The partial transpose ρ^Γ obviously also satisfies $\text{tr} \rho^\Gamma = 1$ but might have negative eigenvalues. Since ρ^Γ is still hermitian, the trace norm is given by

$$\|\rho^\Gamma\|_1 = \sum_i |\lambda_i| = \sum_{\lambda_i \geq 0} \lambda_i + \sum_{\lambda_i < 0} |\lambda_i| = \sum_i \lambda_i + 2 \sum_{\lambda_i < 0} |\lambda_i| = 1 + 2 \sum_{\lambda_i < 0} |\lambda_i|,$$

where in the last step $\sum \lambda_i = \text{tr} \rho^\Gamma = 1$ was used. \square

Remark. The PPT criterion states, that if ρ^Γ has negative eigenvalues, the state ρ is entangled. The negativity uses this criterion for a quantification of entanglement. This motivates the name *negativity*.

Calculating the logarithmic negativity of the evolved state eq. (2.7), it is possible to quantify how the entanglement behaves in time. A straight forward computation following the calculation methods established above yields (for detailed calculations see appendix A.2)

$$E_N(|\psi(t)\rangle\langle\psi(t)|) = \log_2 (1 + |\sin \Delta\phi|). \quad (2.17)$$

As expected, the states are not entangled for $\Delta\phi = k\pi$, $k \in \mathbb{Z}$ and maximum entanglement $E_N = 1$ is reached for $\Delta\phi = 2\pi k \pm \pi/2$. This result aligns with the previous observations by demanding that the evolved state eq. (2.10) is separable. The complete entanglement dynamics are shown in fig. 2.2. Additionally, this figure depicts the en-

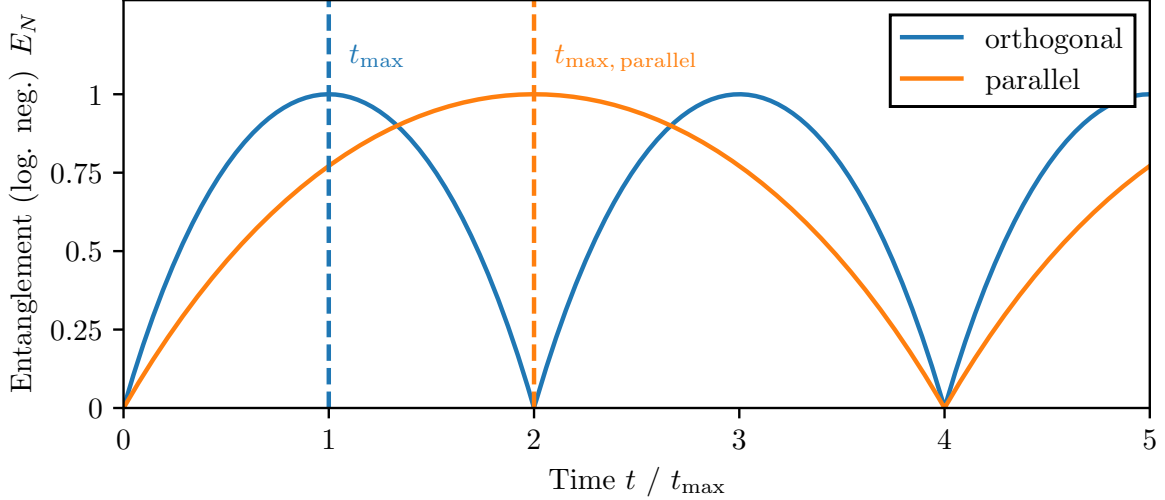


Figure 2.2: Entanglement dynamics quantified by the logarithmic negativity E_N for two different orientations of the spatial superpositions. The parallel orientation (**orange**) is shown in fig. 2.1 and the orthogonal orientation (**blue**) was taken from Ref. [27], where the cat-states are right-angled compared to the parallel configuration. The maximal amount of entanglement is reached after a time given by eq. (2.18) and for reasonable parameters this equates to $t_{\text{max, orthogonal}} \equiv t_{\text{max}} \approx 129$ ms.

tanglement generation in the “orthogonal orientation”, where both superpositions are aligned in a straight line right-angled to the previously used setup in fig. 2.1.

The time $t_{\text{max, parallel}}$ at which the states are maximally entangled for the first time, can be calculated by using the definition of $\Delta\phi$ from eq. (2.9) as

$$t_{\text{max, parallel}} = \frac{8\pi L^3 \hbar}{GM_A M_B (\Delta x)^2}. \quad (2.18)$$

In the orthogonal orientation, this point in time is reached twice as fast [27]. This is because in this orientation, the difference in distances between the cat-states is maximized and consequently the relative dynamical phase build-up is faster compared to the parallel orientation resulting in a faster entanglement rate.

This suggests, that the orthogonal orientation might be beneficial as it requires shorter coherence times. This effect is studied in more detail in section 4.2. To give an estimation of the coherence times needed, consider two identical silica nano-spheres with densities $\rho = 2648 \text{ kg/m}^3$ and radii $R = 10^{-5} \text{ m} = 10 \mu\text{m}$ separated by a distance $2L = 4R$.

The superposition size is in the order of 100 nm. The maximum entanglement in the parallel configuration is reached after a time $t_{\text{max, parallel}} \approx 258$ ms which is quite long and challenging experimentally considering that possible coherence times are currently only in the order of micro-seconds [37].

2.3 Issues with the idealized experimental procedure

For the practical realization of an experiment on measuring gravitationally induced entanglement of masses, other forms of direct or indirect interaction between the particles must be suppressed such that the measured entanglement ultimately arises only due to their gravitational interaction. In particular, the short-range **Casimir interactions** [18] discussed in chapter 3 have to be shielded as they exert a much greater attraction force on the particles at small separations than gravity. It is still a hot topic of discussions whether Casimir interactions can even entangle macroscopic bodies at all, as it is not even clear if it is a conservative force in the first place - although most researchers believe it is [38, 39]. To estimate the minimal particle-particle separation $2L$ while requiring that the gravitational interaction V_{Gravity} is stronger than the Casimir interactions V_{Casimir} [40] by a factor $\chi > 1$, the following inequality can be stated:

$$\chi |V_{\text{Casimir}}| \leq |V_{\text{Gravity}}| \quad (2.19)$$

$$\iff \chi \frac{23\hbar c}{4\pi(2L)^7} \left(\frac{\varepsilon_r - 1}{\varepsilon_r + 2}\right)^2 R^6 \leq \frac{GM^2}{2L}. \quad (2.20)$$

Using $M = 4/3\pi R^3 \rho_{\text{Silica}}$, the minimum separation distance is independent of the size of the particle and is given by

$$L \geq \left(\frac{207}{4096} \frac{\hbar c}{\pi^3 G \rho_{\text{Silica}}^2} \right)^{1/6} \sqrt[6]{\chi} \approx 69 \mu\text{m} \sqrt[6]{\chi}. \quad (2.21)$$

For the same particle as used before, the time for a single measurement, i.e. the coherence time $t_{\text{max}} \approx 30 \text{ s} \sqrt{\chi}$ is very large. The field of levitated particles is promising for these experiments as it offers an isolated, noise-reduced environment while still allowing for exceptional force sensitivity as well as precise quantum control and thus long coherence times [41, 42]. Nevertheless, it would be beneficial to reduce the separation distance between the particles for a shorter measurement time. For this, usually a conducting **Faraday shield** between the particles is proposed [43]. Such a shield would simultaneously suppress all other forms of electromagnetic interactions such as Coulomb forces, if the particles happened to be charged. Coulomb forces have the ability to entangle the particles as well³ and due to the similar distance behavior for Coulomb and gravitational interactions as well as the stronger coupling, these interactions could potentially be problematic.

³In fact, the Aspelmeyer group is currently working on an experiment trying to measure entanglement due to Coulomb interactions [44].

This thesis is focused around the problems which arise in the generation of entanglement in the presence of the Faraday shield. Reconstructing the position states of the masses requires many experimental runs and small variations in the initial setup between measurements introduce effective decoherence. Casimir interactions between the particles and the newly placed Faraday shield can ultimately destroy entanglement in the final averaged measurement. In chapter 4 this effect is analyzed in depth, narrowing the range of viable parameters for particle-shield separation, superposition size, and particle mass. Additionally, thermal vibrations and shield-induced noise are explored in chapter 5.

3 Casimir effect

Casimir forces can be viewed in a very similar way to the *van der Waals forces*. In fact, both phenomena describe just two different sides of the same coin. They define the so-called dispersion forces between neutral atoms or bodies. The quantum theory of van der Waals forces between two neutral atoms was developed by London in 1930 who found the attractive potential $\propto 1/r^6$ for small separations [45]. Casimir and Polder showed in 1948, that for separations larger than the resonance wavelength of the atoms, retardation effects need to be taken into account and the potential decays by a power law of $1/r^7$ [33]. Additionally, they calculated the interaction with an atom or molecule and a perfectly conducting plate, showing that macroscopic objects could experience these **Casimir-Polder interactions** as well. It becomes evident, that a full description of dispersion forces cannot be given by classical electrodynamics alone. Additional considerations regarding relativistic effects and quantum electrodynamics have to be made [46–48]. Casimir, following a suggestion by Bohr [49], found a derivation using the zero-point energy of the vacuum to calculate the attraction between two conducting plates, which works as follows: In quantum electrodynamics the electromagnetic field is described by quantized harmonic oscillators with ground state energy $E_0 = \hbar\omega/2$, where each harmonic oscillator is called a mode. The total *zero-point energy* of the ground state (the vacuum) of the field is therefore given by summing over the energies E_0 for each possible mode n

$$E_{\text{vacuum}} = \frac{\hbar}{2} \sum_n \omega_n. \quad (3.1)$$

These sums are clearly divergent since there exist infinitely many possible modes. While in free space, there are uncountably infinite modes, electrostatic boundary conditions require the field to be zero at the surface of conductors restricting the possible modes between two parallel plates to countably infinite many. Since the difference between two infinite quantities is not well defined, the divergence is often simply dropped, motivated by the fact that energy is usually only defined up to a constant [46]. Precisely the finite difference between the infinite vacuum energy with and without the plates give rise to the macroscopic **Casimir forces**. Using renormalization techniques, Casimir arrived at his famous formula [18]

$$E_{\text{Casimir}} = -\frac{\hbar c \pi^2}{720 L^3} A \quad (3.2)$$

for the attractive Casimir-potential between two conducting plates with surface area A and separation L . The attractive force $F = -\nabla E = -dE_{\text{Casimir}}/dL$ between the plates

3 Casimir effect

can be simply expressed as

$$F_{\text{Casimir}} = -\frac{\hbar c \pi^2}{240 L^4} A, \quad (3.3)$$

where $c = 2.9979... \times 10^8$ m/s is the speed of light. It is remarkable, that such a simple relation arises out of the infinities of the vacuum. To this day, these Casimir forces are a major topic of modern scientific research. They are generally very difficult to calculate for geometries other than two plates or for physical materials with dielectric properties. For simple geometries even the sign of the force is not always intuitively clear [47]: As an example, the Casimir force for an ideal conducting spherical shell leads to an expansion of the sphere [50]. Between other rather simple and important geometries like a sphere-plane or sphere-sphere configuration, no closed and universally applicable expression for the Casimir force exists. In the following section, the different possible approximation methods for large and small separations will be discussed.

Almost ten years after the discovery of Casimir and Polder, Lifshitz was the first to find an expression for the Casimir force between two dielectric plates with arbitrary relative permittivity $\varepsilon_{r,1}$ and $\varepsilon_{r,2}$ for separations larger than the resonant wavelength⁴ [52]. The expression he found facilitates the general complexity of the Casimir interactions and can only be expressed in form of an integral [52]

$$F/A = -\frac{\hbar c}{32\pi^2 L^4} \int_0^\infty dx \int_1^\infty dp \frac{x^3}{p^2} \left\{ \left[\frac{(s_1 + p)(s_2 + p)}{(s_1 - p)(s_2 - p)} e^x - 1 \right]^{-1} + \left[\frac{(s_1 + \varepsilon_{r,1}p)(s_2 + \varepsilon_{r,2}p)}{(s_1 - \varepsilon_{r,1}p)(s_2 - \varepsilon_{r,2}p)} e^x - 1 \right]^{-1} \right\} \quad (3.4)$$

with

$$s_{1(2)} = \sqrt{\varepsilon_{r,1(2)} - 1 + p^2}.$$

In the limit of two perfectly conducting plates, $\varepsilon_{r,1} = \varepsilon_{r,2} \rightarrow \infty$, the integral can be solved analytically resulting in the same expression already obtained by Casimir

$$F_{\text{cond.}}/A = -\frac{\hbar c}{16\pi^2 L^4} \int_0^\infty dx \int_1^\infty dp \frac{x^3}{p^2(e^x - 1)} = -\frac{\hbar c \pi^2}{240 L^4}. \quad (3.5)$$

From eq. (3.4) one can also derive the attraction force between two dielectric plates with the same dielectric constant ε_r (DD) as well as the force between a conducting metal

⁴The “resonance wavelength” for a macroscopic body is the typical wavelength that induces electric excitations in the body. For example, it might be understood as the plasma frequency in the Drude model [51]. Different models for light-matter interaction result in slightly different resonant wavelength. The Lifshitz formula however holds true for the cases of separations in the micro-meter regime for all practical materials [43].

plate and a dielectric plate (DM). The forces are given by

$$F_{\text{DM}} = -\frac{\hbar c \pi^2}{240 L^4} \frac{\varepsilon_r - 1}{\varepsilon_r + 1} \varphi(\varepsilon_r) \quad (3.6)$$

$$F_{\text{DD}} = -\frac{\hbar c \pi^2}{240 L^4} \left(\frac{\varepsilon_r - 1}{\varepsilon_r + 1} \right)^2 \varphi(\varepsilon_r) \quad (3.7)$$

where $\varphi(\varepsilon_r)$ is a tabulated function [52]. For superconducting plates, $\varphi(\varepsilon_r \rightarrow \infty)$ approaches 1 whereas for a perfect dielectric ($\varepsilon_r = 1$) and a metal plate, the function approaches a constant value $\varphi \approx 0.46$. $\varphi(\varepsilon_r)$ is shown for the two cases of DD and DM in fig. 3.1. Since both $(\varepsilon_r - 1)/(\varepsilon_r + 1) < 1$ as well as $\varphi(\varepsilon_r) < 1$ are bounded by 1, the

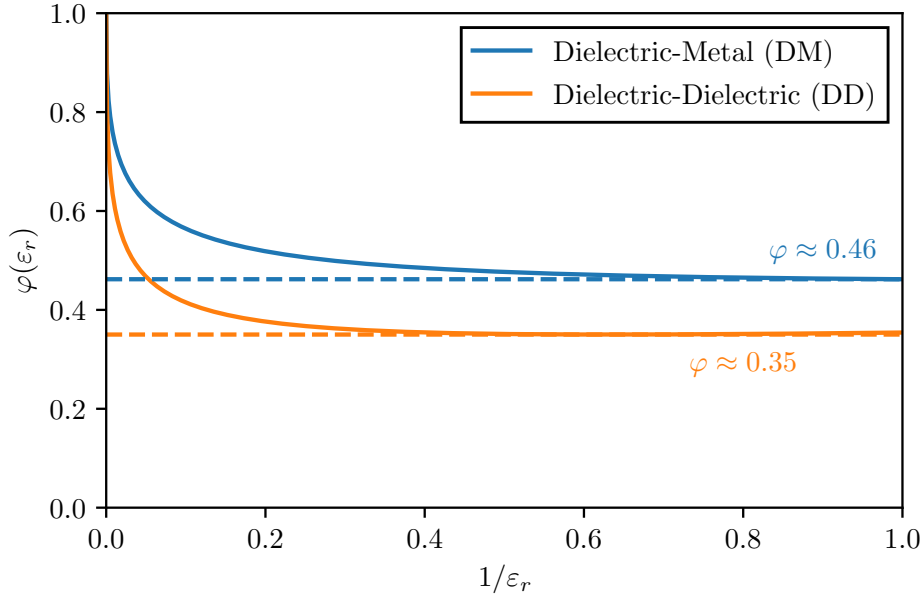


Figure 3.1: Numeric calculations of the function $\varphi(\varepsilon)$ used in the Lifshitz formulas eq. (3.6) and (3.7). The function was calculated for a dielectric and a metal (DM) plate (**blue**) and two dielectric (DD) plates (**orange**). It approaches unity for $\varepsilon_r \rightarrow \infty$ and a finite value for $\varepsilon_r \rightarrow 1$.

Casimir force between dielectrics differs from the force between conducting metals by only a constant. The latter therefore forms an upper bound for the Casimir interaction.

3.1 Proximity force approximation

While the macroscopic Casimir force has an analytical description for two plates, it is not possible to find such an expression for arbitrary geometries. There even exists no analytic expression for the simple (and for this thesis relevant) plate-sphere geometry for all separations of the bodies. Fortunately, approximation methods exist and in particular

the **proximity-force-approximation (PFA)** can, in many cases, be calculated easily as long as the involved surfaces are smooth [53–55]. The PFA is only valid for small separations ($L/R \approx 1$) where R is the typical length scale of the bodies and L the distance between the surfaces. In the sphere-plate geometry, R would be the radius of the sphere and L the center-to-plate distance. In the PFA, the surfaces of the two bodies are divided into infinitesimal small parallel segments with area dA as depicted in fig. 3.2. Finally, one sums over the forces each of the surface elements experiences to estimate the force on the whole body. This is given by

$$E_{\text{PFA}} = \iint_A dA \frac{E_{\text{plate-plate}}}{A} \quad (3.8)$$

where for the Casimir energy per unit area $E_{\text{plate-plate}}/A$ either eq. (3.2) or alternatively any of the Lifshitz equations eq. (3.7) or eq. (3.6) can be used. For the following

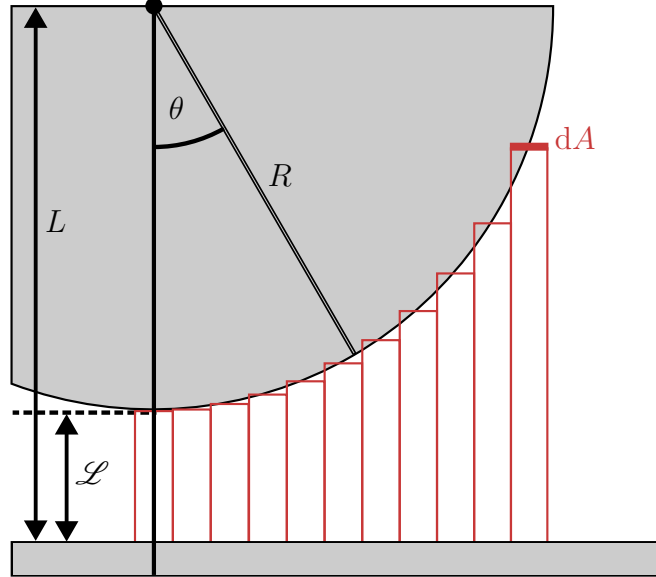


Figure 3.2: In the proximity force approximation the sphere is divided into infinitesimal plane areas dA which all exert a force dF according to eq. (3.3). All the contributions are added up together.

calculations, it is important to distinguish the distance between the plate and the spheres center of mass donated by L and the edge-to-edge separation $\mathcal{L} = L - R$.

The problem with this approximation is that it is ambiguous what surface the area element dA represents. For the plate-sphere geometry, dA can be parametrized either tangential to the sphere or parallel to the plate (or in theory as any other fictitious surface somewhere in between) [55]. In the limit of the validity of the PFA $\mathcal{L} \ll R$ all methods usually yield the same result. For the following calculations, dA is chosen parallel to the plate and the area can be parametrized with $r \in [0, R]$ and $\varphi \in [0, 2\pi]$ resulting in

a distance L between the infinitesimal area elements⁵ $L(r) = \mathcal{L} + R - \sqrt{R^2 - r^2}$. The PFA eq. (3.8) yields for a dielectric sphere and a perfectly conducting plate

$$E_{\text{PFA}} = -\frac{\hbar c \pi^2}{720} \left(\frac{\varepsilon_r - 1}{\varepsilon_r + 1} \right) \varphi(\varepsilon_r) \int_0^R dr \int_0^{2\pi} r d\varphi \frac{1}{L(r)^3} \quad (3.9)$$

$$= -\frac{\hbar c \pi^3}{360} \left(\frac{\varepsilon_r - 1}{\varepsilon_r + 1} \right) \varphi(\varepsilon_r) \frac{R^2}{2\mathcal{L}^2(R + \mathcal{L})} \quad (3.10)$$

$$\stackrel{\mathcal{L} \ll R}{\approx} -\frac{\hbar c \pi^3}{720} \left(\frac{\varepsilon_r - 1}{\varepsilon_r + 1} \right) \varphi(\varepsilon_r) \frac{R}{\mathcal{L}^2} \quad (3.11)$$

3.2 Casimir forces between a conducting plate and a dielectric sphere

There does not exist a closed form expression for the Casimir energy between a dielectric sphere with radius R and dielectric constant ε_r in front of a conducting plate that is applicable at all sphere-plate separations L/R . In the limit of small separations, the proximity force approximation from section 3.1 is valid and yields for dielectric or conducting spheres

$$E_{\text{PFA}} = -\frac{\hbar c \pi^3}{720} \left(\frac{\varepsilon_r - 1}{\varepsilon_r + 1} \right) \varphi(\varepsilon_r) \frac{R}{\mathcal{L}^2} \sim \frac{1}{(L - R)^2} \quad \text{for } L/R \approx 1 \quad (3.12)$$

$$E_{\text{PFA, cond.}} = E_{\text{PFA}}(\varepsilon_r \rightarrow \infty) = -\frac{\hbar c \pi^3}{720} \frac{R}{\mathcal{L}^2}. \quad (3.13)$$

For arbitrary separations, the Casimir energy can only be expressed as an infinite series [40, 54] or in terms of an integral [51]. The integral form reads

$$F = -\frac{\hbar c}{4\pi L^4} \int_0^\infty d\omega \alpha(\omega) [3 \sin 2\omega L - 6L\omega \cos 2\omega L - 6L^2\omega^2 \sin 2\omega L + 4L^3\omega^3 \cos 2\omega L]. \quad (3.14)$$

where α is the electric polarizability of the sphere and the integration is performed over all possible interaction frequencies ω of the electromagnetic field with the materials.

In the **large-separation-limit (LSL)**, where the sphere-plate separation is much larger than the resonant wavelength of the material, the polarizability can be taken as a static constant [43, 51]. In this case, the integral eq. (3.14) can be solved analytically by using an exponential convergence factor resulting in

$$F = -\frac{6\hbar c}{4\pi L^5} \alpha. \quad (3.15)$$

⁵Taking dA tangential to the sphere, it can be parametrized with $\theta \in [0, \pi/2]$ and $\varphi \in [0, 2\pi]$ resulting in $z(\theta) = \mathcal{L} + R - R \cos \theta$. The PFA eq. (3.8) yields with $dA = R^2 \sin \theta d\theta d\varphi$ the result $\propto \frac{\pi R^2 (R + 2\mathcal{L})}{\mathcal{L}^2 (R + \mathcal{L})^2}$ which in the limit of $\mathcal{L} \ll R$ results in the same expression as eq. (3.11).

3 Casimir effect

The polarizability of a uniform dielectric sphere with a dielectric constant ε_r is calculated in appendix A.3 and is given by

$$\alpha_{\text{sphere}} \propto \left(\frac{\varepsilon_r - 1}{\varepsilon_r + 2} \right) R^3 \quad (3.16)$$

resulting in a Casimir energy of

$$E_{\text{LSL}} = -\frac{3}{8} \frac{\hbar c}{\pi L^4} \left(\frac{\varepsilon_r - 1}{\varepsilon_r + 2} \right) R^3 \sim \frac{1}{L^4} \quad \text{for } L/R \gg 1 \quad (3.17)$$

$$E_{\text{LSL, cond.}} = E_{\text{LSL}}(\varepsilon_r \rightarrow \infty) = -\frac{3}{8} \frac{\hbar c R^3}{\pi L^4}. \quad (3.18)$$

This matches precisely the leading-order term in the series expansion from Ref. [54] and Ref. [56]. A comparison of the PFA and LSL approximations across all separations is shown in fig. 3.3, alongside numerical results from Ref [54].

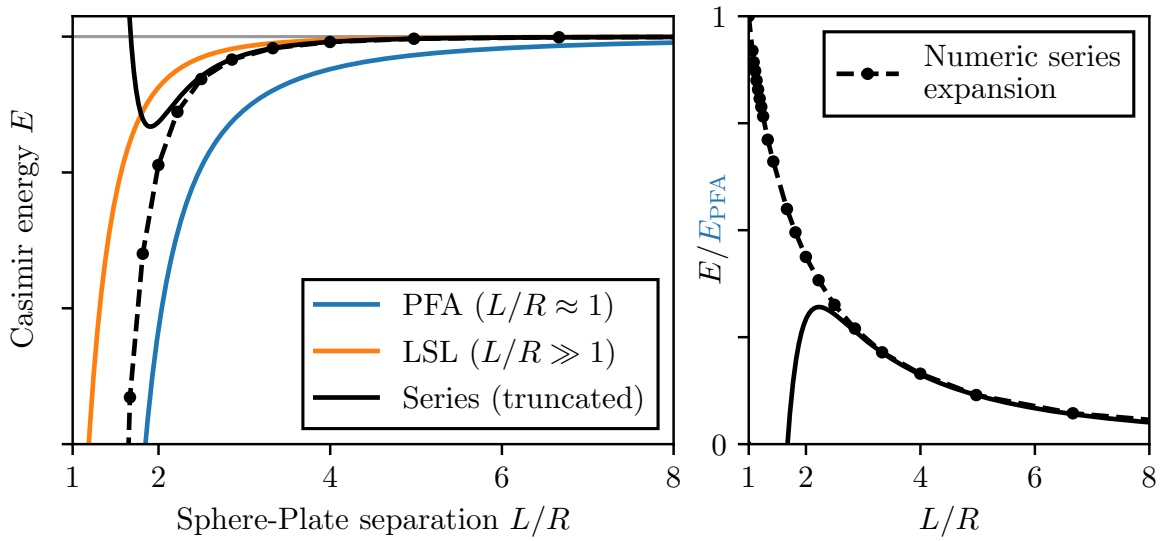


Figure 3.3: Behavior of the Casimir energy for different sphere-plate separations L/R . For close separations ($L/R \approx 1$) the PFA eq. (3.12) is valid whereas for large separations ($L/R \gg 1$) the LSL eq. (3.17) can be used. Additionally the numeric series expansion from Ref. [54] is shown, which converges to the PFA and LSL in each limit.

The scaling of $1/L^4$ for large separations can additionally be motivated empirically. Casimir and Polder [33] calculated the potential between two atoms separated by a distance L with polarizability α_i as⁶

$$E = -\frac{23\hbar c \alpha_1 \alpha_2}{4\pi L^7}. \quad (3.19)$$

⁶For two macroscopic spheres, the Casimir potential looks identical to eq. (3.19). The polarizability α is given by eq. (3.16), resulting in a Casimir potential between two identical dielectric spheres in the large separation limit of $-\frac{23\hbar c}{4\pi L^7} \left(\frac{\varepsilon_r - 1}{\varepsilon_r + 2} \right)^2 R^6$ [40].

3 Casimir effect

If both atoms are approximated as spheres with $\alpha \sim R^3$ and one of them is increased to the size of $R \sim L$, the total Casimir-Polder potential between them effectively scales with $\sim R^3/L^4$. This representation corresponds to the limit $L/R \gg 1$ and aligns with the actual scaling of the macroscopic Casimir potential for large separations in eq. (3.17).

The series expansion in fig. 3.3 suggests, that the proximity-force-approximation is an upper bound for the actual Casimir interaction at all separations. In fact, it can be proven that the PFA for a superconducting sphere and a plate always predicts a stronger force $|\nabla E|$ than the LSL.

Theorem 3.1. *The Casimir force in the PFA-model eq. (3.12) between a superconducting sphere ($\varepsilon_r \rightarrow \infty$) and a perfectly conducting plate is an upper bound for the LSL eq. (3.17).*

Proof. The proof is given in the following steps: **(a)** first it is shown that $|\nabla E_{\text{PFA}}| > |\nabla E_{\text{LSL}}|$ for arbitrary dielectric spheres, then it will be shown **(b)** that $|\nabla E_{\text{PFA, cond.}}| \geq |\nabla E_{\text{PFA, diel.}}|$.

(a) By directly comparing the gradients of eq. (3.12) (PFA) and eq. (3.12) (LSL), one can find the inequality

$$\begin{aligned} & |\nabla E_{\text{PFA}}| > |\nabla E_{\text{LSL}}| \\ \iff & \frac{2\hbar c\pi^3}{720} \left(\frac{\varepsilon_r - 1}{\varepsilon_r + 1} \right) \varphi(\varepsilon_r) \frac{R}{\mathcal{L}^3} > \frac{12\hbar c}{8\pi L^5} \left(\frac{\varepsilon_r - 1}{\varepsilon_r + 2} \right) R^3 \\ \iff & \frac{\pi^4}{540} \left(\frac{\varepsilon_r + 2}{\varepsilon_r + 1} \right) \varphi(\varepsilon_r) > \frac{(L - R)^3 R^2}{L^5} = \left(\frac{R}{L} \right)^2 - 3 \left(\frac{R}{L} \right)^3 + 3 \left(\frac{R}{L} \right)^4 - \left(\frac{R}{L} \right)^5 \end{aligned}$$

One can easily convince themselves that the right-hand side (for $R/L \leq 1$) is upper-bounded by ≈ 0.0346 (at $R/L = 0.4$). By remembering that $(\varepsilon_r + 2)/(\varepsilon_r + 1) > 1$ and $\varphi(\varepsilon_r) \gtrsim 0.46$ one can put a lower bound on the left-hand side by $0.0830 > 0.0346$. Therefore, $|\nabla E_{\text{PFA}}| > |\nabla E_{\text{LSL}}|$.

(b) By using eq. (3.12) and eq. (3.13) for the PFA of a dielectric and conducting sphere, it follows quickly that $|\nabla E_{\text{PFA, cond.}}| \geq |\nabla E_{\text{PFA}}(\varepsilon_r)|$, because $\varphi(\varepsilon_r)$ as well as $(\varepsilon_r - 1)/(\varepsilon_r + 1)$ are monotonically increasing with ε_r .

Combining steps **(a)** and **(b)** results in

$$|\nabla E_{\text{PFA, cond.}}| \geq |\nabla E_{\text{PFA, diel.}}| > |\nabla E_{\text{LSL}}|. \quad (3.20)$$

Thus, the PFA provides an upper bound over the LSL at all separations. \square

Remark. Considering the numerical series expansion, it appears as if the argument applies at all separations L/R - although this is not mathematically proven here.

For later calculations, only the difference in the Casimir energy for slightly different separations L and thus effectively the gradient $\nabla E = dE/dL$ is required. Thus, the proof was given in terms of the Casimir force $F = -\nabla E$.

For subsequent calculations, the PFA is therefore used as a worst-case approximation of the Casimir energy. Whenever possible, results are cross-verified and compared with the LSL model.

3.3 Imperfect surfaces of the plate and the sphere

In practice, the surfaces of the sphere and plate are not perfectly flat and contain imperfections, leading to small, localized variations in the sphere-plate separation and consequently to slight changes in the Casimir energy. While in reality, both the sphere and the plate have rough surfaces, we limit ourselves to the case where the plate is rough and the sphere is smooth, as we do not expect any fundamental changes. Under the PFA, the Casimir interaction solely depends on the surface-to-surface separation \mathcal{L} and thus, all irregularities on the sphere's surface can effectively be modeled as an equivalent roughness on the plate. To quantify and estimate the impact of uneven surfaces on the Casimir energy, several representative types of plate imperfections with characteristic amplitude $\Delta\mathcal{L}$ shown in fig. 3.4 have been studied with numerical methods.

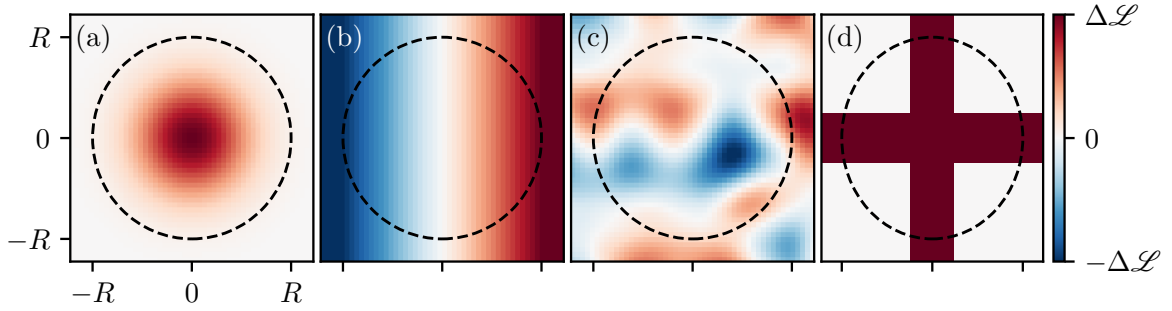


Figure 3.4: A selection of imperfect plates. **(a)** A simple gaussian deformation in the same size as the sphere. **(b)** Linearly inclining plate or a tilted flat plate. **(c)** Uneven and noisy but uniformly random surface realized using *Perlin noise* [57]. **(d)** A cross-shape in the center of the plate.

- (a)** A *gaussian shaped bump or dip* in the plate can be used to describe a range of possible local deformations comparable in size to the sphere. For a small shield ($r_s \approx R$), thermal vibrations resemble these deformations, as discussed in chapter 5. Displacements with positive or negative amplitudes $\pm\Delta\mathcal{L}$ following a Gaussian profile were studied.
- (b)** If the characteristic length scale of imperfections is much larger than the sphere's radius and the sphere is sufficiently close to the plate, it experiences a nearly linear gradient in the plate's surface height, effectively behaving as though the plate was tilted. These *linear deflection* can describe thermal vibrations for larger shields $r_s \ll R$. At small gradients, variations in the Casimir potential cancel out in first

3 Casimir effect

order since the potential in the PFA $1/(\mathcal{L} \pm \Delta\mathcal{L})^2 \sim 1/\mathcal{L}^2 \mp 2\Delta\mathcal{L}/\mathcal{L}^3$ depends linearly on the deflection. As a result, no significant change in the total attraction force is expected.

- (c) Similarly negligible are *random noisy but uniformly distributed deformations*, provided the typical length scale of the noise is smaller than the sphere's radius. Here, the noise was modeled using *Perlin noise* [57], which produces smooth pseudo-random surface textures commonly used in computer science to imitate surface roughness. Equidistant grid-points are defined, each of which is assigned with a pseudo-random gradient. The noise function follows this gradient in the vicinity of a grid-point and the interpolation between points generates smooth transitions. Due to the uniformness, no large deviations from an ideal flat plate are expected.
- (d) Structural features on the plate, such as a *centered cross*, may enhance the stability and rigidity of the shield, potentially reducing thermal vibrations. However, the effects of such features, including amplification of the Casimir interaction, must be investigated further.

The resulting Casimir potentials between a macroscopic sphere and the imperfect surfaces were numerically calculated in the PFA and are shown in fig. 3.5. All imperfections are bounded by the potential between a sphere and a perfectly flat ideal plate moved by a distance $\Delta\mathcal{L}$ closer or farther. This is symbolized by the gray region in fig. 3.5. For the gaussian distributions, this overestimation is not particularly large and especially for large structures, like the cross, this bound is practically reached. As expected, the uniformly distributed noise as well as a slightly tilted plane do not increase the Casimir potential substantially even at small separations. For small imperfections or large separations, plate imperfections are negligible as the relative effect decreases with $\Delta\mathcal{L}/\mathcal{L} \rightarrow 0$. However, the considerations made in this section are particularly important for small shields the size of the particles and close distances.

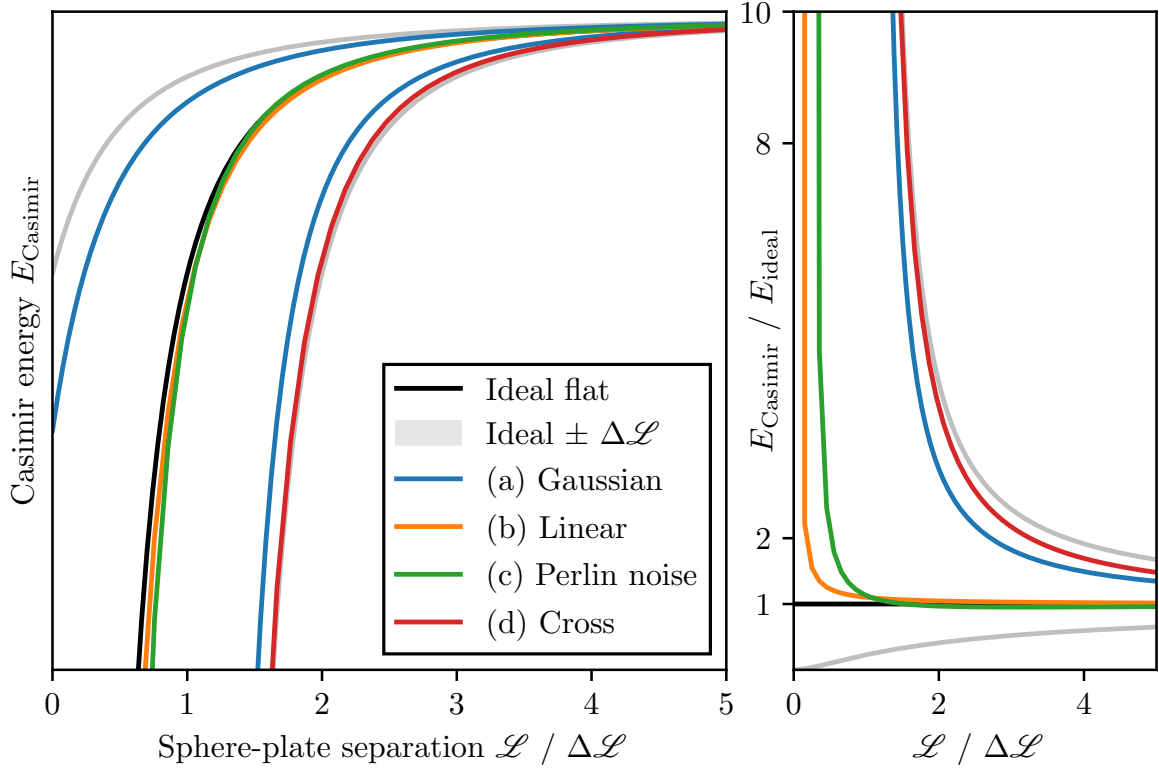


Figure 3.5: Casimir energy between a sphere and plates with surface imperfections shown in fig. 3.4. The gaussian deformation (blue) was calculated for displacements with amplitude $\pm\Delta\mathcal{L}$. The shaded region bounds all imperfections and represents the Casimir energy between a flat plate moved $\pm\Delta\mathcal{L}$ closer or farther to the sphere. In the limit $\Delta\mathcal{L} \ll \mathcal{L}$, all imperfections are negligible.

4 The particle in front of a static shield

The generalized configuration of the system described in chapter 2 with the inclusion of a conducting Faraday shield is shown in fig. 4.1. Similar to the prior arrangement, particles

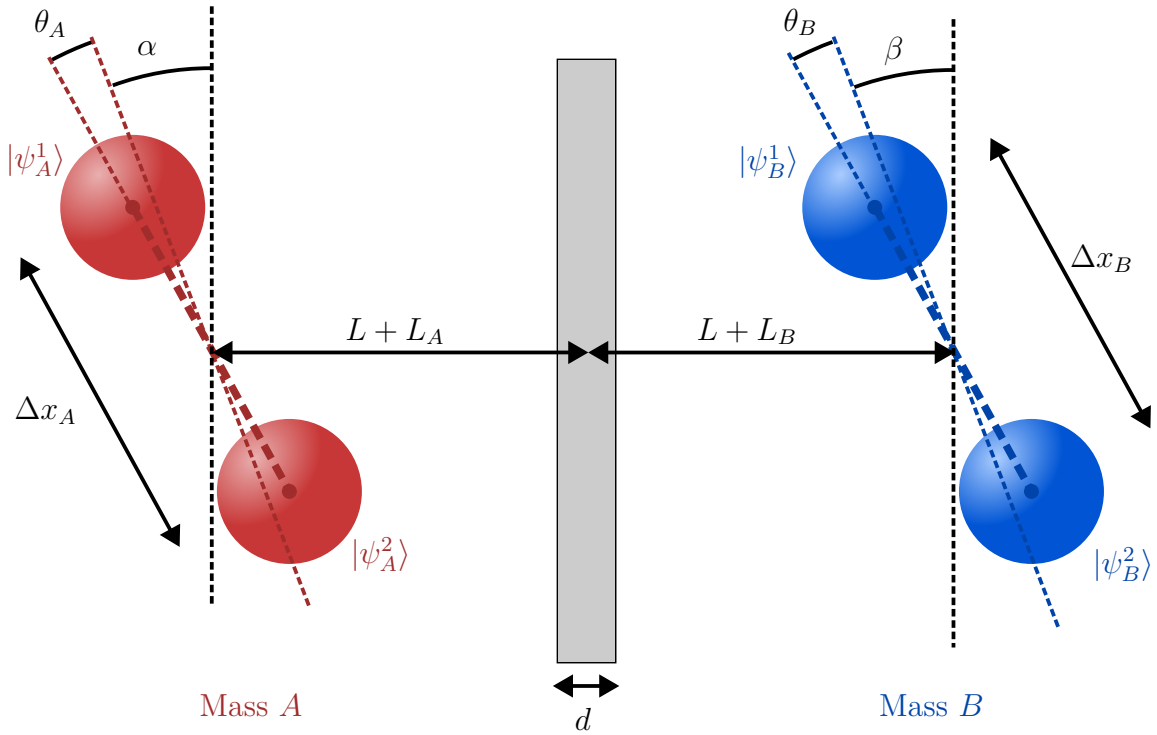


Figure 4.1: Schematic representation of the experimental setup for detecting gravitationally induced entanglement between particles A and B with radius R separated by a distance $2L + L_A + L_B$. Their respective orientations relative to the shield are specified by angles α and β , subject to small random variations $\theta_{A(B)}$. All variations are modeled with a normal distribution around zero with standard deviation $\Delta L_{A(B)}$ and $\Delta \theta_{A(B)}$. Each particle is in a delocalized cat-state with a size $\Delta x_{A(B)}$ between states $|\psi_{A(B)}^1\rangle$ and $|\psi_{A(B)}^2\rangle$. A conducting Faraday shield of thickness d is placed in the center.

A and B are prepared in delocalized spatial Schrödinger-cat states with superposition

sizes Δx_A and Δx_B respectively. They are positioned at a distance L from the shield, with their cat-state superpositions aligned at angles $\alpha, \beta \in [0, \pi)$ relative to it. The special case $\alpha = \beta = 0$ defines the “parallel orientation”, while $\alpha = \beta = \pi/2$ defines the “orthogonal orientation”.

Under the assumptions that gravity can mediate entanglement, particles A and B can get entangled. Casimir interactions between the particles and the newly introduced shield must additionally be considered, especially at small separations. These interactions contribute only phase shifts to individual cat-states, but do not couple the particles and hence cannot generate entanglement - assuming a static shield e.g. at zero temperature.

Experimental considerations pose additional complexities, particularly concerning the detection of entanglement. One proposed solution involves employing an entanglement witness [15, 19], whose selection depends on the experimental specifics. For simplicity, in this thesis it is assumed that the full density matrix of the system is accessible and entanglement is quantified with the logarithmic negativity introduced in section 2.2. Furthermore, the analysis confines each cat-state to a truncated two-dimensional Hilbert space, as only the relative dynamic phase differences between two such states are of interest. Consequently, the density matrix has 16 entries, of which only nine are independent, making reconstruction possible using known matrix properties (e.g., hermiticity $\rho^\dagger = \rho$ and normalization $\text{tr } \rho = 1$). Precise state tomography, however, requires numerous measurements due to quantum probabilistic behavior. Stochastic variability in the placements across runs - expressed by angular variations $\alpha + \theta_A$ and $\beta + \theta_B$ or by variations in the particle-shield separation $L + L_A$ and $L + L_B$ - leads to an initially mixed state ρ_0 . Even with exact particle placement, thermal vibrations of the shield induce further variations in particle-shield separation, analyzed in chapter 5. Other experimental noise sources, such as variations in the measurement timing, have been considered previously in Ref. [58].

If the random variable $X \in \{\theta_A, \theta_B, L_A, L_B\}$ is subject to statistical variations, the resulting mixed state can be described by

$$\rho = \int_{-\infty}^{\infty} dX \frac{1}{\sqrt{2\pi}\Delta X} e^{-X^2/2(\Delta X)^2} |\psi_X\rangle\langle\psi_X|, \quad (4.1)$$

where $|\psi_X\rangle$ is the pure state of a single measurement dependent on the random variable X . Placement variations are assumed to be normally distributed with mean $\langle X \rangle = 0$ and standard deviation ΔX on the basis of the central limit theorem [59, p. 1195]. While potential correlations between $\theta_{A(B)}$ and $L_{A(B)}$ are possible, they are initially assumed negligible to yield a conservative estimate. In chapter 5 during the analysis of thermal vibrations of the Faraday shield, cases involving correlated variables due to thermal shield vibrations are analyzed.

Convergence for a finite number of measurements

Experimentally, it would be very interesting to know how fast the averaged density matrix $\bar{\rho}$ after a finite number of N measurements converges to the idealized asymptotic mean $\langle \rho \rangle$ given by eq. (4.5). After N measurements, the sample average is given by

$$\bar{\rho} = \frac{1}{N} \sum_{k=1}^N \rho(X_k) \quad (4.2)$$

where $\rho(X)$ depends on the random variable $X \in \{\theta_{A(B)}, L_{A(B)}\}$ and X_k is the k -th sample drawn from the normal distribution $\mathcal{N}(0, (\Delta X)^2)$ ⁷. As $N \rightarrow \infty$, the law of large numbers and in particular the central limit theorem (CLT) ensures that $\bar{\rho} \rightarrow \langle \rho \rangle$ [59, p. 1195]. According to the CLT, the sample average $\bar{\rho}(X)$ fluctuates around $\langle \rho \rangle$ with a standard deviation given by the Berry-Esseen theorem for independent and identically distributed random variables X_k by $\sigma \sim N^{-1/2}$ [60]. Thus, if the placements of the particles in each measurement are completely independent from each other, the rate of convergence to the ideal mean $\langle \rho \rangle$ is governed by $\mathcal{O}(1/\sqrt{N})$.

It is however very likely that measurements are mostly performed consecutively in the same trap so that the particle placements in successive measurements are correlated. The correlations $\text{Cov}[\rho(X_i), \rho(X_j)] = c_{|i-j|}$ between the i -th and j -th measurement should therefore decrease with increasing $|i-j|$. The variance of $\bar{\rho}$ is now dependent of these correlations in the form [59, p. 1227]

$$\text{Var}[\bar{\rho}] = \frac{1}{N^2} \sum_{i,j=1}^N \text{Cov}[\rho(X_i), \rho(X_j)] = \frac{1}{N} \text{Var}[\rho] + \frac{2}{N^2} \sum_{n=1}^{N-1} (N-n)c_n \quad (4.3)$$

where $\text{Cov}[\rho, \rho] = \text{Var}[\rho]$ was used for the variance of the mean density matrix $\langle \rho \rangle$. For correlations $c_n \sim n^{-\alpha}$ ($\alpha < 1$) the sum in eq. (4.3) can be asymptotically calculated by the Euler-Maclaurin formula and scales like

$$\sum_{n=1}^{N-1} (N-n)n^{-\alpha} \xrightarrow{N \rightarrow \infty} \int_1^N dn (N-n)n^{-\alpha} \sim N^{2-\alpha} \quad (4.4)$$

which results in $\text{Var}[\bar{\rho}] \sim N^{-\alpha}$. In the asymptotic limit the standard deviation of the sample average $\sqrt{\text{Var}[\bar{\rho}]}$ and thus the convergence rate to the mean $\langle \rho \rangle$ scales with $\mathcal{O}(1/\sqrt{N^\alpha})$. This convergence is arbitrary slow for small α (if the setup does not change a lot between individual measurements) and thus the calculations in the next sections are just a worst-case estimation of the actual experimental results. If a weaker correlation in the form of $c_n \sim e^{-\alpha n}$ is assumed, the convergence rate is again asymptotically governed by $\mathcal{O}(1/\sqrt{N})$.

⁷Here it is not strictly required that X_k are normally distributed. As long as they are i.i.d. random variables, any distribution is sufficient for the following argumentation [59, p. 1195].

4.1 Entanglement generation

The averaged state $\langle \rho \rangle$ after multiple measurements is given by

$$\langle \rho \rangle = \int_{-\infty}^{\infty} d\theta_A p(\theta_A) \int_{-\infty}^{\infty} d\theta_B p(\theta_B) \int_{-\infty}^{\infty} dL_A p(L_A) \int_{-\infty}^{\infty} dL_B p(L_B) \rho(\theta_A, \theta_B, L_A, L_B) \quad (4.5)$$

where $p(\cdot)$ represents the Gaussian distributions of the random variables $\theta_{A(B)}$ and $L_{A(B)}$ with standard deviations $\Delta\theta$ or ΔL respectively. $\rho(\theta_A, \theta_B, L_A, L_B)$ denotes the state of a single measurement, dependent on the initial setup of the system. The state ρ_0 at $t = 0$ is given as before by eq. (2.2). Beyond mutual gravitational interactions, the dynamic phases $\phi_{A(B), \text{Cas}}^{(i)}(t)$ are induced on the cat-states $|\psi_{A(B)}^{(i)}\rangle$ ($i = 1, 2$) by Casimir interactions with the Faraday shield. Using the two different models for the Casimir attraction for large and small separations given by eq. (3.12) and eq. (3.12), it follows

$$\phi_{A(B), \text{Cas}}^{(i)}(t) = \frac{t}{\hbar} \begin{cases} \frac{3\hbar c}{8\pi} \left(\frac{\varepsilon_r - 1}{\varepsilon_r + 2} \right) \frac{R^3}{\left(L_{A(B)}^{(i)} \right)^4} & \text{for large separations (LSL)} \\ \frac{\hbar c \pi^3}{720} \varphi(\varepsilon_r) \left(\frac{\varepsilon_r - 1}{\varepsilon_r + 1} \right) \frac{R}{\left(\mathcal{L}_{A(B)}^{(i)} \right)^2} & \text{for small separations (PFA)} \end{cases} \quad (4.6)$$

Here, $L_{A(B)}^{(i)}$ and $\mathcal{L}_{A(B)}^{(i)} = L_{A(B)}^{(i)} - R$ are the distances between the particles and the shield's surface given by

$$L_A^{(i)} = L + L_A - \frac{d}{2} \pm_i \frac{\Delta x_A}{2} \sin(\alpha + \theta_A) \quad \text{and} \quad (4.7)$$

$$L_B^{(i)} = L + L_B - \frac{d}{2} \mp_i \frac{\Delta x_B}{2} \sin(\beta + \theta_B) \quad (4.8)$$

where $\pm_i = -(-1)^i$ distinct between the two cat-states of a single particle. The gravitationally induced phase between states $|\psi_A^{(i)}\rangle \otimes |\psi_B^{(j)}\rangle$ is given analogue to the previous calculations in chapter 2 as

$$\phi_{\text{Grav}}^{(ij)}(t) = \frac{t}{\hbar} \frac{GM_A M_B}{L^{(ij)}}. \quad (4.9)$$

The separation $L^{(ij)}$ between the particle cat-states $A^{(i)}$ and $B^{(j)}$ is given by

$$L^{(ij)} = \sqrt{\left(2L + L_A + L_B \pm_i \frac{\Delta x_A}{2} \sin(\alpha + \theta_A) \mp_j \frac{\Delta x_B}{2} \sin(\beta + \theta_B) \right)^2 + \left(\frac{\Delta x_A}{2} \cos(\alpha + \theta_A) \mp_{i=j} \frac{\Delta x_B}{2} \cos(\beta + \theta_B) \right)^2} \quad (4.10)$$

with $\mp_{i=j} = +(-1)^{\delta_{ij}}$. Expanding to first order in $\Delta x_{A(B)} \ll L$, $\theta_{A(B)} \ll 1$ and $L_{A(B)} \ll 1$ (which is justified as seen in the following), the averaged evolved state $\langle \rho \rangle$ in eq. (4.5) is analytically obtainable, as shown in appendix B.2. Assuming $\Delta\theta_A = \Delta\theta_B \equiv \Delta\theta$ and $\Delta L_A = \Delta L_B \equiv \Delta L$, the off-diagonal elements (the so-called *coherences*) decay with

$$\langle \rho_{kl} \rangle = \frac{1}{4} e^{i\Delta\phi_{kl}(t)} \exp\left\{ -\frac{(\xi_{kl})^2}{2} (\Delta\theta)^2 t^2 \right\} \exp\left\{ -\frac{(\zeta_{kl})^2}{2} (\Delta L)^2 t^2 \right\} \quad (4.11)$$

Orientation	Particle size		L	Δx	Shield size ^b	
	Radius R	Mass M ^a			d	r_s
Parallel ($\alpha = \beta = 0$)	$10\ \mu\text{m}$ $= 10^{-5}\text{ m}$	$\approx 10^{-11}\text{ kg}$ $= 5 \times 10^{-4} m_p$	$2R = 20\ \mu\text{m}$	100 nm	100 nm	1 cm

^a Here $m_p = \sqrt{\hbar G} \approx 2.17 \times 10^{-8}\text{ kg}$ is the Planck mass. ^b The required size of the shield is later estimated in section 5.1.

Table 4.1: Default parameters for the setup in fig. 4.1. Maximum entanglement is reached after $t_{\text{max}} = 258\text{ ms}$ for these parameters. They were chosen in accordance with multiple proposals [41, 61]. Both particles are assumed to be identical. The thickness d and radius r_s of the shield is estimated in section 5.1.

where $\Delta\phi$, ξ and ζ are substitutes for lengthy expressions given by eq. (B.2), eq. (B.15) and eq. (B.18) in the appendix and are dependent on system parameters. For $\Delta\theta, \Delta L \rightarrow \infty$ or $t \rightarrow \infty$, coherences vanish, resulting in a maximally mixed state with $\text{tr } \rho^2 = 1/4$ - which is not entangled. For large variations in the initial placement of the particles, one therefore expects the loss of entanglement.

For the special case of two identical particles and $\alpha = \pm\beta$, the logarithmic negativity E_N is approximated to first order as

$$E_N(\langle\rho\rangle) = \max \left\{ 0, \log_2 \left(e^{-\gamma} (\cosh \gamma + |\sin \phi|) \right) \right\} \quad (4.12)$$

where the decoherence parameter $\gamma = (\xi^2(\Delta\theta)^2/2 + \zeta^2(\Delta L)^2/2) t^2$ is given in eq. (B.21) and the phase ϕ is given by eq. (4.15) in the next section. Numerical results validate this approximation and are shown in fig. 4.2 for varying $\Delta\theta$ and ΔL in the parallel configuration. For small placement variations, the system remains entangled. However, once the critical thresholds $\Delta\theta_{\text{crit}}$ and ΔL_{crit} are surpassed, entanglement is lost entirely. The critical decoherence threshold γ_{crit} is given by

$$\gamma_{\text{crit}} = \log(1 + \sqrt{2}) = \text{const.} \quad (4.13)$$

which imposes $\Delta\theta_{\text{crit}} \propto 1/(\xi t)$ and $\Delta L_{\text{crit}} \propto 1/(\zeta t)$. For the parameters in table 4.1, these thresholds are around $\Delta\theta_{\text{crit}} \approx 6 \times 10^{-10}\text{ rad}$ and $\Delta L_{\text{crit}} \approx 1.4 \times 10^{-10}\text{ m}$, which seems challenging experimentally. For all these calculations, the radius of the particles is set to $R = 10^{-5}\text{ m} = 10\ \mu\text{m}$ with corresponding masses $M = 4/3\pi R^3 \rho_{\text{Silica}} \approx 1.1 \times 10^{-11}\text{ kg}$. A particle-shield separation of $L = 2R$ and a superposition size of $\Delta x = 100\text{ nm}$ are used. In the rest of this thesis, if not otherwise specified, these parameters are used as a default. For convenient retrieval, they are collectively displayed in table 4.1.

These values are consistent with theoretical proposals (see e.g. the Tab. 1 in Ref. [61]) as they result in a low one-run duration of $t_{\text{max}} \approx 258\text{ ms}$ [41, Timestamp: 51:00],

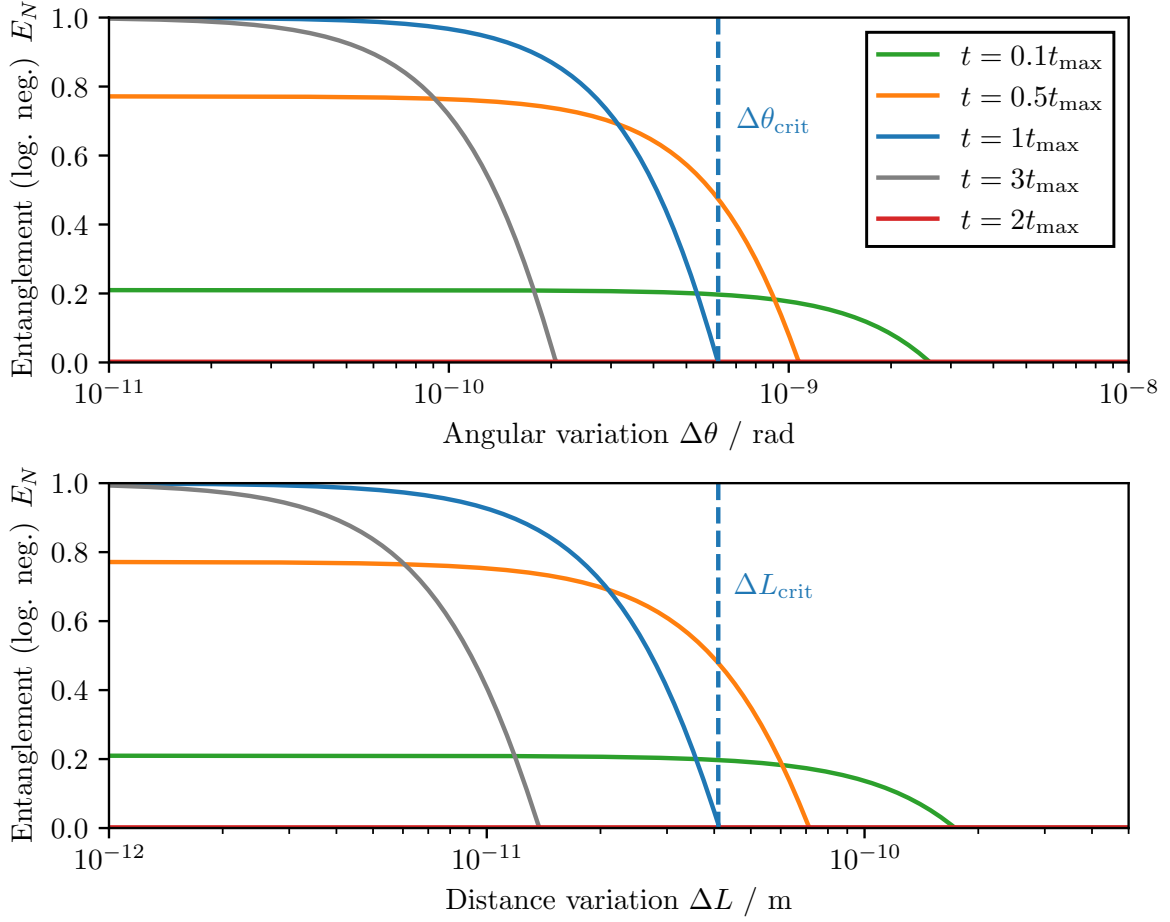


Figure 4.2: Entanglement quantified by the logarithmic negativity dependent on the placement variations in the initial setup $\Delta\theta$ and ΔL . The entanglement is shown at different times, where $t_{\max} \approx 258$ ms is the time from eq. (4.16), after which maximal entanglement is reached. At a critical point $\Delta\theta_{\text{crit}}$ or ΔL_{crit} , all entanglement is lost. The used parameters are taken from table 4.1.

but remain beyond current experimental capabilities. The largest mass demonstrated in matter-wave interferometry is around 4×10^{-23} kg [31] with a spatial superposition size of $\Delta x \gtrsim 500$ nm. In solid-state opto-mechanical systems, quantum control and ground-state cooling have been demonstrated with masses of 10^{-13} kg with mechanical oscillators coupled to superconducting qubits [37]; entangled diamonds with 10^{-11} kg have been observed [62] and masses of 10^{-8} kg have been prepared in motional center-of-mass cat-states [63], although with very short coherence times $\lesssim 1 \mu\text{s}$. Also impressive and notable is the cooling of the ~ 40 kg LIGO mirrors to only very few occupied phonon states [64]. In contrast, the smallest mass with a measurable gravitational force is around 92 mg [32]. The field of levitated nano-particles has the potential to bridge the worlds of molecular superposition and mechanical systems, offering exceptional quantum control,

high force sensitivity and long coherence times up to seconds [41]. Thus many proposals aim to measure quantum entanglement due to gravity between trapped and levitated particles [17, 42].

Nonetheless, the required accuracy in the placement of the particles appears very challenging experimentally. However, looking at the entanglement dynamics in fig. 4.3, for shorter times $t < t_{\max}$, greater variations in particle placement can be tolerated at the cost of reduced entanglement. At these shorter times, the gravitational interaction has

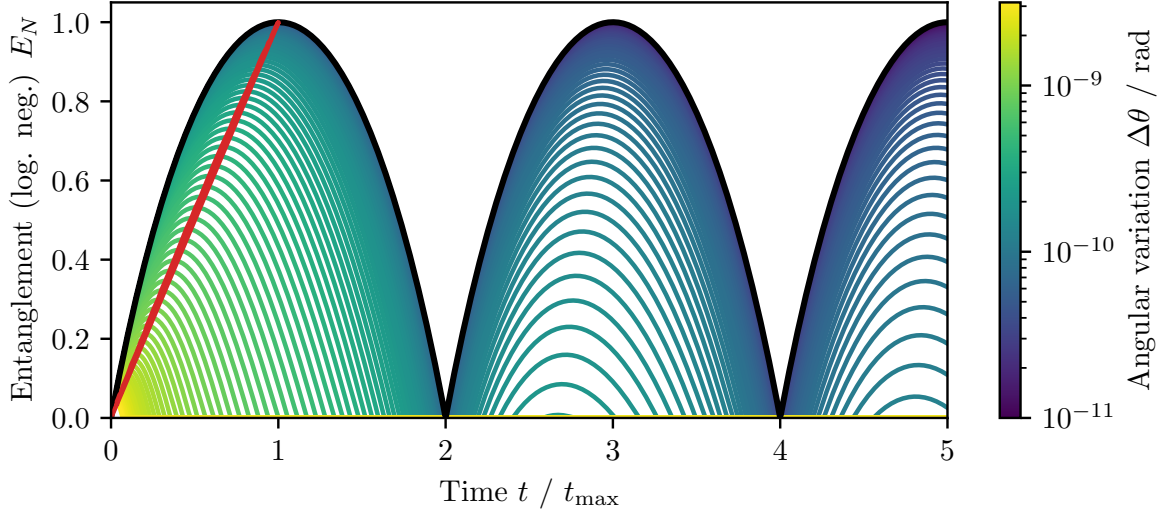


Figure 4.3: Entanglement dynamics after eq. (4.12) for different angular variations $\Delta\theta$ for the parameters used in table 4.1. The black outer most line shows the ideal case without any placement variations and aligns with fig. 2.2. For large variations, entanglement is only observable during a brief window of time with an optimal measurement time colored in red.

not fully entangled the particles, and decoherence (which scales as $\gamma \propto t^2$) has not yet significantly developed. If achieving full entanglement is not required and *any* amount of entanglement $E_N > 0$ suffices, it may be advantageous to perform measurements at $t < t_{\max}$. This, of course, requires ensuring that other entanglement mechanisms contribute smaller entanglement rates (see chapter 5 for further discussion). Decoherence effects from collisions with air molecules and thermal black-body radiation should also be taken into account. The optimal measurement time for a required level of entanglement is depicted in fig. 4.4. The figure also provides the corresponding maximum allowable variation for a given time. Conversely, for fixed variations, the optimal measurement time and maximum attainable entanglement can be determined. It can be seen that at times $2kt_{\max}$, $k \in \mathbb{N}$ no entanglement is measurable, coinciding with the findings for the ideal scenario in chapter 2.

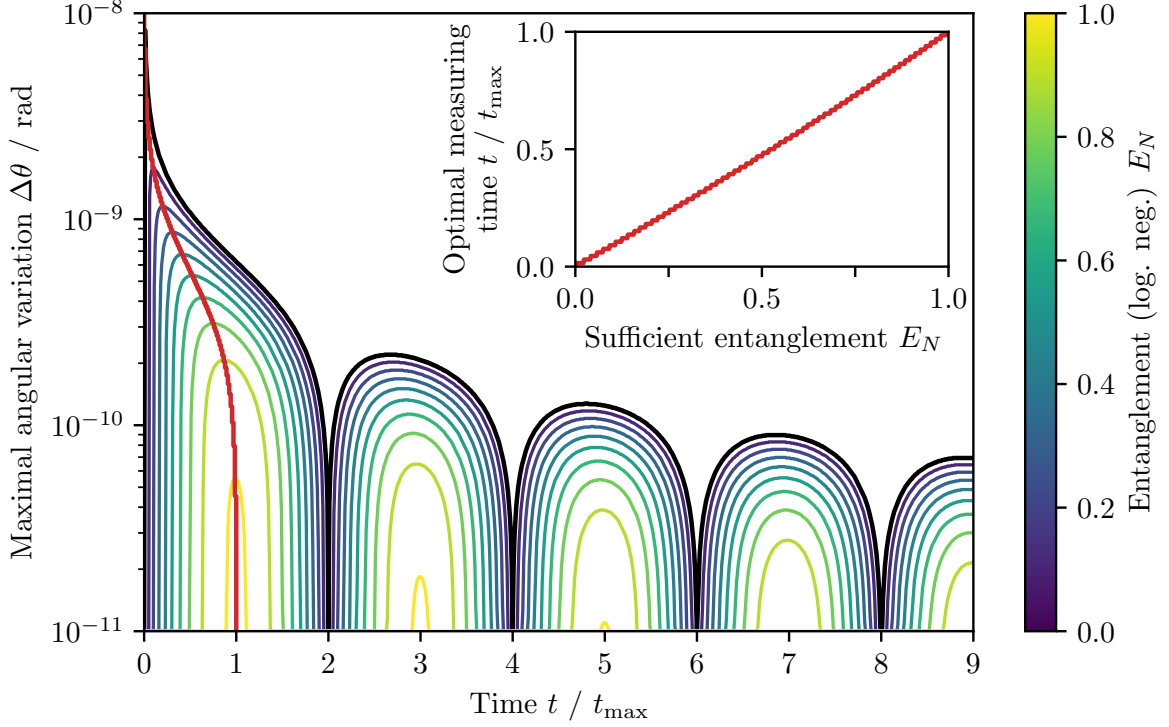


Figure 4.4: Maximal angular variation for given times after which a specific amount of entanglement E_N is still measurable. The setup parameters are taken from table 4.1. The outer most black line corresponds to the time dependence of $\Delta\theta_{\text{crit}}$. A fully entangled state with $E_N = 1$ is only measurable at $t = t_{\text{max}}$ with a maximally possible angular variation of around 10^{-11} rad. The red curve on the top left shows the optimal measuring time for a specific amount of entanglement and aligns precisely with the red curve in fig. 4.3. Correspondingly, the red curve in the main figure shows the maximal angular variation for which this goal is reachable. At times $2kt_{\text{max}}$, $k \in \mathbb{N}$ no entanglement can be measured.

4.2 The optimal setup

With the general framework in hand, the next logical question to ask is, whether the stability against placement-variations can be improved. The rule of thumb for these optimizations is the following: Increase the gravitational interaction by either having heavier and larger particles or by reducing the separation distance L without substantial sacrifices of experimental realization. As an example, the stability increases intuitively by increasing the separation distance L . However, this does also increase the time $t_{\max} \propto L^3$ until the maximum amount of entanglement can be measured which would increase the total time $\sim N t_{\max}$ of the experiment with N individual measurements. It is not immediately obvious, how the stability and the maximum possible variations $\Delta\theta_{\text{crit}}$ and ΔL_{crit} behave for the change in parameters. In the following section, precisely the dependence of this stability is discussed for altering the orientation α, β , the particle-shield separation L , the mass $M_A = M_B \equiv M$ and the superposition size $\Delta x_A = \Delta x_B \equiv \Delta x$ for two identical particles.

4.2.1 Orientation

One of the arguably easiest parameters to change in the experimental setup is the orientation of the cat-state superpositions, which is quantified by $\alpha, \beta \in [0, \pi)$ in fig. 4.1. As already seen in fig. 2.2, maximal entanglement in the parallel orientation is reached after twice the time compared to the orthogonal orientation. In general, it is advantageous to aim for the highest entanglement rate and thus the smallest $t_{\max}(\alpha, \beta)$, as this requires a shorter coherence time and thus reduces the total time of the experiment. The previous results from chapter 2 can be further generalized for an arbitrary orientation α, β . The logarithmic negativity is given by (derived in appendix B.1)

$$E_N = \log_2 (1 + |\sin \phi|) \quad (4.14)$$

where ϕ is now dependent on the orientation and is defined as (for $\Delta x \ll L$)

$$\phi = \frac{GM_A M_B \Delta x_A \Delta x_B}{8\hbar L^3} t \left(\sin \alpha \sin \beta - \frac{1}{2} \cos \alpha \cos \beta \right). \quad (4.15)$$

The maximum entanglement $E_N = 1$ is reached for $\phi = \pm\pi/2$ and thus after a time

$$t_{\max}(\alpha, \beta) = \frac{4\pi\hbar L^3}{GM_A M_B \Delta x_A \Delta x_B} \left| \sin \alpha \sin \beta - \frac{1}{2} \cos \alpha \cos \beta \right|^{-1}. \quad (4.16)$$

For the specific symmetric cases $\alpha = \pm\beta$ and $\beta = 0$, the resulting entanglement times are shown in fig. 4.5. The global minima of $t_{\max}(\alpha, \beta)$ is attained in the orthogonal orientation. This is not surprising considering that this orientation maximizes the *differences in separation distances* between all superposition cat-states. Much more interesting and unanticipated are the singularities in fig. 4.5 which appear for

$$\sin \alpha \sin \beta = \frac{1}{2} \cos \alpha \cos \beta. \quad (4.17)$$

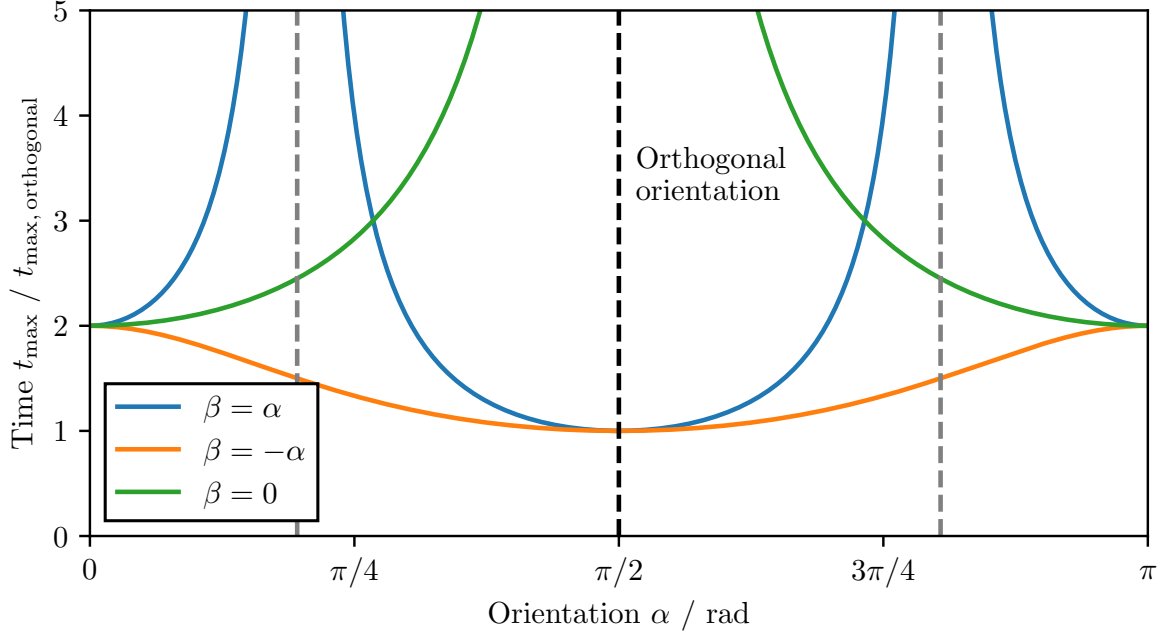


Figure 4.5: Time $t_{\max}(\alpha, \beta)$ for different orientations in the special symmetric cases of $\alpha = \pm\beta$ and $\beta = 0$. After this time, a maximally entangled state $E_N = 1$ is reached. The singularity $t_{\max} \rightarrow \infty$ for $\beta = 0$ and $\alpha = \pi/2$ is expected, as all separations between the cat states $|\psi_A^{(1)}\rangle \leftrightarrow |\psi_B^{(1),(2)}\rangle$ and $|\psi_A^{(2)}\rangle \leftrightarrow |\psi_B^{(1),(2)}\rangle$ is equal. The two other singularities for $\alpha = \beta = 2 \arctan(\sqrt{3} \pm \sqrt{2})$ are explainable by the fact that all separations lie in the “harmonic mean”, as seen in fig. 4.6.

For $\beta = 0$ the singularity at $\alpha = \pi/2$ is not surprising. In this configuration, the distances $|\psi_A^{(1)}\rangle \leftrightarrow |\psi_B^{(1),(2)}\rangle$ and $|\psi_A^{(2)}\rangle \leftrightarrow |\psi_B^{(1),(2)}\rangle$ are identical and thus these states accumulate the same phases, resulting in a factorable global phase. In the case of $\alpha = \beta$, the two singularities are precisely given in the orientation

$$\alpha = \beta = 2 \arctan(\sqrt{3} \pm \sqrt{2}) \approx 90^\circ \pm 54.74^\circ. \quad (4.18)$$

There exists a non-obvious geometric interpretation why no entanglement is generated exactly in this configuration, as all 4 separation distances between the states form the “harmonic mean” visualized in fig. 4.6. In the limit $\Delta x \ll L$, all dynamic phases for

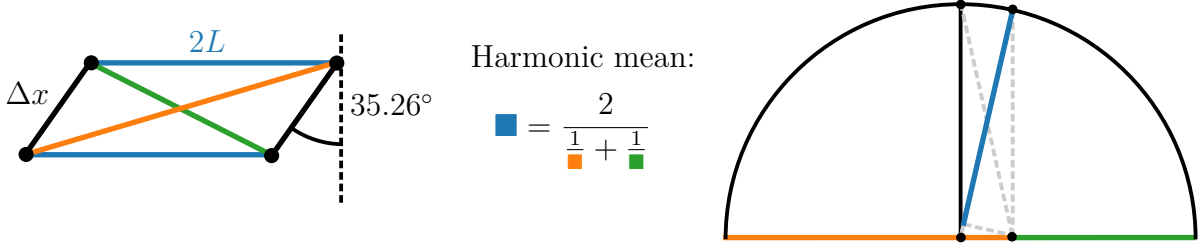


Figure 4.6: **left:** The system in the orientation $\alpha = \beta = 2 \arctan(\sqrt{3} - \sqrt{2})$. For $\Delta x \ll L$, all separation distances exactly form the *harmonic mean*. Here, the phases due to the mutual gravitational interaction precisely cancel out resulting in no entanglement. **right:** Geometric visualization of the harmonic mean.

the different cat-states can be factored in a global phase and thus resulting in a loss of entanglement. To avoid all these singularities, it is advisable to always choose $\alpha = -\beta$, where all orientations result in roughly similar entanglement times t_{\max} , at most only differing by a factor of 2.

It should come by no surprise that the different orientations exhibit different stabilities. Naturally, one would expect the orthogonal configuration to be much more sensitive to angular variations than the parallel one. In contrast, the parallel configuration should be much more stable against variations L , as no phase difference is induced between the two superposition states $|\psi_{A(B)}^{(1)}\rangle$ and $|\psi_{A(B)}^{(2)}\rangle$ of the particles A and B .

The effect of different orientations on the stability against angular variations and the behavior of the critical angular variation $\Delta\theta_{\text{crit}}$ is shown in fig. 4.7. As expected, the orthogonal configuration is the most stable against these kind of variations. This is, because the dephasing ultimately depends on the distance between the cat-state and the shield $L \pm \Delta x/2 \cos \theta \approx L \pm \Delta x/2(1 - \theta^2/2)$, which is a only second order effect of the angular variations θ . This explains the apparent “infinitely” good stability in the figure, as the analytical solution only uses first order approximations in θ . Exact numerical results however cap the stability at $\Delta\theta_{\text{crit,orthogonal}} \approx 7.3 \times 10^{-5}$ rad.

Respectively, the stability against distance variations ΔL_{crit} for different orientations is shown in fig. 4.8. Again aligning with expectations, the parallel configuration exhibits

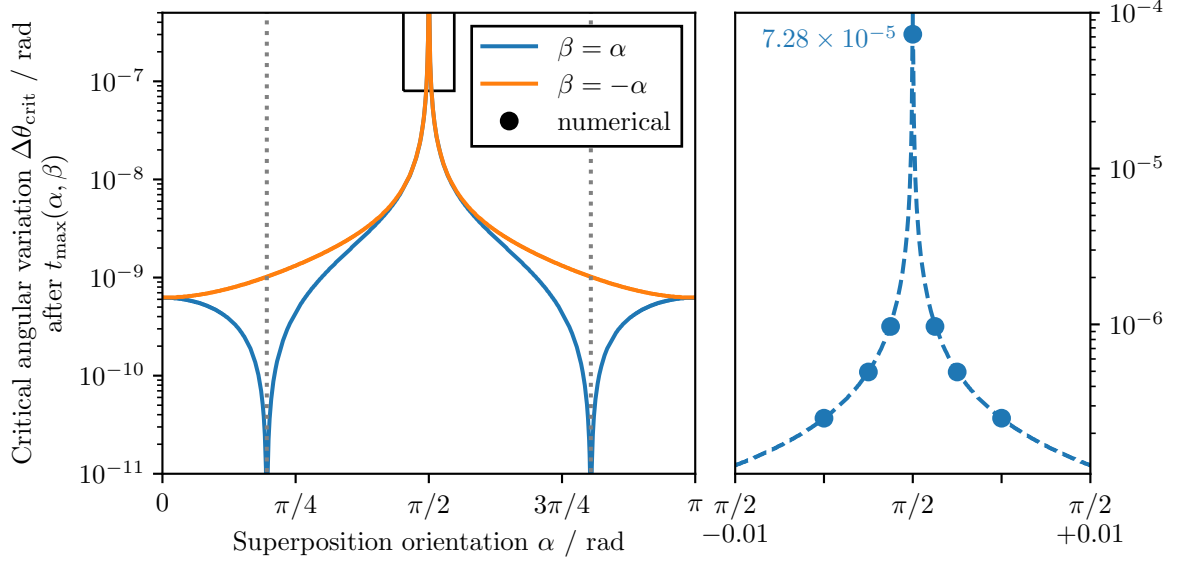


Figure 4.7: Critical angular variation $\Delta\theta_{\text{crit}}$ for different orientations after the time $t_{\text{max}}(\alpha, \beta)$. The **orthogonal orientation** magnified on the right is very stable against angular variations and only numerical methods show a finite stability value. The singularities in the left figure for $\alpha = \beta$ arise from the fact, that these orientations need infinite time to entangle as already seen in fig. 4.5.

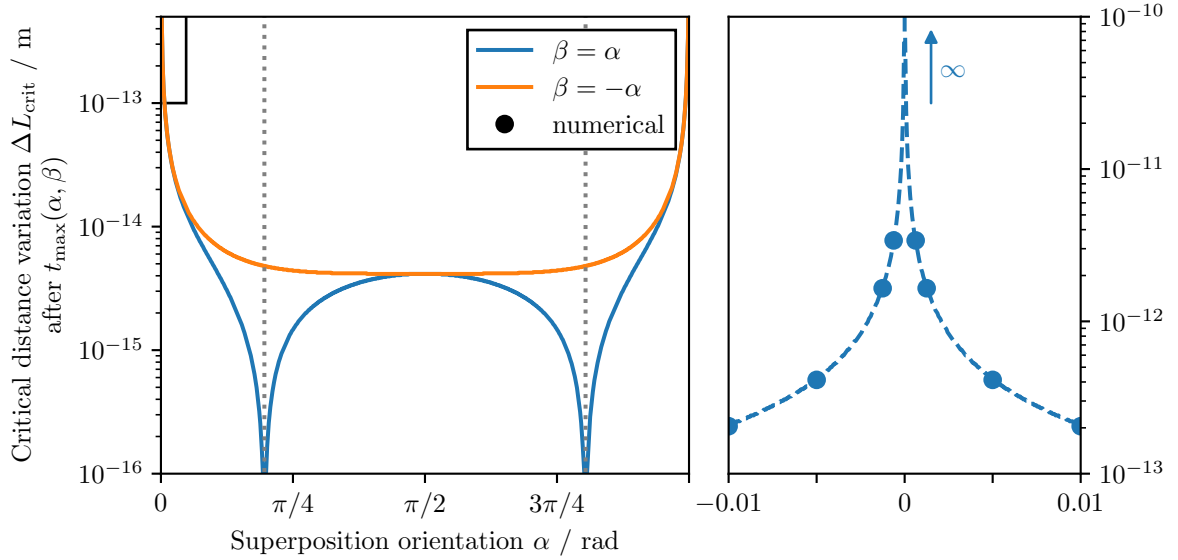


Figure 4.8: Critical variation in the particle-shield separation ΔL_{crit} for different orientations after a time $t_{\text{max}}(\alpha, \beta)$. Here, the **parallel orientation** (magnified on the right) is “infinitely” stable against placement variations.

an infinite stability. One could argue, that a for this to hold, the uncertainties in the angular placement have to be zero. As however seen in fig. 4.7, these variations are at most around $\sim 5 \times 10^{-5}$ rad and thus a realistic upper bound for the minimum required distance variations is given by $\Delta L_{\text{crit,parallel}} = \Delta L_{\text{crit}}(\alpha \approx 5 \times 10^{-5} \text{ rad}) \simeq 4 \times 10^{-11} \text{ m}$. It is important to keep in mind, that these bounds can be improved substantially by e.g. increasing the separation distance L , the particle size R or the superposition size Δx .

Considering these results, the parallel orientation seems to be the more stable and therefore favorable option, even if it requires coherence times t_{max} are twice as long. Keeping particle-shield separation variations below 0.01 pm in the orthogonal orientation - even smaller than size of a single atom - is extremely challenging, especially under the additional consideration of the thermal vibrations of the shield, which are in the same order of magnitude as seen later in chapter 5. With this framework on hand, it is possible to generate the stability diagram in fig. 4.9, showing the optimal orientation in which the most entanglement can be measured. For most combinations of ΔL and $\Delta\theta$, entanglement is exclusively given in either the parallel or orthogonal orientation.

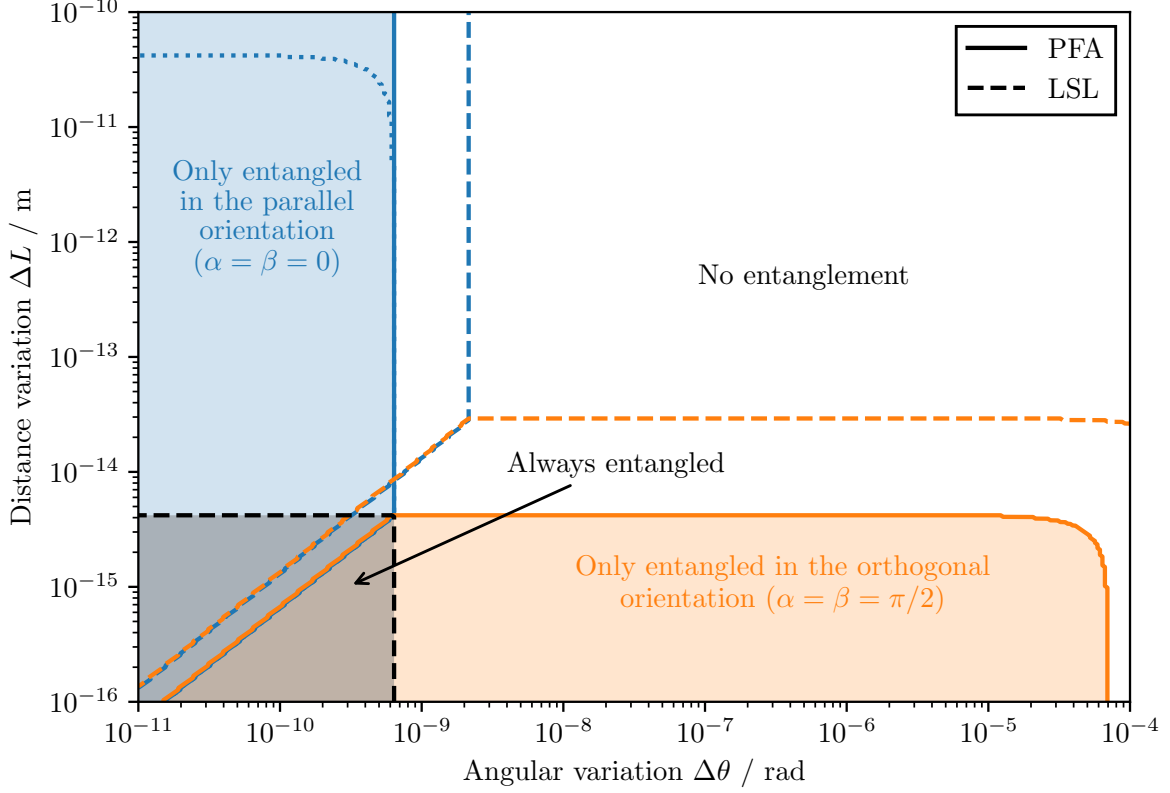


Figure 4.9: Optimal and most stable configuration for the orientation of the cat-states relative to the shield for different variations in the angle $\Delta\theta$ and in the separation distance ΔL . The used parameters for the particle are shown in table 4.1 and e.g. larger separations L would improve the stability boundaries significantly. Both models for the Casimir interactions are shown. In regions where entanglement is given regardless of the orientation (the bottom left), the the favorable orientation with “more” entanglement is colored. The blue dotted line corresponds to the realistic upper bound discussed in the text, where an additional angular variation of 5×10^{-5} rad as a worst-case estimation is assumed.

4.2.2 Separation, mass and superposition size

It is possible to improve the placement accuracies required in the initial placement of the particles by changing the parameters in table 4.1. The particle-shield separation L in particular can be adjusted easily over a wide range and one is only limited in the ability of trapping close to the shield (discussed in section 4.3) and the size of the experimental setup. The scaling of the critical angular variation $\Delta\theta_{\text{crit}}$ for different L is shown in fig. 4.10. A similar figure can be created for the change of ΔL_{crit} , but as

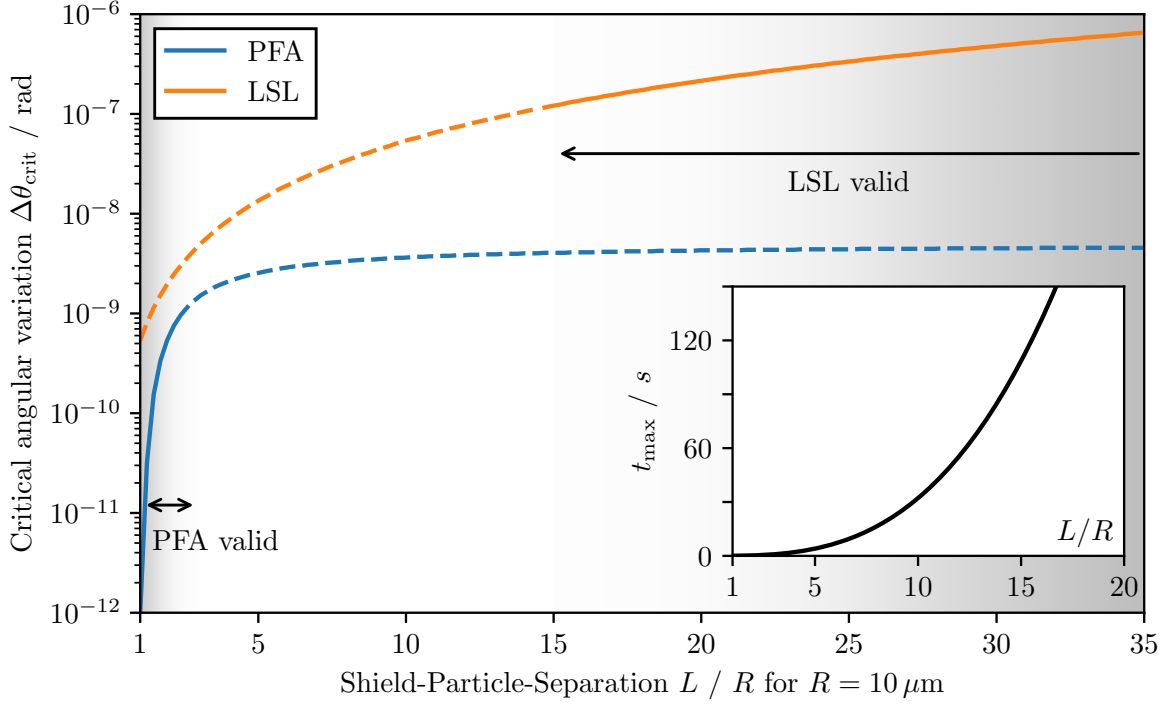


Figure 4.10: Stability against angular variations for increasing separation distances L in units of $R = 10 \mu\text{m}$ after a time $t_{\text{max}}(L)$. The dependence on the radius can be seen in fig. 4.11. Two models for the casimir-interaction are shown: The proximity-force-approximation (PFA) and the large-separation-limit (LSL). The regions outside the models validity are indicated with dashed lines. In the bottom right the time $t_{\text{max}}(L) \propto L^3$ is shown.

already discussed previously, the setup in the parallel orientation is very stable against variations in the separation distance, so only angular variations have to be considered.

It is intuitively clear, that a larger separation improves the stability as the relative effect of the angular variations $\sim \Delta x \sin \theta \ll L$ decreases and the Casimir potential tends towards zero. However, a larger separation also slows down the entanglement generation by $t_{\text{max}} \propto L^3$. The combination of both effects leads to the results shown in fig. 4.10. Both models for the Casimir interaction for either small separations $L \sim R$ (PFA) or large separations $L \gg R$ (LSL) have been considered and the regions of validity for each

model are shaded in gray. Looking at the dependence of the critical point eq. (4.13) on the separation, it becomes evident that (ξ is given by eq. (B.15))

$$\Delta\theta_{\text{crit}} \sim 1/(\xi t) \sim \frac{(L - R - d/2)^3}{t_{\text{max}}} \sim \frac{(L - R - d/2)^3}{L^3} \quad (4.19)$$

for small separations and similarly $\Delta\theta_{\text{crit}} \sim L^2$. For this approximations, it was additionally used that the Casimir force is much larger than the gravitational interaction for all $L \lesssim 3.2 \text{ m}$ (in fig. 4.10, the match is quantified by $R^2 = 0.99$).

Contrary to L , the size of the particle R and thus the mass M cannot be changed easily over a wide range of possible values. Estimations suggest, that masses of around $10^{-11} \text{ kg} \approx 5 \times 10^{-4} m_p$ could be possible to use for the detection of gravitationally induced entanglement [41, Timestamp 51:00]. Nevertheless, the effect of a larger particle on angular variations is analyzed and shown in fig. 4.11. The particles are most likely made

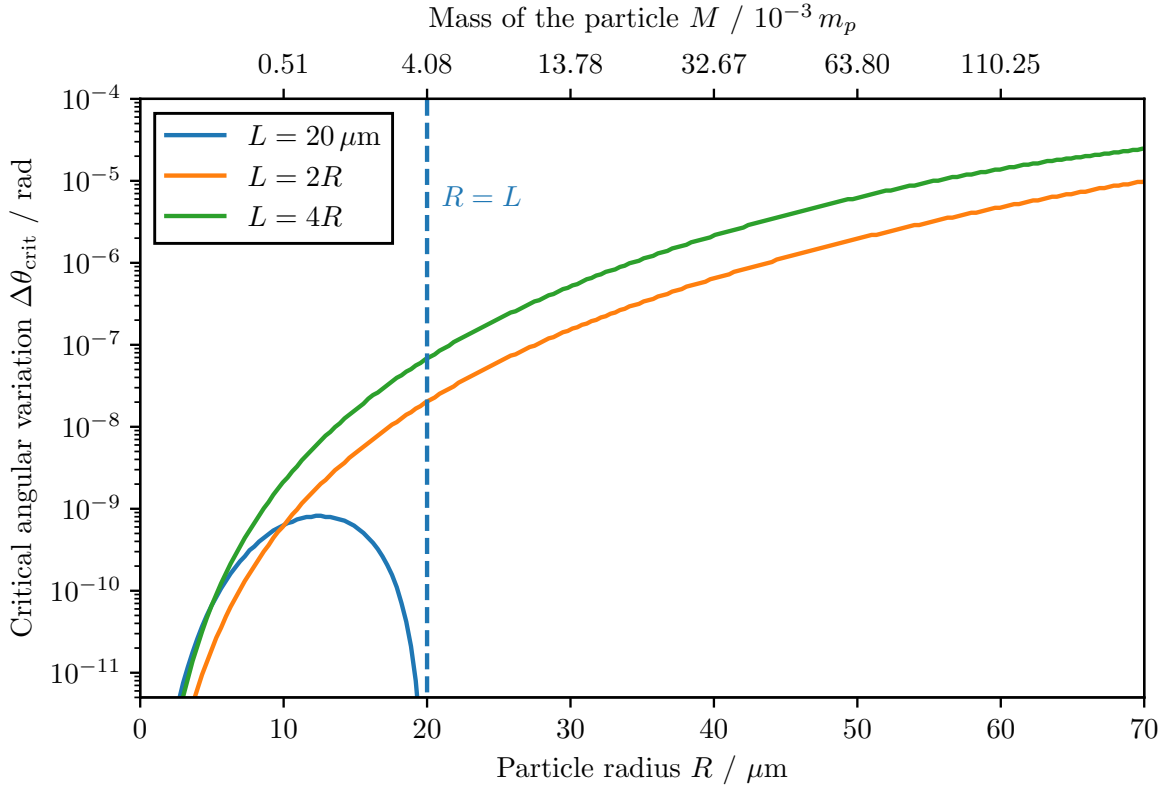


Figure 4.11: Critical angular variation $\Delta\theta_{\text{crit}}$ for different sized particles after a time $t_{\text{max}}(M)$. The mass of the corresponding particle in units of the Planck mass $m_p = \sqrt{\hbar c/G} \approx 2.176 \times 10^{-8} \text{ kg}$ is given on the top axis. For particles as large as the separation $R = L$, the surface-to-surface separation is almost zero, resulting in large casimir forces and thus no entanglement.

out of silica (SiO_2) with density $\rho_{\text{Silica}} = 2648 \text{ kg/m}^3$, as this material has been widely

used in experiments on levitated nanoparticles [65, 66]. Denser materials like lead or osmium [17] in magnetic traps could potentially be considered as the required particle radius and the number of atoms in a single particle are reduced. The entanglement generation fastens substantially for larger particles as t_{\max} scales with M^{-2} and thus effectively with R^{-6} . The dependence of $\Delta\theta_{\text{crit}}$ on R can be determined in first order to

$$\Delta\theta_{\text{crit}} \sim \frac{(L - R - d/2)^3}{Rt_{\max}} \sim \frac{(L - R - d/2)^3 R^6}{RL^3} \quad (4.20)$$

for small separations and in the special case where $L \propto R$, a scaling of $\Delta\theta_{\text{crit}} \sim (R - d/2)^3 R^2$ is expected. Both cases are shown in fig. 4.11.

Similarly to the particles size, the spatial extension of the coherent superposition of the center-of-mass motion Δx can most likely not be changed substantially. The delocalizations are, considering the current record in matter-wave experiments of 500 nm for 4×10^{-23} kg [31], smaller than the particles radius. In fig. 4.12 the effect of the superposition size on the critical angular variation is shown. A larger superposition would

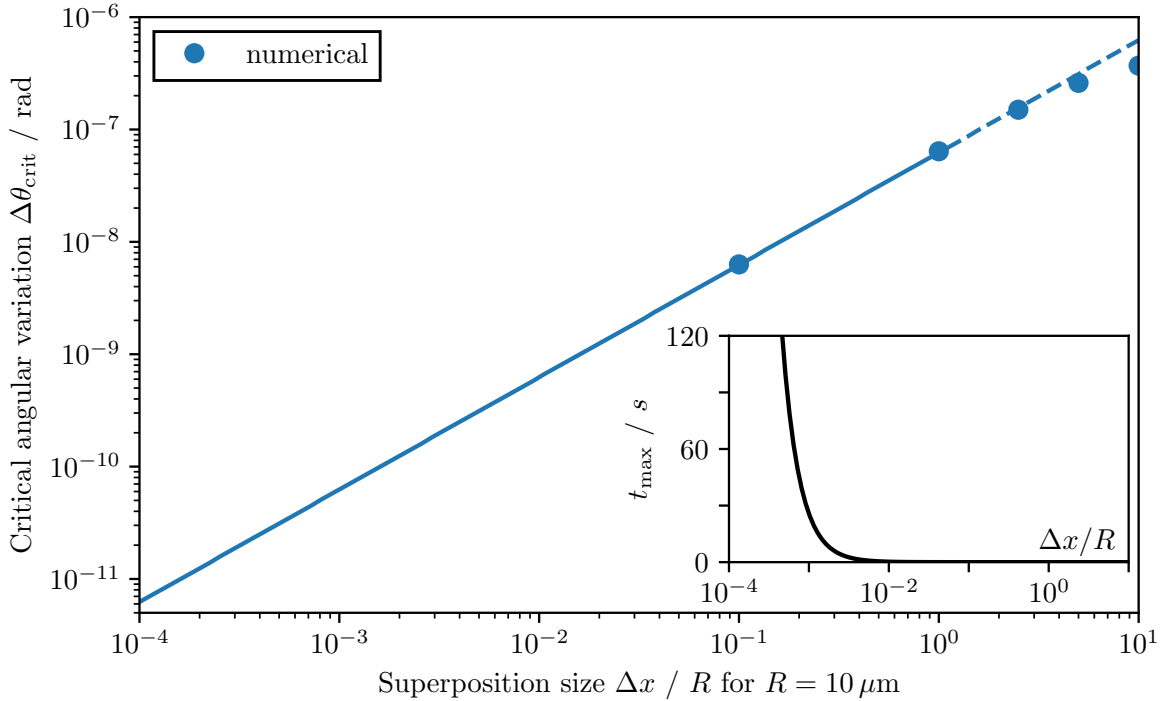


Figure 4.12: Effect of the superposition size Δx on the critical angular stability $\Delta\theta_{\text{crit}}$ after a time $t_{\max}(\Delta x)$. For $\Delta x \gtrsim R$, numerical results are used. In the lower left, the time $t_{\max} \propto (\Delta x)^{-2}$ is shown, until maximum entanglement is reached. For $\Delta x \ll R$, the resulting relation between Δx and $\Delta\theta_{\text{crit}}$ is linear.

increase the entanglement generation as the relative phase differences between the states increase, leading to $t_{\max} \propto 1/(\Delta x)^2$. Simultaneously, a larger superposition size increases

the effect of angular variations, as they depend on $\sim \Delta x \sin(\theta)$. The effective scaling of the angular variations is therefore linear $\Delta\theta_{\text{crit}} \sim \Delta x$, as seen in fig. 4.12 ⁸.

4.3 Trapping the particle

The presence of a shield introduces potential challenges to the stability of the particle trap. Levitated particles are typically trapped and cooled in ultra-high vacuum using magnetic, optical or electrical radiofrequency Paul traps [42]. These traps differ in the trapping mechanism, but if the particle is cooled close to the ground state, all trapping potentials can be considered “harmonic” with trapping frequency $\omega_{\text{trap}} = 2\pi \times f$. The strength of the trapping potential $V \propto f^2$ varies across trap types, with frequencies typically ranging from 1 Hz – 1 kHz for magnetic traps [66] up to 10 kHz – 300 kHz for optical traps [42].

If the particle is positioned close to the shield, the Casimir interaction may destabilize the trap or pull the particle onto the shield. The total potential $V_{\text{tot}} = V_{\text{trap}} + V_{\text{Casimir}}$ is shown in fig. 4.13 for stable and unstable configurations. The attractive Casimir force displaces the equilibrium trap position closer to the shield by a distance Δx given by

$$\Delta x = \frac{|\nabla V_{\text{Casimir}}|}{m(2\pi f)^2} = \frac{2\hbar c \pi^3}{720} \left(\frac{\varepsilon_r - 1}{\varepsilon_r + 1} \right) \varphi(\varepsilon_r) \frac{R}{\mathcal{L}^3} \frac{1}{m(2\pi f)^2}. \quad (4.21)$$

For $f = 1$ kHz and $L = 2R = 20 \mu\text{m}$, this shift is negligibly small, as it is in the order of $\Delta x \approx 10^{-13}$ m.

To determine the stability of a trapped particle with mass $M \propto R^3$ in a trap with frequency f placed at a distance $L_0 > R$ in front of the shield, the number of bound energy-eigenstates in the potential V_{tot} is considered. From fig. 4.13 it becomes clear, that as long as the particles thermal energy is well below E_0 , the trap is stable and the particle is bound. Here, E_0 is defined as the local maximum of the potential

$$E_0 = \max_{L \in (R, L_0)} (V_{\text{trap}} + V_{\text{Casimir}}). \quad (4.22)$$

If no such local maximum exists, i.e.

$$\frac{\partial}{\partial L} (V_{\text{trap}} + V_{\text{Casimir}}) > 0 \quad (4.23)$$

for all $L \in (R, L_0)$, the trap is unstable. Regions of instability are shown in white in the stability diagram fig. 4.14. In the general case, the stability can be measured by computing the number of bound eigenstates $n(E \leq E_0)$ and comparing them with the number of thermally excited states \bar{n} . At a temperature T on average

$$\bar{n} = \frac{1}{e^{\beta\hbar\omega} - 1} \quad (4.24)$$

⁸Here it is shown in a double-logarithmic plot. The relation between Δx and $\Delta\theta_{\text{crit}}$ is nevertheless linear.

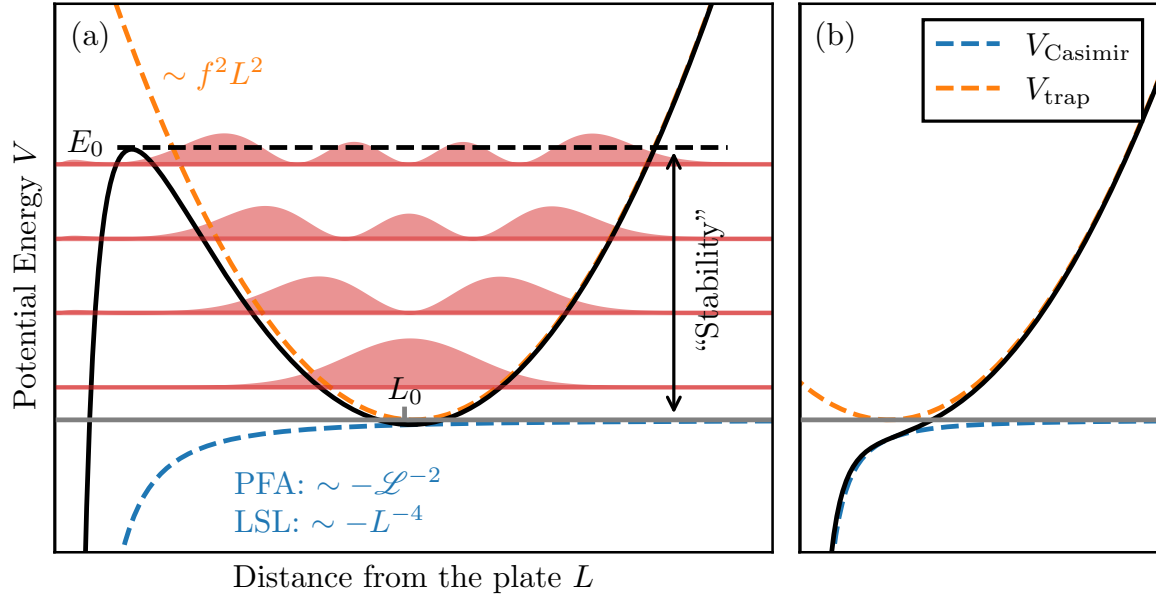


Figure 4.13: Visualization of the potential as an overlay of the harmonic trapping potential $V_{\text{trap}} = m(2\pi f)^2 L^2/2$ and the casimir potential V_{Casimir} . f is the trapping frequency and L_0 the position of the trap. In red, eigenstates of the potential are visualized offset by the eigen-energies. **(a)** Almost harmonic bounded potential which can hold the particle, if its energy is less than E_0 . **(b)** Potential with no bounded states. Here, trapping is not possible.

states are occupied, where $\beta = 1/k_B T$ and $\omega = 2\pi f$. This is true, as long as the potential is assumed to be harmonic, which is, as seen shortly, a good approximation. To find the number of possible bound energy-eigenstates in the potential, the **WKB-approximation** is used. In this approximation, the energy of the n -th eigenstate of a smooth and appropriately slow varying potential $V(x)$ can be calculated using [67, p. 163]

$$\int_{x_1}^{x_2} dx \sqrt{2m(E - V(x))} = \left(n + \frac{1}{2}\right) \pi \hbar, \quad (4.25)$$

where $V(x_1) = V(x_2) = E$ are two turning points corresponding to energy E . Conversely, it is possible to use this approximation to numerically estimate the total number of bound states in the potential $V = V_{\text{trap}} + V_{\text{Casimir}}$ using

$$n(E_0) \approx \frac{1}{\hbar\pi} \int_{x_1}^{x_2} dx \sqrt{2m(E_0 - V(x))}, \quad (4.26)$$

which is closely given (highest deviation around 40%; averaged relative error $\sim 0.9\%$) by the harmonic approximation $n(E_0) \sim E_0/\hbar\omega$. The resulting number of bound states is shown in fig. 4.14 as well as the stability boundaries at specific temperatures where $\bar{n} = n(E_0)$. In these calculations, tunneling effects through the potential boundary at E_0 are neglected, as they should not influence the results much considering the large number of bound eigenstates. It turns out, that regardless the type of the trap, a successful trapping even at room temperature should be possible as long as the particle is placed appropriately far away from the trap. The ability to trap and levitate the masses is therefore not significantly impaired by the presence of the Faraday shield.

4.4 Discussions

The preceding results highlight, that the proposed Faraday shield in experiments on measuring gravitationally induced entanglement entail significant engineering challenges, particularly due to the strict accuracy requirements for particle placement. Variations must be minimized to a precision of approximately $\Delta L \simeq 10^{-10}$ m and $\Delta\theta \simeq 10^{-9}$ rad, which are extremely stringent. Even the rotation of the earth ($\omega_{\text{Earth}} \approx 7.3 \times 10^{-5}$ rad/s) could potentially be problematic, because if small fluctuations in the measurement time $\Delta t \gtrsim 10^{-4}$ s are present, this corresponds to an additional angular uncertainty of $\omega_{\text{Earth}} \Delta t \gtrsim \Delta\theta_{\text{crit}}$. Adjustments to the experimental parameters in table 4.1 have to be made, where especially the separation distance L and the orientation are easily changeable.

The parallel configuration is very stable against variations in the distance and might therefore be favorable (see in fig. 4.9). The separation L can be freely chosen and larger distances reduce the effect of placement variations as seen in fig. 4.10, while simultaneously increasing the required coherence time $t_{\text{max}} \propto L^3$.

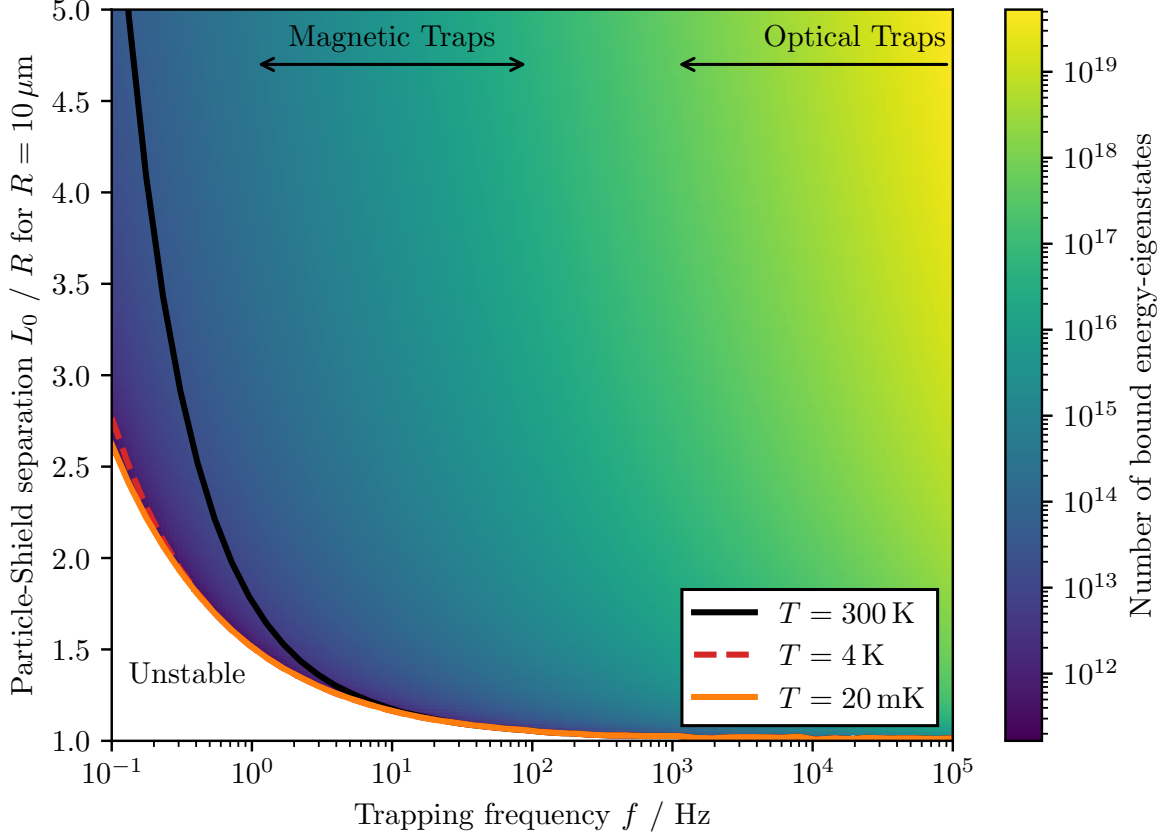


Figure 4.14: Stability diagram for different trapping frequencies $f = \omega/2\pi$ and particle-shield separations L_0 . The number of bound energy-eigenstates for each combination of f and L_0 are calculated using the WKB-approximation. The number of thermally occupied states \bar{n} at different Temperatures is overlaid. As an example, for $f = 1$ Hz, $\bar{n}(T = 300 \text{ K}) \approx 10^{13}$ states are thermally occupied. All regions below these boundaries are unstable. An increase in the radius R and thus the mass M improves the regions of stability massively.

It could also be argued that at a distance of $L \geq 100 \mu\text{m} = 10R$ (compare to section 2.3), the Faraday shield would no longer be required because the Casimir forces are approximately ten times weaker than gravitational interactions. However, the loss of entanglement due to angular and distance variations is not purely due to the Casimir forces between the particle and the shield. The gravitational coupling also depends on the placement, so that a complete removal of the shield does not fully eliminate the need for high placement accuracy. Without the shield and by gravitational interaction alone, the critical variations are given by $\Delta\theta_{\text{crit, ideal}} = 1.1 \times 10^{-3} \text{ rad}$ and $\Delta L_{\text{crit, ideal}} = 7 \times 10^{-4} \text{ m}$, which should not pose an engineering problem.

Other parameters, such as particle size and superposition size, may not be easily adjustable without increasing the complexity of quantum control. Furthermore, particle trapping and levitation is not a limiting factor, as stable trapping is achievable for various configurations (section 4.3).

A primary aim of this thesis is to assess whether the Faraday shield allows particles to be brought closer together to enhance gravitational entanglement and reduce coherence times. Using the previous results, a optimal experimental parameter space can be determined. The optimization-goal can be expressed as the following:

One wants to get *as much entanglement as possible* in the *shortest time possible* while allowing for the *largest uncertainties* in the state preparation and considering the limitations in the particles mass as well as in the superposition size.

Without specific constraints, a general optimization is impossible because (if the mass M and the superposition size Δx is fixed) coherence time $t \propto L^3$ (eq. (4.16)) and critical angular variation $\Delta\theta_{\text{crit}} \propto (L - R)^3/L^3$ (for small separations) or $\Delta\theta_{\text{crit}} \propto L^2$ (for $L \gg R$) cannot be optimized simultaneously. With constraints such as target coherence time t_{target} and/or a minimum placement accuracy, the required sphere-plate separation L as well as maximum measurable entanglement can be determined using the following steps:

1. Let us assume that the size of the particle R and consequently the mass $M = 4/3\pi R^3 \rho_{\text{Silica}}$ as well as the superposition size Δx are fixed. An increase in either of them would have a positive effect of the optimization goal stated above, as the time t_{max} decreases and the stability against placement variations increases simultaneously.
2. Given placement accuracies in angular and separation variations determine the optimal orientation α, β of the setup as seen in fig. 4.9. Experimentally reachable coherence times may influence this decision slightly by taking fig. 4.5 into account. Most likely, the most stable orientation is going to be the parallel one with $\alpha = \beta = 0$.
3. The following ratio given by the entanglement rate eq. (4.16)

$$\frac{M^2(\Delta x)^2}{L^3} t_{\text{max}} = \frac{4\pi\hbar}{G} \left| \sin \alpha \sin \beta - \frac{1}{2} \cos \alpha \cos \beta \right|^{-1} \sim 10^{-23} \text{ kg}^2\text{s/m} \quad (4.27)$$

is fixed therefore [41].

4. In general it is possible to measure at an earlier time $t_{\text{target}} = \tau t_{\text{max}}$ (i.e. the coherence time) with $\tau \leq 1$, where less entanglement has been generated but a larger stability against placement variations can be tolerated (see fig. 4.4). Putting all assumptions together, the product

$$\tau L^3 = \frac{t_{\text{target}} G M^2 (\Delta x)^2}{8\pi\hbar} = \text{const.} \quad (4.28)$$

of measurement time and particle-shield separation is constant.

5. In the parallel orientation, the distance variations don't matter as the system is very stable against variations in the particle-shield separation. The critical angular variation however scales like $\Delta\theta_{\text{crit}} \sim (L - R)^3/L^3$ for small distances and like $\Delta\theta_{\text{crit}} \sim L^2$ at larger distances as shown in fig. 4.10. It is therefore possible to determine the minimum separation $L_{\text{min}} > R$ for a given placement accuracy.
6. Using the required separation, one can calculate $\tau \in (0, 1]$ using eq. (4.28) and look up the maximal possible entanglement in fig. 4.4 after an evolution time τt_{max} .

As an example, the radius is fixed at $R = 10\,\mu\text{m}$ and the superposition size is $\Delta x = 100\,\text{nm}$. Let's say that such a particle can be placed with an accuracy of $\Delta\theta = 5 \times 10^{-8}\,\text{rad}$ and a coherence time of 1 s is reachable. Using the steps outlined above, the required minimum particle-shield separation is around $L \approx 8R$ and the maximal amount of measurable entanglement is given by $E_N \approx 6.0 \times 10^{-2}$. For more entanglement, either a heavier particle, a larger superposition size, a higher placement accuracy or larger coherence times are required. It is therefore possible to bring the particles closer together than without the Faraday shield and still measure entanglement. One is only limited by the placement accuracy and repeatability.

5 The consequences of a thermal shield

The primary goal of the Faraday shield is to enable particle separations closer than what would be possible without the shield, thereby enhancing gravitational interaction and reducing the required coherence times. To reach separations $L \lesssim 100 \mu\text{m}$, mutual Casimir interactions between the particles have to be shielded, as discussed in section 2.3. Until now, the shield's dynamics and properties have been ignored. However, at non-zero temperatures, thermal vibrations of the shield could significantly affect entanglement generation. In this chapter, an estimation of the required shield size is given followed by examining the impact of thermal vibrations for both large and small shields on entanglement generation. In the experiment, the trapped particles are cooled to their motional ground state to enable effective quantum control and the generation of spatial superpositions. Liquid helium at $T \approx 4 \text{ K}$ is commonly used for cooling but cryogenic dilution refrigerators can cool small setups down to temperatures as low as $T \approx 20 \text{ mK}$ [68]. These temperatures serve as reference points for all relevant calculations.

5.1 Thickness and size of the shield

The required thickness d and the radius r_s of the spherical shield to effectively block electromagnetic interactions between the particles can be estimated by analyzing the properties of a physical conductive material with high electric conductivity σ . For an almost perfect shielding, a superconducting shield may be considerable as well. The transmission T of electromagnetic waves through a physical shield is given by [69]

$$T = \left| \frac{\mathbf{E}_{\text{after}}}{\mathbf{E}_{\text{before}}} \right| = \frac{2}{Z_0 \sigma d} \quad (5.1)$$

where $Z_0 = 377 \Omega$ is the impedance of free space (assuming the shield is placed in a vacuum or in air). The electric conductivity σ is highly dependent on the temperature [70, p. 284-286], decreasing approximately with $1/T^5$ at low temperatures⁹. Copper offers a strong electric conductivity of $\sigma = 59.6 \times 10^6 \text{ S/m}$ at room temperature and measured data showing even $\sigma(T = 10 \text{ K}) \approx 1.5 \times 10^{10} \text{ S/m}$ at 10 K [71].

⁹This behavior is valid for temperatures below the Debye temperature ($\Theta_D = 343 \text{ K}$ for copper). At the low temperatures used in the experiment, this model accurately describes the conductivity of metals [71].

To estimate the shield's thickness, the primary criterion used, is that gravitational interactions should dominate the entanglement generation. Other mutual interactions between the particles, such as Coulomb or Casimir forces, must be sufficiently suppressed by the shield. The **entanglement rate** Γ quantifies the build-up of entanglement over time

$$\Gamma = \left. \frac{d}{dt} E_N(\rho) \right|_{t=0}, \quad (5.2)$$

where E_N is an appropriate entanglement measure - in this case the logarithmic negativity [36] introduced in section 2.2. For gravitational interactions, the entanglement rate in the parallel orientation is given by using eq. (2.17) as

$$\Gamma_{\text{Gravity}} = \frac{GM_A M_B \Delta x_A \Delta x_B}{16\hbar L^3 \log 2} = \frac{G\pi^2 R^6 \rho_{\text{Silica}}^2 (\Delta x)^2}{9\hbar L^3 \log 2}. \quad (5.3)$$

where in the last step $M_A = M_B = 4/3\pi R^3 \rho_{\text{Silica}}$ and $\Delta x_A = \Delta x_B \equiv \Delta x$ was used. The entanglement rate for non-gravitational interactions, such as Coulomb or Casimir forces, must be significantly smaller than the gravitational entanglement rate, ideally by a factor $\chi \gg 1$. This ensures that any measured entanglement is primarily due to gravitational interactions. In the following sections, estimations about the thickness and size of the shield are made, to effectively screen Coulomb and Casimir forces.

5.1.1 Shielding Coulomb-Interactions

The primary role of the Faraday shield is to block electromagnetic interactions between particles. Experimentally, it may be beneficial for the particles to carry a small amount of charge, enabling the use of electrostatic traps with high trapping strength and large controllability [42]. The Coulomb interaction potential between two charged particles is given by

$$V = \frac{1}{4\pi\epsilon_0} \frac{q_A q_B}{2L} \quad (5.4)$$

where $\epsilon_0 = 8.8542 \times 10^{-12} \text{ A}^2 \text{ s}^4 \text{ m}^{-3} \text{ kg}^{-1}$ is the permittivity of free space and we assume that each particle carries one electron charge $|q_{A(B)}| = e = 1.6022 \times 10^{-19} \text{ C}$. This interaction mimics the form of the gravitational potential and can similarly induce entanglement with a entanglement rate

$$\Gamma_{\text{Coulomb}} = \frac{T |q_A q_B| (\Delta x)^2}{64\pi\epsilon_0 \hbar L^3 \log 2}. \quad (5.5)$$

The shield suppresses the coupling by a factor of T . Requiring $\Gamma_{\text{Gravity}} > \chi \Gamma_{\text{Coulomb}}$, the minimum thickness of the shield can be calculated by using eq. (5.1) as

$$T \frac{|q_A q_B|}{64\pi\epsilon_0} \chi < \frac{G\pi^2 R^6 \rho_{\text{Silica}}^2}{9} \quad (5.6)$$

$$\iff d > \frac{9}{32} \frac{1}{Z_0 \sigma} \frac{1}{\pi^3 \epsilon_0 G \rho_{\text{Silica}}^2} \frac{e^2}{R^6} \chi. \quad (5.7)$$

The thickness strongly depends on the particles size R , and large or heavy particles will favor gravitational entanglement generation. Assuming the particles are silica nanospheres with parameters given in table 4.1, a minimum shield-thickness of $d \approx 10 \text{ nm}\chi$ at 4 K and of $d \approx 2.5 \mu\text{m}\chi$ at room temperature is required. At low temperatures, a realistic shield thickness could therefore be $d = 100 \text{ nm}$, balancing engineering practicality and electromagnetic suppression. Exact estimations however depend on the realization of the experiment as well as the precision in which the evolved state is measurable.

Electrostatic fields still can propagate around the finite-sized Faraday shield and potentially induce entanglement. It is possible to estimate the required shield radius r_s to block a specific amount η of the electric field (see appendix A.4):

$$\frac{r_s}{L} = \sqrt{\frac{1 - (1 - \eta)^2}{(1 - \eta)^2}} \quad (5.8)$$

The results are visualized in fig. 5.1. The shield's transmission T should therefore be

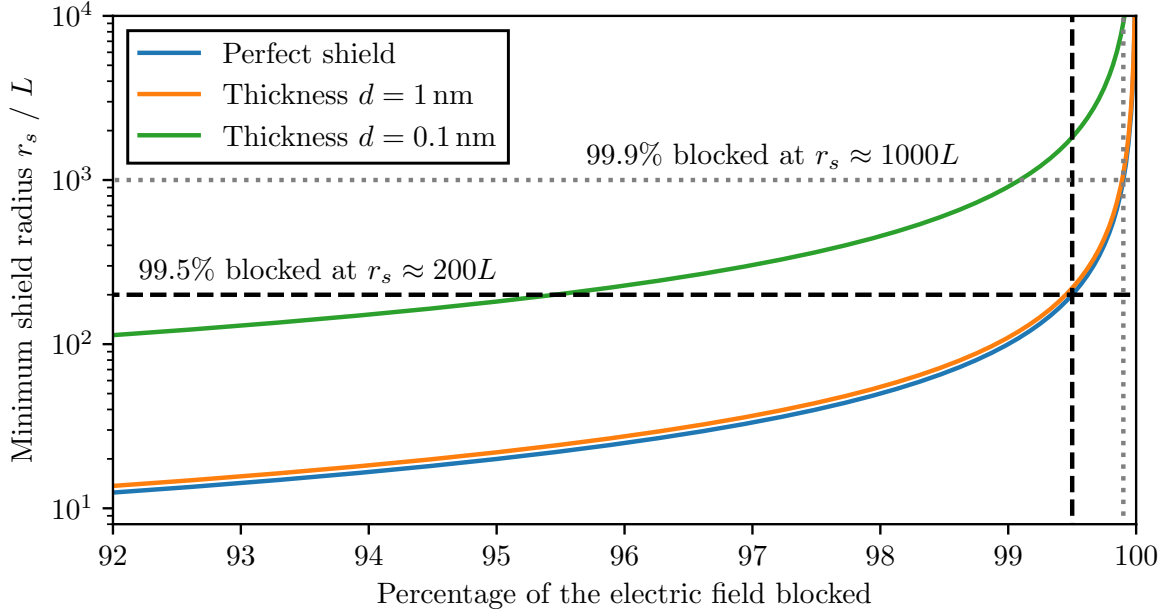


Figure 5.1: Shield radius as a function of the shielding effectiveness η for an ideal shield. Additionally, a real shield with varying thicknesses d is considered at $T = 300 \text{ K}$. To achieve shielding of 99.5 – 99.9% ($\eta = 0.995 - 0.999$), a radius of $r_s = 200 - 1000L$ is needed.

modified to $\tilde{T} = T\eta + (1 - \eta)$, where the shielding effectiveness η depends on r_s as given by eq. (5.8). Modifying eq. (5.6), a minimum effectiveness η_{\min} for sufficient shielding of

$$\eta_{\min} \approx 1 - \frac{64\pi^3 \varepsilon_0 G R^6 \rho_{\text{Silica}}^2}{9e^2} \quad (5.9)$$

can be approximated. Using again the parameters from table 4.1, a minimum shielding of $\eta_{\min} \gtrsim 0.99997$ and thus a radius of $r_s \gtrsim 28000L \approx 60 \text{ cm}$ is required. Depending on the experimental setup, such a shield might be too large for all practical purposes and it may be beneficial to choose heavier masses ($\tilde{M} \sim 4M$) to reduce the shield size to the orders of $\sim 1 \text{ cm}$. Due to practicality, a shield with $r_s = 1 \text{ cm}$ is used in the following calculations. Uncharged particles would eliminate the Coulomb interactions and therefore reducing the shield's size and thickness to only shield mutual Casimir interactions.

5.1.2 Shielding Casimir-Interactions

Similarly to Coulomb interactions, it is possible to estimate the required thickness for a shield to sufficiently block Casimir interactions. The Casimir potential between the spheres with radius R separated by $2L$ is given in first order by [40]

$$V = -\frac{23\hbar c}{4\pi \cdot 128L^7} \left(\frac{\varepsilon_r - 1}{\varepsilon_r + 2} \right)^2 R^6. \quad (5.10)$$

The corresponding entanglement rate is calculated similar to before by expanding the potential in small Δx and computing the logarithmic negativity:

$$\Gamma_{\text{Casimir}} = T^2 \frac{161}{4096} \frac{cR^6(\Delta x)^2}{\pi L^9 \log 2} \left(\frac{\varepsilon_r - 1}{\varepsilon_r + 2} \right)^2. \quad (5.11)$$

The dependence on T^2 arises because Casimir forces are second order effects in the dipole-dipole interaction [46]. Requiring gravitational entanglement generation to dominate, $\Gamma_{\text{Gravity}} > \chi \Gamma_{\text{Casimir}}$, leads to

$$T^2 \frac{161cR^6}{4096\pi L^6} \left(\frac{\varepsilon_r - 1}{\varepsilon_r + 2} \right)^2 \chi < \frac{G\pi^2 \rho_{\text{Silica}}^2 R^6}{9\hbar} \quad (5.12)$$

$$\iff d > \sqrt{\frac{1449}{4096} \frac{c\hbar}{G\pi^3} \frac{2}{Z_0\sigma\rho L^3} \frac{\varepsilon_r - 1}{\varepsilon_r + 2}} \sqrt{\chi}, \quad (5.13)$$

where again $T = 2/Z_0\sigma d$ from eq. (5.1) was used. For large separations, the shield thickness can be arbitrarily low, as Casimir forces vanish and at separations of $L \gtrsim 100 \mu\text{m}$, the shield might not be required at all (compare section 2.3). Assuming two identical silica nano-spheres with parameters given by table 4.1, the required minimum thickness is between $4 \times 10^{-11} \text{ m} \sqrt{\chi}$ at 4 K and $10 \text{ nm} \sqrt{\chi}$ at room temperature. This is much thinner than what is required for shielding Coulomb interactions. The factor ε_r modifies the thickness only by up to a constant factor of ≤ 1 and is therefore ignored for worst-case estimations.

However, very thin shields lose mechanical rigidity, leading to enhanced vibrational excitations and potential instabilities. Vibrational frequency and thus the vibrational energy depends linearly on the shield's thickness, making thinner shields prone to large decoherence due to thermal vibrations. A detailed analysis of these effects is provided in the subsequent section.

5.1.3 Gravitational effects of the shield

The gravitational interaction between the masses and the shield is generally neglected because it has no significant impact on the entanglement generation between the particles. The only potential effect is indirect entanglement mediated by the thermal oscillations of the shield, as both masses couple gravitationally to it. However, as shown in section 5.3, this second-order effect is very weak and does not pose a problem, since it still represents gravitationally mediated entanglement - which is the focus of the experiment anyway. The gravitational force between a sphere with mass M and an infinitesimal mass segment $dm = r d\rho_{\text{Cu}} dr d\varphi$ of the shield made of copper with density $\rho_{\text{Cu}} = 8960 \text{ kg/m}^3$ at a distance r from the shield's center is given by

$$d\mathbf{F} = \frac{GMdm}{\ell} \hat{\ell} \Rightarrow dF_z = \frac{GM r \rho_{\text{Cu}} d}{\ell^2} dr d\varphi \cos \theta, \quad (5.14)$$

where $\ell^2 = r^2 + L^2$ denotes the distance between the sphere and the mass segment and $\theta = \arccos L/\ell$ is the angle between them. The total attractive force between the mass and the shield with radius r_s is therefore

$$F_z = GM \rho_{\text{Cu}} d L \int_0^{r_s} dr \int_0^{2\pi} d\varphi \frac{r}{(r^2 + L^2)^{3/2}} = 2\pi GM \rho_{\text{Cu}} d \left(1 - \frac{L}{\sqrt{L^2 + r_s^2}} \right). \quad (5.15)$$

For large shields $r_s \rightarrow \infty$ this is independent of the particle-shield separation L . For a shield with thickness $d = 100 \text{ nm}$ and a silica particle with parameters given in table 4.1, the attraction force is around $F_{\text{particle-shield}} \approx 4.1 \times 10^{-24} \text{ N}$ which is comparable with the attraction gravitational attraction force between the two particles themselves at $F_{\text{particle-particle}} \approx 5.0 \times 10^{-24} \text{ N}$ but is much weaker than the Casimir attraction between the particle and the shield with $F_{\text{Casimir}} \approx 1.4 \times 10^{-17} \text{ N}$. Therefore, the gravitational effect of the shield can be neglected in all practical calculations.

5.2 Thermal shield vibrations

A spherical plate of radius r_s clamped at its edge, can vibrate in distinct modes characterized by indices (k, l) , where $k \in [1, \infty)$ and $l \in [0, \infty)$. The exact vibrational frequencies ω_{kl} and mode shapes u_{kl} are described by Bessel functions. In fact, one of the first occurrences of these functions is linked to Euler's study of vibrating perfectly flexible and infinitely thin membranes [72]. For a plate of a physical material with density ρ and thickness d , vibrations are described by the differential equation [73, p. 490]

$$D \nabla^2 \nabla^2 u = -\rho d \ddot{u} \quad (5.16)$$

where D is a flexural rigidity constant, dependent on material properties of the plate like Young's modulus E and the Poisson ratio ν in the form

$$D = \frac{d^3 E}{12(1 - \nu^2)}. \quad (5.17)$$

The general solution of this differential equation is expressed terms of Bessel functions as (derived in Ref. [73, p. 490-495])

$$u_{kl}(r, \theta, t) = \left[J_l(\beta_k r) - \frac{J_l(\beta_k r_s)}{I_l(\beta_k r_s)} I_l(\beta_k r) \right] \cos(l\theta + \phi_1) \sin(\omega_{kl}t + \phi_2) \quad (5.18)$$

with

$$\beta_k = \frac{\tilde{r}_k}{r_s} \quad \text{and} \quad \omega_{kl} = \frac{\tilde{r}_k^2}{r_s^2} \sqrt{\frac{D}{\rho d}} = \tilde{r}_k^2 \frac{d}{r_s^2} \sqrt{\frac{E}{12\rho(1-\nu^2)}}. \quad (5.19)$$

Here, \tilde{r}_k is the k -th root of the equation

$$J_l(\tilde{r}_k)I_{l+1}(\tilde{r}_k) + I_l(\tilde{r}_k)J_{l+1}(\tilde{r}_k) = 0. \quad (5.20)$$

The phases ϕ_1 and ϕ_2 are determined by initial conditions and represent rotational and temporal offsets. The shape u_{kl} of the first 12 modes (k, l) at time $t = (\pi n - \phi_2)/\omega_{kl}$, $n \in \mathbb{Z}$ are shown in fig. 5.2. In general, any possible vibration of the plates can be decomposed into a sum of these modes u_{kl} . The amplitude \hat{z}_{kl} depends on temperature T and is treated as the position operator of a quantum harmonic oscillator with frequency ω_{kl} . The expectation value of the amplitude $\langle \hat{z} \rangle$ is obviously zero and the variance $(\Delta \hat{z})^2 = \langle \hat{z}^2 \rangle - \langle \hat{z} \rangle^2$ of a thermally occupied harmonic oscillator at temperature T is given by (derivation in appendix A.5)

$$(\Delta \hat{z}_{kl})_T^2 = \frac{\hbar}{2\tilde{m}\omega_{kl}} \coth\left(\frac{\hbar\omega_{kl}}{2k_B T}\right) \approx \frac{k_B T}{\tilde{m}\omega_{kl}^2}, \quad (5.21)$$

where $\hbar\omega \ll k_B T$ was used in the last step and $k_B = 1.3806 \times 10^{-23}$ J/K is the Boltzmann constant. The *effective mass* \tilde{m} of the mode, considering the mode's shape, can intuitively be estimated by the average amplitude of the mode

$$\tilde{m} = m \frac{1}{\pi r_s^2} \int_0^{r_s} dr \int_0^{2\pi} r d\theta u_{kl}(r, \theta, t) \quad (5.22)$$

with $m = \rho\pi r_s^2 d$ being the total mass of the plate. The amplitude scales therefore as $\Delta z_{kl} \propto \omega^{-1}$ at high temperatures or for low frequencies.

It is additionally interesting to consider the scaling of the amplitudes Δz for shields with varying sizes r_s . According to eq. (5.19), the frequency $\omega \propto r_s^{-2}$ increases quadratically as the shield radius decreases. Simultaneously, the effective mass $\tilde{m} \sim r_s^2$ in eq. (5.22) increases also quadratically with the shield's size, consequently resulting in linear dependence of $\Delta z \sim r_s$ for $\hbar\omega \ll k_B T$.

The effect of infinite modes

For a shield with radius $r_s = 1$ cm $\gg R$ (referred to as the “large shield”) and thickness $d = 100$ nm made out of copper with $E = 110$ GPa and $\nu = 1/3$, the vibrational

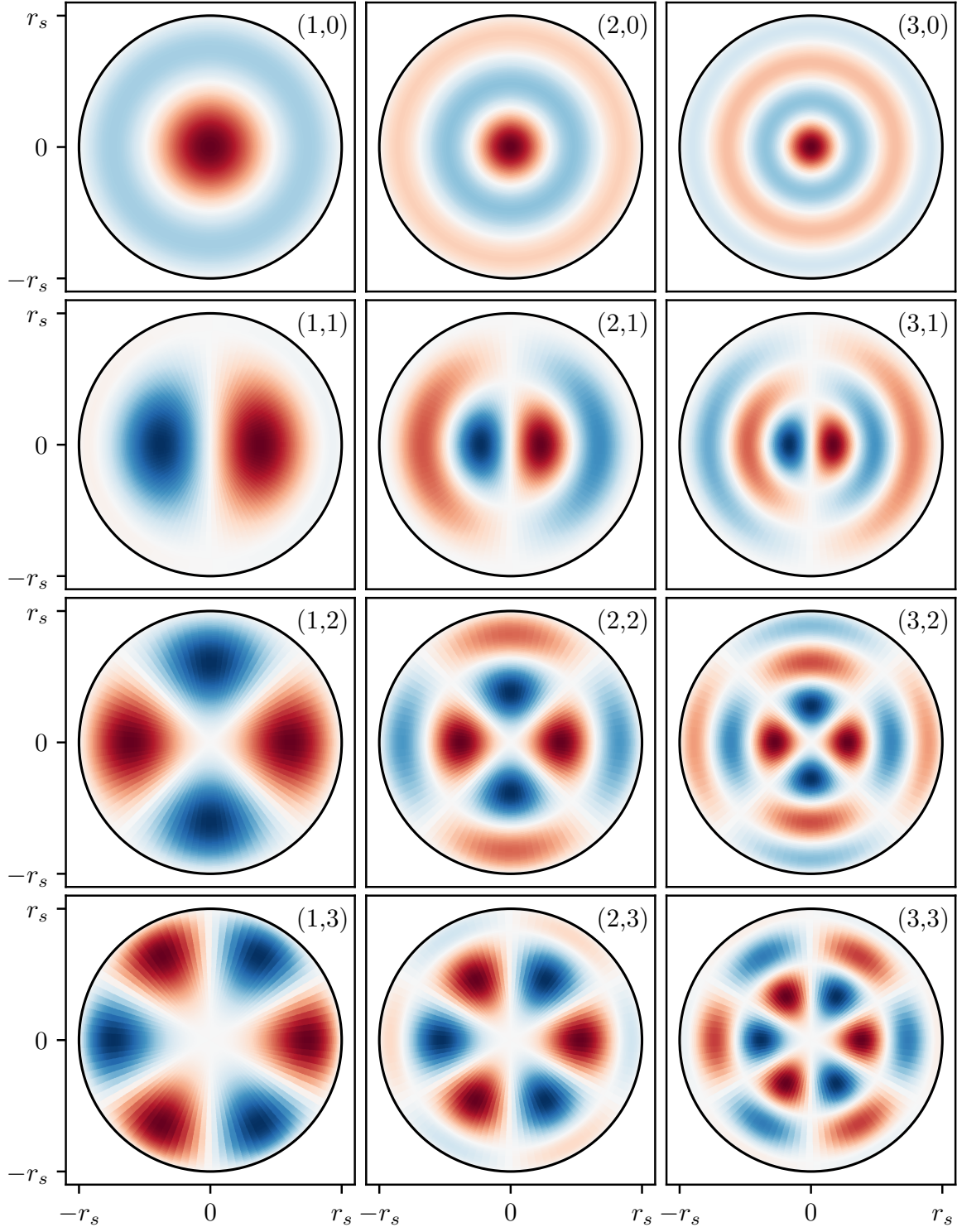


Figure 5.2: Shape u_{kl} of the first 12 modes (k, l) ($k \geq 1$ and $l \geq 0$) of a vibrating spherical plate clamped at its edge after a time $t = (\pi n - \phi_2)/\omega_{kl}$, $n \in \mathbb{Z}$ with $r_s/d = 1000$.

frequencies for the first few modes are between $f_{1,0} = 1.8 \text{ Hz}$ for $(1, 0)$ up to $f_{7,6} = 162 \text{ Hz}$ for $(7, 6)$. These low frequencies result in vibrational energies $\hbar\omega$ that are much smaller than the thermal energy $k_B T$ at any reasonable temperature. Consequently a lot of vibrational modes are highly populated simultaneously as even for temperatures of 10^{-6} K , the first 600 modes are roughly equally populated.

It is possible to determine the asymptotic scaling of ω_{kl} in the limit $k, l \rightarrow \infty$. Using the large-argument-expansion for $x \rightarrow \infty$ of the Bessel functions [74, eq. 10.17.3]

$$J_l(x) \sim \cos\left(x - \frac{l\pi}{2} - \frac{\pi}{4}\right) \quad \text{for } x \rightarrow \infty \quad (5.23)$$

and of the modified Bessel functions [74, eq. 10.40.1]

$$I_l(x) \sim \frac{e^x}{\sqrt{2\pi x}} \quad \text{for } x \rightarrow \infty, \quad (5.24)$$

the asymptotic expansion of eq. (5.20) can be expressed as

$$\sim \frac{e^x}{\sqrt{2\pi x}} \left[\cos\left(x - \frac{l\pi}{2} - \frac{\pi}{4}\right) + \cos\left(x - \frac{l\pi}{2} - \frac{3\pi}{4}\right) \right] = 0. \quad (5.25)$$

Hence, for large $k \rightarrow \infty$, the zeros \tilde{r}_k occur periodically. For large orders $l \rightarrow \infty$, the Bessel functions J_l and I_l scale like [74, eq. 10.19.1 and eq. 10.41.1]

$$J_l(x) \sim I_l(x) \sim \frac{1}{\sqrt{2\pi l}} \left(\frac{ex}{2l}\right)^l \quad \text{for } l \rightarrow \infty, \quad (5.26)$$

implying that the first zero \tilde{r}_1 shift outwards by $\tilde{r}_1 \gtrsim 2l/e$. For high modes k and l this results in an linear asymptotic distribution of zeros and thus, the frequencies ω_{kl} scale in the order of $\mathcal{O}((k+l)^2)$.

Since the amplitude scales inversely with frequency $\Delta z_{kl} \propto 1/\omega_{kl}$, higher modes exhibit a quadratic decrease in amplitude. This effect ensures that higher-order modes have minimal contributions, allowing numerical calculations to focus on the first few modes. Nevertheless, the influence of infinitely many modes can still be approximated asymptotically using the scaling behavior of ω_{kl} .

5.3 Entanglement in front of a thermal shield

The generation of entanglement between two particles depends heavily on variations in their initial placement, as seen in chapter 4. Shield vibrations can effectively be understood to alter the separation and angle of the cat-state relative to shield, as depicted in fig. 5.3. This approximation is only valid for shields significantly larger than the particle radius ($r_s \gg R$) and for low vibrational frequencies ($1/\omega \approx t_{\text{max}}$), effectively capturing the impact of the first vibrational modes for small l and k . Especially the

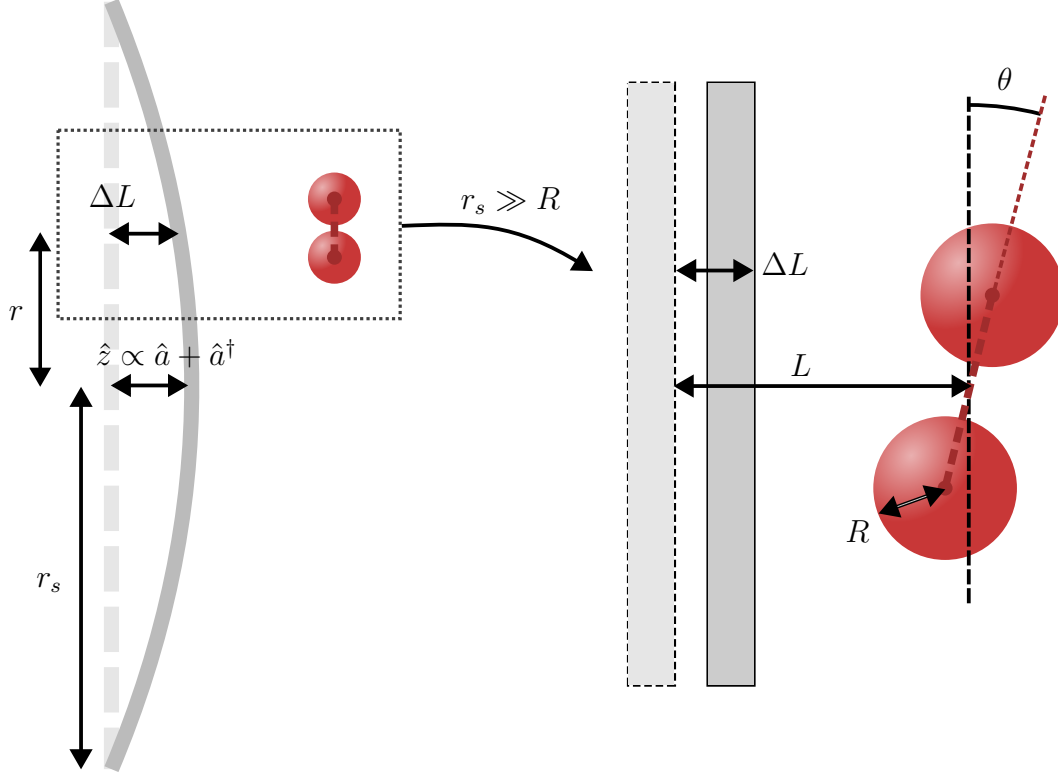


Figure 5.3: For a large ($r_s \gg R$) and locally linearizable shield, thermal vibrations with amplitude z can be interpreted as a static shield where particle A (shown in red) is positioned at $L + \Delta L$ with angle θ and particle B at $L - \Delta L$ with angle $-\theta$. Both variations depend solely on the vibrational amplitude. At low vibrational frequencies ($1/\omega \approx t_{\max}$), the amplitude remains nearly static during an experimental run, with thermal fluctuations distributed around $\langle \hat{z} \rangle = 0$ and variance $\Delta \hat{z}$ given by eq. (5.21). The particles are placed at a distance r away from the shield's center. Especially the cases $r = 0$ and $r \approx 0.527r_s$, where the gradient of the first mode $(1,0)$ is maximized, are considered.

effect of the first mode (1,0) can be put into the same framework from chapter 4. The interpretation is further supported by findings in section 3.3, showing that the Casimir interaction between a sphere and a tilted plane closely resembles that between a sphere and a flat plane. Contrary to the problem considered in chapter 4, here only the thermal amplitude z_{kl} is an independent random variable distributed around $\langle z_{kl} \rangle = 0$ with a standard deviation Δz_{kl} given by eq. (5.21). Variations in the particle-shield separation (ΔL) and angle (θ) are correlated to the vibration amplitude z . For a large and linearizable shield, this can be understood as

$$\theta = \arctan(z |\nabla u|) \approx z |\nabla u| \quad \text{and} \quad \Delta L = z |u| \quad (5.27)$$

where ∇u is the gradient of the vibrational mode's shape. Performing similar calculations to those in chapter 4, the averaged density matrix $\langle \rho \rangle$, dependent on Δz_{kl} , can be derived (see appendix B.3). The resulting entanglement, quantified by logarithmic negativity as a function of temperature T and particle-shield separation L , is given by eq. (B.28) and shown in fig. 5.4. At typical experimental temperatures, entanglement in the presence of

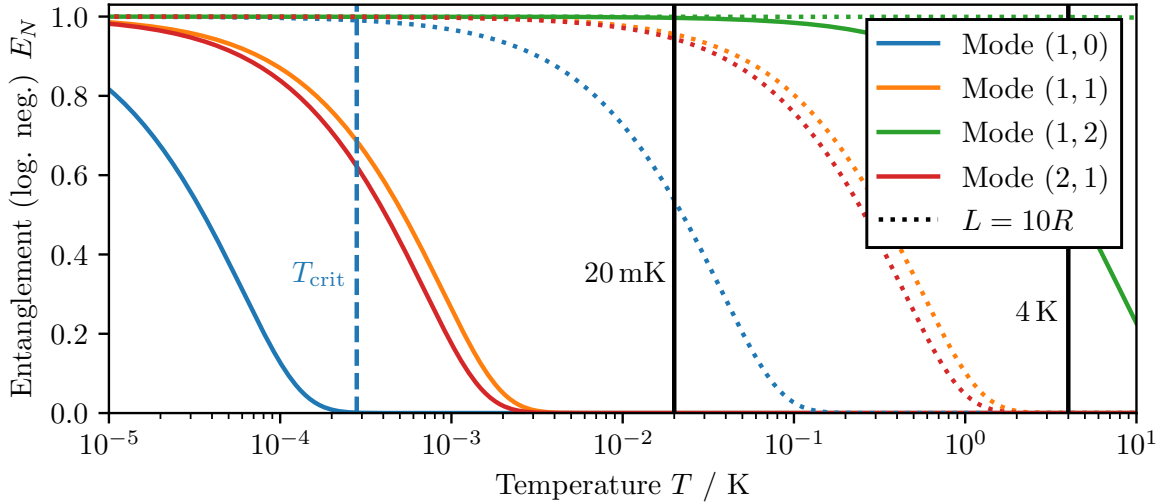


Figure 5.4: Entanglement after a time t_{\max} at different temperatures T . The particle (parameters given in table 4.1) is placed in front of a thermal shield, vibrating in selected modes (k, l), at a position $r \approx 0.527r_s$, where the effect of the first mode (1,0) is maximized. The solid lines show the generated entanglement for $L = 2R = 20 \mu\text{m}$ whereas the dashed lines show the entanglement for $L = 10R$. At a critical temperature $T_{\text{crit}} \propto L^4$, entanglement is lost.

the mode (1,0) is observable only at large particle-shield separations. In fact, the critical temperature T_{crit} scales with the separation L in the large-separation-limit (LSL) as (see eq. (B.29))

$$T_{\text{crit}} = \frac{\tilde{m}\omega_{kl}^2}{k_B} (\Delta z_{\text{crit}})^2 \sim \left(\frac{L^5}{t_{\max}} \right)^2 \sim L^4. \quad (5.28)$$

The large separations required are consistent with previous findings in chapter 4, considering that the thermal amplitudes $\Delta z_{1,0} \approx 9 \times 10^{-11}$ m at 20 mK are comparable with the critical values the variation in the shield-particle separation ΔL_{crit} . Interestingly, these results are unaffected by the shield radius r_s , as long as $r_s \gg R$ and the vibrational mode can be locally linearized. This invariance arises because the gradient $|\nabla u| \sim 1/r_s$ and $\Delta z \propto r_s$ perfectly cancel, leaving θ independent of r_s . When the cat-state orientation is parallel to the shield, the system is very stable against variations in ΔL , leaving the entanglement generation completely independent of r_s in first order.

However, as seen in fig. 5.4, the mode number (k, l) significantly impacts entanglement generation. Higher modes correspond to higher vibrational frequencies and smaller amplitudes Δz , with T_{crit} asymptotically scaling as $\mathcal{O}((k+l)^2)$. This behavior is presented in fig. 5.5. If the particle is positioned exactly at the center of the shield, only spe-

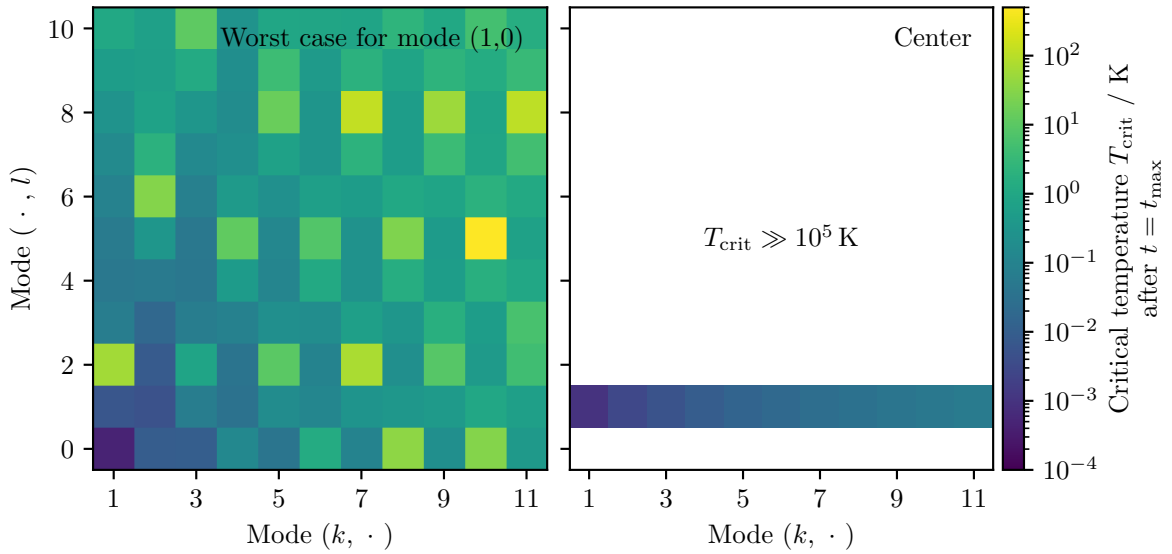


Figure 5.5: Critical temperature T_{crit} , at which no entanglement is measurable anymore for different modes at a separation of $L = 2R = 2 \mu\text{m}$. The shape of the vibrational modes is considered. The particle is either placed at the position of the highest gradient of mode $(1, 0)$ (**left**) or in the center of the shield (**right**).

cific symmetric mode shapes with $l = 2k + 1$, $k \in \mathbb{N}_0$ can induce decoherence. For $l > 1$, this decoherence effects become numerically indistinguishable from 0. If the particle is placed in the worst-case position for the first mode $(1, 0)$, which corresponds to the point of maximum gradient $|\nabla u|$ and thus the largest decoherence (approximately at $r \approx 0.527r_s$), all modes are relevant. It becomes evident, that only the first few vibrational modes significantly affect the entanglement generation. The critical temperature for higher order modes increases and thus the generation of entanglement is not influenced by these vibrations even at reasonable high temperatures.

This naive method for calculating the decoherence induced due to the thermal shield is

only accurate in the specific cases of a large and slow vibrating shield, as it requires the shield to be treaded as flat and tilted on the scale of the particle. Furthermore, due to considering all modes separately, the combined effect is a huge overestimation, as each mode is treaded as maximally displaced simultaneously and no individual dynamics are accounted for. In reality, the displacements of multiple simultaneously occurring modes can cancel each other partially out, reducing the overall decoherence.

5.3.1 Analytic dynamics

The effect of the thermal shield on entanglement generation between the two delocalized particles can be calculated analytically. The Hamiltonian governing the interactions between the two particles with each other and with the thermal shield is given by

$$\begin{aligned}
 \hat{H} = & \sum_{\substack{m \in \{(k,l)\} \\ k \geq 1, l \geq 0}} \left\{ \hbar \omega_m \left(\hat{a}_m^\dagger \hat{a}_m + \frac{1}{2} \right) \right. \\
 & + g_{A,m,Cas}^{(1)} (\hat{a}_m + \hat{a}_m^\dagger) \left(|\psi_A^{(1)}\rangle\langle\psi_A^{(1)}| \otimes \mathbb{1} \right) + g_{A,m,Cas}^{(2)} (\hat{a}_m + \hat{a}_m^\dagger) \left(|\psi_A^{(2)}\rangle\langle\psi_A^{(2)}| \otimes \mathbb{1} \right) \\
 & + g_{B,m,Cas}^{(1)} (\hat{a}_m + \hat{a}_m^\dagger) \left(\mathbb{1} \otimes |\psi_B^{(1)}\rangle\langle\psi_B^{(1)}| \right) + g_{B,m,Cas}^{(2)} (\hat{a}_m + \hat{a}_m^\dagger) \left(\mathbb{1} \otimes |\psi_B^{(2)}\rangle\langle\psi_B^{(2)}| \right) \Big\} \\
 & + g_{Grav}^{(1,1)} |\psi_A^{(1)}\psi_B^{(1)}\rangle\langle\psi_A^{(1)}\psi_B^{(1)}| + g_{Grav}^{(1,2)} |\psi_A^{(1)}\psi_B^{(2)}\rangle\langle\psi_A^{(1)}\psi_B^{(2)}| \\
 & + g_{Grav}^{(2,1)} |\psi_A^{(2)}\psi_B^{(1)}\rangle\langle\psi_A^{(2)}\psi_B^{(1)}| + g_{Grav}^{(2,2)} |\psi_A^{(2)}\psi_B^{(2)}\rangle\langle\psi_A^{(2)}\psi_B^{(2)}|
 \end{aligned} \tag{5.29}$$

where the gravitational coupling

$$g_{Grav}^{(ij)} = \frac{GM^2}{L^{(ij)}} \tag{5.30}$$

between the states $|\psi_A^{(i)}\rangle$ and $|\psi_B^{(j)}\rangle$ ($i, j = 1, 2$) is determined by their separation $L^{(ij)}$ from eq. (4.10). The shield's thermal vibrations have no influence on this coupling, hence the gravitational interaction is the same as already discussed in chapter 4. Gravitational effects arising from the attraction due to the non-zero mass of the shield are omitted in these calculations because they are weaker by a factor of 10^7 compared to the Casimir interactions, as calculated in section 5.1.3.

The Casimir interaction strength $V_{A(B),m,Cas}^{(i)}$ between the state $|\psi_{A(B)}^{(i)}\rangle$ and the shield is described by the term

$$V_{A(B),m,Cas}^{(i)} = \frac{\hbar c \pi^3}{720} \left(\frac{\varepsilon_r - 1}{\varepsilon_r + 1} \right) \varphi(\varepsilon_r) \frac{R}{\left(\mathcal{L} + \hat{z}_m u_m \left(r_{A(B)}^{(i)} \right) \right)^2} \tag{5.31}$$

which is dependent on the mode m and the mode displacement $\hat{z}_m u_m$ at the position $r_{A(B)}^{(i)}$ of the cat-state, where $\hat{z} = \sqrt{\hbar/2\tilde{m}\omega_m}(\hat{a}_m + \hat{a}_m^\dagger)$ is the amplitude of the vibration.

Expanding the term in first order in \hat{z} and ignoring the zeroth-order term, which is constant and thus equal to a global phase at the end of the calculations, the Casimir coupling in the Hamiltonian eq. (5.29) is given by

$$g_{A(B),m,Cas}^{(i)} = g_{PFA} \frac{2u_m(r_{A(B)}^{(i)})}{\mathcal{L}^3} \sqrt{\frac{\hbar}{2\tilde{m}\omega_m}} \quad \text{with} \quad g_{PFA} = \frac{\hbar c \pi^3 R}{720} \left(\frac{\varepsilon_r - 1}{\varepsilon_r + 1} \right) \varphi(\varepsilon_r). \quad (5.32)$$

The combined system of the two particles $\rho_{\text{sys.}} \in \mathcal{H}_{\text{sys.}}$ and the thermal modes $\rho_{\text{th}} = \otimes_m \rho_{\text{th},m} \in \mathcal{H}_{\text{th}}$ evolves under the hamiltonian starting in the initial state $\rho_0 = \rho_{\text{th}} \otimes \rho_{\text{sys.}}$. The initial state of the two particles $\rho_{\text{sys.}}$ is given by eq. (2.2) and $\rho_{\text{th},m}$ is the thermal state of vibrational mode m , which can be represented either in the number basis $\{|n\rangle\}$ or in the coherent state basis $\{|\alpha\rangle\}$ as [75]

$$\rho_{\text{th},m} = \frac{1}{Z} \sum_{n=1}^{\infty} e^{-\beta \hbar \omega_m (n+1/2)} |n\rangle\langle n| = \int d\alpha^2 \frac{1}{\pi \bar{n}} e^{-\frac{|\alpha|^2}{\bar{n}}} |\alpha\rangle\langle \alpha|. \quad (5.33)$$

Here, $Z = \text{tr} e^{-\beta \hbar \omega_m (\hat{n}+1/2)} = e^{-\beta \hbar \omega_m /2} / (1 - e^{-\beta \hbar \omega_m})$ is the partition function and $\bar{n} = 1/(e^{\beta \hbar \omega_m} - 1)$ is the average thermal occupation number of mode m at temperature T .

After time t , tracing out the thermal shield yields the evolved two-particle system

$$\rho_{\text{sys.}}(t) = \text{tr}_{\text{th}} \left(\hat{U}(t) \rho_0 \hat{U}^\dagger(t) \right). \quad (5.34)$$

The time evolution is computed in appendix B.4 and is given by

$$\rho_{\text{system}}(t) = \frac{1}{4} \begin{pmatrix} 1 & e^{i\phi_{11,12}} e^{-\gamma_{11,12}} & e^{i\phi_{11,21}} e^{-\gamma_{11,21}} & e^{i\phi_{11,22}} e^{-\gamma_{11,22}} \\ e^{i\phi_{12,11}} e^{-\gamma_{12,11}} & 1 & e^{i\phi_{12,21}} e^{-\gamma_{12,21}} & e^{i\phi_{12,22}} e^{-\gamma_{12,22}} \\ e^{i\phi_{21,11}} e^{-\gamma_{21,11}} & e^{i\phi_{21,12}} e^{-\gamma_{21,12}} & 1 & e^{i\phi_{21,22}} e^{-\gamma_{21,22}} \\ e^{i\phi_{22,11}} e^{-\gamma_{22,11}} & e^{i\phi_{22,12}} e^{-\gamma_{22,12}} & e^{i\phi_{22,21}} e^{-\gamma_{22,21}} & 1 \end{pmatrix} \quad (5.35)$$

with the decoherence terms

$$\gamma_{ii',jj'} = \sum_m \frac{4}{\hbar^2 \omega_m^2} \left| (g_{A,m,Cas}^{(i)} + g_{B,m,Cas}^{(i')}) - (g_{A,m,Cas}^{(j)} + g_{B,m,Cas}^{(j')}) \right|^2 \sin^2 \left(\frac{\omega_m t}{2} \right) \left[\bar{n} + \frac{1}{2} \right] \quad (5.36)$$

and the phases

$$\begin{aligned} \phi_{ii',jj'} = \sum_m \frac{1}{\hbar} \left(g_{\text{Grav}}^{(ii')} - g_{\text{Grav}}^{(jj')} \right) t \\ + \frac{\sin(\omega_m t) + \omega_m t}{\hbar^2 \omega_m^2} \left[(g_{A,m,Cas}^{(i)} + g_{B,m,Cas}^{(i')})^2 - (g_{A,m,Cas}^{(j)} + g_{B,m,Cas}^{(j')})^2 \right]. \end{aligned} \quad (5.37)$$

At $T = 0$, decoherence terms persist, but their effect is only significant for strong Casimir interactions (e.g., small separations $L \approx R$). The decoherence scales as $\gamma \propto \omega_m^{-4}$ from which the asymptotic dependence on the modes $\mathcal{O}((k+l)^{-8})$ directly follows. It is therefore possible to estimate the combined effect of the first N modes as

$$\sim \frac{1}{\zeta(8)} \sum_{n=1}^N \frac{1}{n^8} \quad (5.38)$$

where ζ is the Riemann zeta function. The sum eq. (5.38) converges very fast to 1, even for small N . At specific times $t = 2\pi k/\omega_m$, $k \in \mathbb{N}$, the decoherence from mode m vanishes, leading to entanglement values close to the ideal case, aligning with the findings in Ref. [76]. This periodic behavior is confirmed in fig. 5.6, showing a measurable amount of entanglement only close to these specific times. The full width

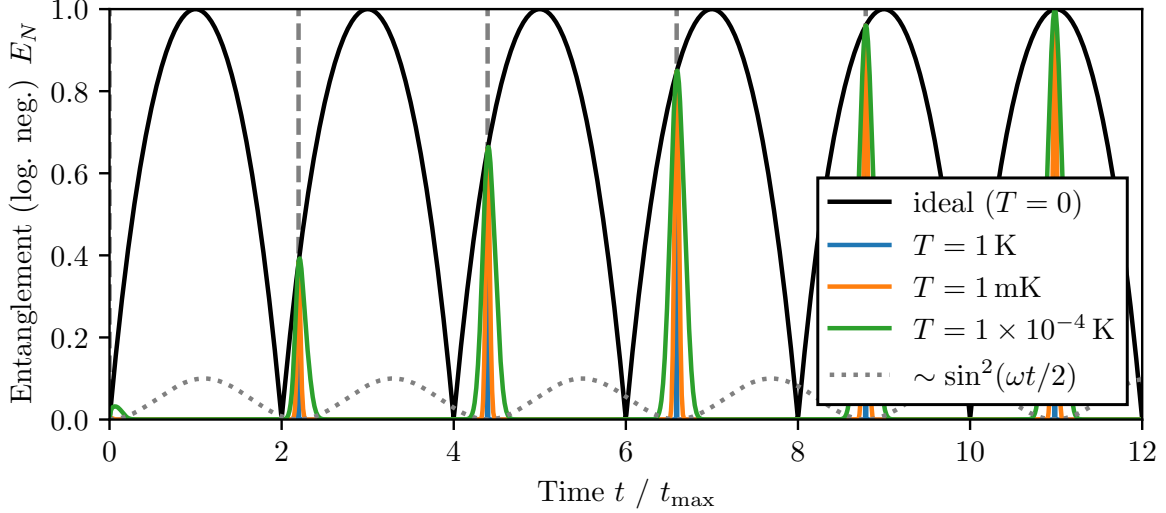


Figure 5.6: Entanglement dynamics in front of a thermal shield in mode (1,0) at different temperatures. Only at specific times $2\pi k/\omega_{1,0} \approx k \times 576$ ms, $k \in \mathbb{N}$, entanglement is observable. This aligns with the findings in Ref. [76]. The particle and shield parameters are taken from table 4.1.

at half maximum (FWHM) of these observed peaks is approximated by

$$\text{FWHM} \approx \frac{4}{\omega} \sqrt{\frac{\log 2}{\gamma}} \propto \frac{1}{\sqrt{n}} \sim \sqrt{\omega/T}, \quad (5.39)$$

getting smaller at higher temperatures.

The resulting decoherence of multiple modes is given by the sum of all individual modes, where the contributed effect decays rapidly with the mode number, as seen in eq. (5.38). Entanglement as seen without the shield is never reachable due to the quasi-periodicity of the system. The frequency ratios $\omega_i/\omega_j \notin \mathbb{Q}$ for $i \neq j$ ¹⁰ prevent exact repetition of the resulting sinusoidal summation. The entanglement dynamics of the first 50 vibrational modes combined are shown in fig. 5.7. This figure highlights the dominant contribution of the first mode (1,0), with realistically measurable entanglement primarily occurring at $t = 2\pi/\omega_{1,0}$. Even for temperatures as low as 20 mK, entanglement remains minimal due to large decoherence. Increasing the particle-shield separation reduces Casimir coupling $g_{\text{Cas}} \propto \mathcal{L}^{-3}$ and hence reducing the decoherence while simultaneously slowing

¹⁰While not rigorously proven, this conclusion is supported by the transcendental nature of the zeros of the Bessel functions [77].

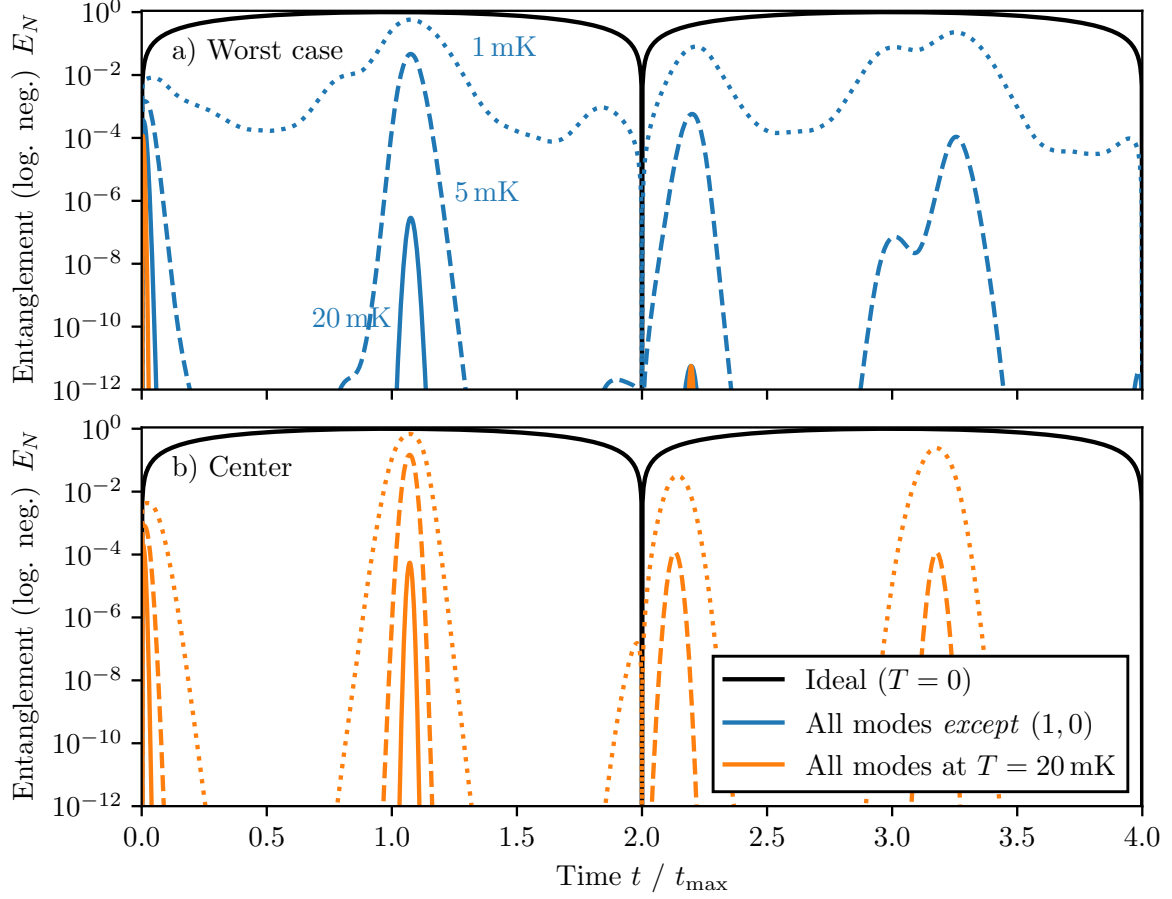


Figure 5.7: Entanglement dynamics in front of a thermal shield. **Orange:** The first 50 modes have been used in the numeric calculation. The effect of all remaining modes is around $1.7 \times 10^{-11} \%$. **Blue:** Results excluding the (1, 0) mode at varying temperatures ranging from 1 mK up to 20 mK. In part **a)** the particles are placed in the worst-case position of the shield where the effect of the mode (1, 0) is maximized. In **b)** the particles are placed in front of the center of the shield. The parameters used are taken from table 4.1.

gravitational entanglement generation down ($t_{\max} \propto L^3$). The combined effect is therefore qualitatively given by $\gamma \propto g_{\text{Cas}}^2 \sin^2(t) \propto L^{-6} \sin^2(L^3) \xrightarrow{L \gg R} 0$, suggesting that no decoherence is present at large separations. The dependence of entanglement on the particle-shield separation at two specific points in time is shown in fig. 5.8.

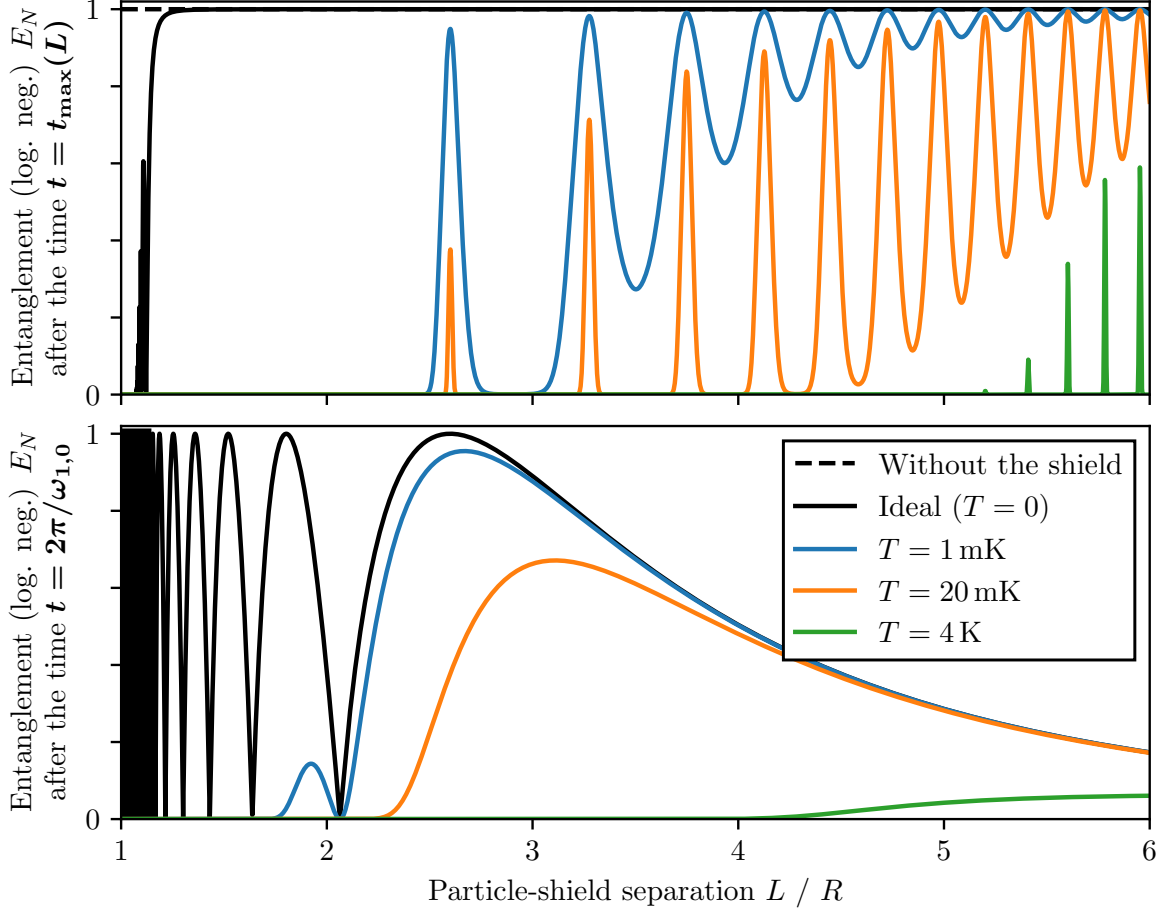


Figure 5.8: Entanglement generation for different particle-shield separations $L > R$ and different temperatures at times $t_{\max}(L)$ (eq. (4.16)) (**top**) and $t = 2\pi/\omega_{1,0} \approx 576$ ms (**bottom**). Calculations use parameters from table 4.1 and the particles are placed in the worst-case position in front of the shield, where the effect of the mode (1,0) is maximized.

By measuring after a time $t_{\max}(L)$ (with $t_{\max}(20 \mu\text{m}) \approx 258$ ms), in the ideal scenario without the shield, a maximally entangled state with $E_N = 1$ is observed. Although $2\pi/\omega_{1,0}$ is constant in time, t_{\max} increases with L , creating specific separations (e.g. for $L \approx 2.6R$) where the two times align, enhancing observability. For even larger L , decoherence effects eq. (5.36) diminish, making entanglement measurable even at higher temperatures.

By measuring at the time $2\pi/\omega_{1,0} \approx 576$ ms where the decoherence of the first mode

almost vanishes, entanglement can be observed by increasing the particle-shield separation. However, measuring at a constant time independent of L limits the maximum of possibly reachable entanglement as the gravitational entanglement rate slows down and increasing t_{\max} .

The radius of the shield also has a large impact on entanglement generation. Smaller shields with larger mode frequencies result in a decreased and faster oscillating decoherence $\gamma \propto \sin^2(\omega)1/\omega_m^2$. The time between the points, where the decoherence effect of the first mode almost vanishes (i.e. every $\Delta t = 2\pi/\omega_{1,0} \propto r_s^2$), decreases for smaller shields and thus making entanglement measurable more frequently at almost any point in time. Numeric calculations show, that even for shields as large as $r_s = 5$ mm, entanglement of around $E_N \lesssim 1$ can be measured at $T = 20$ mK even at close separations (see fig. C.1 and fig. C.2).

Indirect entanglement through the shield

Examining the phases $\phi_{ii',jj'}$ in eq. (5.37) reveals that, similar to the gravitational force, the Casimir interaction between the particle and the shield can induce entanglement between the particles. This occurs as both particles couple to the shield via Casimir interactions, enabling indirect interaction between them. However, the resulting amount of entanglement is very small, as evident from the dependence on $1/\hbar^2$ in eq. (5.37). While negligible at larger separations, Casimir-induced indirect entanglement could become significant at very small distances where the Casimir forces are much stronger than the gravitational interaction. This is particularly relevant if the entanglement generated via Casimir interactions approaches that due to gravity. The relative strength can be estimated by comparing the term corresponding to the gravitational interaction with the Casimir terms in eq. (5.37):

$$g_{\text{Grav}} t \gtrsim \frac{\sin(\omega_m t) + \omega_m t}{\hbar \omega_m^2} g_{\text{Cas}}^2 \quad (5.40)$$

$$\Rightarrow \frac{GM^2}{2L} \gtrsim g_{\text{PFA}} \frac{1}{\mathcal{L}^3} \sqrt{\frac{\hbar}{2\tilde{m}\omega_m}} \quad (5.41)$$

where $\langle \sin(\omega t) \rangle = 0$ was averaged. Using the parameters for the particles and the shield from table 4.1, the lower bound for the separation is given by $L > 1.29 \times 10^{-5} \text{ m} \approx 1.3R$. For separations $L \gtrsim 2.7R$, gravitational entanglement becomes 100 times stronger than entanglement due to Casimir interactions. These separation limits are most likely fulfilled either way considering the results from the previous chapters, thus indirect entanglement can be neglected in all practical circumstances.

5.3.2 Small shields

A small shield can only block the direct Casimir interactions between the particles A and B , hence it can only be used if no other forms of electromagnetic interactions between

the particles such as Coulomb couplings are present. For a very small shield in the size of the particles with radius $r_s \sim R + \Delta x/2$, the above considerations are not fully applicable, as they rely on the linearization of the vibrational mode at the scale of the particles. The vibrations of the shield and the resulting vibrational modes substantially alter the Casimir potential, which is no longer determined solely by the interaction between a perfectly flat shield and a spherical particle. Deformations can therefore not be approximated locally as a flat, tilted plate anymore; instead, the shape of the vibrational mode must be accounted for. As discussed in section 3.3, deformations, such as those resembling the first vibrational mode, significantly impact the resulting Casimir potential which is, in the proximity-force approximation, bounded by an interaction-potential equivalent to that between a sphere and a flat plate with separation $\mathcal{L} \pm \Delta z$.

Vibrational frequencies scale quadratically with the shield size ($\omega \propto 1/r_s^2$), which results in a measuring process multiple times longer than the duration of a single vibrational period. Consequently, Casimir interactions are averaged over time, leading to an effectively planar and flat shield. This agrees with the findings in the previous section and the results shown in fig. C.2, where smaller shields exhibit drastically reduced decoherence effects.

Similar reasoning applies to very higher vibrational modes for arbitrarily large shields: These modes, characterized by high frequencies and a roughly uniform distribution of deformations, effectively result in an averaging in the temporal domain and thus preserving entanglement.

5.4 Discussions of the effects of the thermal shield

In this chapter, two different approaches to quantify the impact of a thermal shield at temperature T on the entanglement generation have been employed, revealing different nuanced insights into the system's dynamic behavior.

The naive approach described in the beginning of section 5.3 assumes a locally static and flat thermal shield, treating vibrational amplitudes z_{kl} as statically and normally distributed over multiple measurements. This method systematically overestimates the dynamics by presuming simultaneous maximal contributions from all vibrational modes. In reality, different modes might cancel themselves partially out, reducing the overall deformation. Critically, this approximation is constrained by two fundamental conditions of requiring a sufficiently large and thus linearizable shield ($r_s \gg R$) as well as low-frequency vibrational mode satisfying $2\pi/\omega_{kl} \approx t_{\max}$.

For the second method, the entanglement generation between the particles was calculated analytically by solving the Hamiltonian dynamics for small amplitudes $\Delta z \ll L$. This approach provides a more accurate description of the time-dependent system and reveals that entanglement can be partially recovered at specific times (notably at $2\pi/\omega_{1,0}$), even for small separations L and large shields.

In general, the effects of the thermal shield can be mitigated by reducing the decoherence effects via the following methods:

Lowering the shield's temperature Reducing the temperature of the shield decreases vibrational amplitudes and the associated decoherence. Temperatures or around 4 K are desirable as they are experimentally accessible using liquid helium cooling. Temperatures as low as 20 mK are theoretically reachable by $^3\text{He}/^4\text{He}$ dilution refrigerators [68, 78]. All cooling mechanisms however induce additional vibrational noise due to their mechanical components and additional studies about the effect of such vibrations has to be considered.

Increasing the particle-shield separation Larger separations reduce the relative effect of the vibrations as $\Delta z/L \rightarrow 0$. In the naive approach, separations of at least $L \gtrsim 10R$ are required, making the shield almost unnecessary as for similar separations, the Casimir interactions between both particles are smaller than the gravitational interaction (see discussion in section 2.3). The presence of the shield could even potentially worsen the entanglement generation. In the more detailed and analytical method in section 5.3.1, separations of around $5R$ are possible, but require measurements at very precise points in time.

Reducing the shield's radius Decreasing r_s does increase the vibrational frequencies quadratically ($\omega_{kl} \propto 1/r_s^2$) and simultaneously decreases the amplitudes $\Delta z_{kl} \sim r_s$. The analytical approach shows a strong dependence on the shield's radius r_s , where halving the radius nearly restores entanglement even for small separations (see fig. C.1 and fig. C.2). The increase in the vibration frequency suggests that in the limit $2\pi/\omega \ll t_{\max}$, vibrations average out over time. A reduction in r_s is however only possible for uncharged, neutral particles that do not interact via a direct Coulomb interaction, necessitating magnetic or optical trapping methods.

By combining these approaches, the thermal shield's impact can be reduced, creating better conditions for entanglement generation. Measurements however might only be possible at specific and precise points in time, particularly at $2\pi/\omega_{1,0}$ with required accuracies of approximately $\Delta t \sim \sqrt{\omega_{1,0}/T}$.

Improvements on the rigidity of the shield can also be considered: Reinforcing the shield, for instance with a cross structure of thicker material, could increase vibrational frequencies and simultaneously decrease amplitudes of the vibrations. Alternative shield designs (e.g. a star shape) might also be beneficial by potentially offering a more uniform vibrational mode distribution and potentially higher frequencies. For rectangular plates in instance, frequency increases are marginal, scaling by $\omega_{kl} = (k^2 + l^2)/(2r_s)^2 \sqrt{D\pi^4/\rho d}$ [73, p. 471-474] and thus improving entanglement generation only at most up to a constant.

6 Discussion and outlook

Testing the quantum nature of gravity is notoriously difficult due to its inherent weakness relative to the other fundamental forces. The concept of gravitationally induced entanglement as evidence for the non-classicality of gravity was first proposed by Feynman at the 1957 Chapel Hill Conference. Since then, several experimental proposals have emerged [15–17], all focusing on measuring entanglement between macroscopic delocalized masses via a direct gravitational coupling. A common approach to prevent electromagnetic interactions such as short-range Casimir forces, involves placing a conductive Faraday shield between the particles [43].

In this thesis, it was shown by calculating the relative dynamical phase build-up, that Casimir interactions between two macroscopic Schrödinger-cat states and a conducting Faraday shield can destroy all measurable entanglement, if small stochastic variations in the initial setup or thermal vibrations of the shield are present. Placement accuracies in the initialization of the cat-states should stay below a threshold, depending on the achievable magnitudes in superposition size and particle masses, usually well below $\Delta\theta \lesssim 10^{-8}$ rad and $\Delta L \lesssim 10^{-9}$ m. To mitigate the decoherence effects of the thermal shield, measuring at very precise points in time is required, where particularly the effects of the first vibrational mode are minimized. The calculated bounds for the placement parameters and the measurement accuracy appear to be very difficult up to practically impossible to implement experimentally in the near future.

Enhancements in entanglement generation are achievable by either increasing the mass or superposition size of the particles or by optimizing the particle-shield separation. While a Faraday shield enables closer particle placements by mitigating inter-particle Casimir forces, its effectiveness is conditional as some parameter regimes favor setups without the shield. A strategy for optimal parameter selection, tailored to experimental constraints on state preparation and placement accuracy was presented in section 4.4. By choosing the shield as small as possible and temperatures as low as physically reachable, decoherence effects of the thermal shield weakens, improving entanglement generation. Uncharged particles, requiring a much smaller shield, emerged as particularly favorable.

Future theoretical studies could benefit from incorporating squeezed gaussian states [79, p. 33-64] or alternative delocalized states in the analysis. Most realizations of spatial superpositions of massive objects, especially in the world of high mass levitated particles, are going to be ideally imperfect squeezed gaussian states [41, Timestamp: 23:00] as they can be naturally prepared by ground state cooling in a harmonic trap [80]. However, the findings in Ref. [27] suggest that the results derived for Schrödinger-cat states in the center-of-mass position should remain largely applicable.

Other forms of decoherence, such as undamped vibrations of the setup (potentially due to complex cooling mechanisms) and black-body radiation between the particles can also be considered. It is possible to estimate the decoherence due to thermal radiation [81, p. 127-136] between the cat states at temperature T by [82]

$$\Gamma_{\text{decoh., black-body}} = \Gamma_0 \left[1 - \exp \left\{ -\frac{(\Delta x)^2}{\lambda_{\text{th}}^2} \right\} \right] \sim (\Delta x)^2 \quad (6.1)$$

where $\lambda_{\text{th}} = \pi^{2/3} \hbar c / k_B T$ is the thermal wavelength with values of $\lambda_{\text{th}} \approx 1 \text{ mm}$ at 4 K and (for $\Im(\varepsilon_r) \approx 0$, since silica is transparent)

$$\Gamma_0 = \frac{8! \cdot 8\zeta(9) R^6 c}{9\pi} \left(\frac{k_B T}{\hbar c} \right)^7 \left(\frac{\varepsilon_r - 1}{\varepsilon_r + 1} \right)^2 \approx 1.7 \times 10^5 \text{ s}^{-1}. \quad (6.2)$$

It follows that $\Gamma_{\text{decoh., black-body}} \ll \Gamma_{\text{Gravity}}$ in the parameter regime given by table 4.1. For very large superposition sizes, decoherence stays constant ($\Gamma_{\text{decoh.}} \sim \Gamma_0$) resulting in a domination of gravitational entanglement generation. Other forms of decoherence, like collisions with air molecules, can similarly be accounted for and thus a required vacuum pressure can be estimated.

Analogous to variations in the initial particle placement for each run, variations in other parameters, such as the measurement time (i.e. the time of gravitational interaction between the states), can be examined. A brief investigation of this effect was presented in Ref. [58], showing results consistent with those obtained in this thesis. The varying gravitational effects of non-stationary surrounding masses must also be considered, as they can influence the entanglement generation differently during each measurement run. For instance, the gravitational attraction exerted by the moon on the masses is 10^7 times stronger than their mutual gravitational interaction. Variations in the moon-earth distance over a lunar period can alter this attraction over multiple runs and result in additional effective decoherence. Even changes in atmospheric conditions might need to be accounted for as different densities due to temperature fluctuations would exert different gravitational attractions.

Advanced data analysis methodologies present further promising avenues for reducing the effective decoherences due to stochastic particle placements. By measuring initial placement parameters each run or establishing skewed probabilistic distribution models, decoherence effects might be partially accounted for. The calculations in this thesis are therefore potentially just an overestimation.

Given the existence of geometries that exhibit either attractive or repulsive Casimir forces [50], it is reasonable to hypothesize the existence of shapes with significantly reduced or even negligible Casimir interaction. Such bodies would offer clear advantages, including reduced unwanted entanglement generation between the particles, potentially eliminating the necessity of the Faraday shield. However, identifying such geometries and reliably fabricating nanoparticles in them at the micrometer scale is by no means trivial.

The findings in this thesis have broader implications beyond gravitationally induced entanglement, as a new method for the precise measurement of Casimir forces can be developed utilizing spatial delocalizations. The idea of using levitated particles for observing Casimir interactions is a current research topic [83]. By positioning a single Schrödinger-cat superposition state close to a large thermally vibrating plate, dephasing effects similar to the ones discussed in section 5.3.1 are expected due to the slightly different interactions of each superposition component with the plate. Measuring this dephasing offers a way to determine the Casimir coupling strength between arbitrarily shaped objects and a flat plane with high precision. Moreover, this approach could be extended to measure Casimir-Polder interactions between atoms or molecules and a plate. Current technologies, as demonstrated in matter-wave experiments [31], could be sufficient even today. Experimental setups designated for gravitational entanglement sensing can be adapted for these measurements, providing a new and precise tool for testing modern theories of Casimir interactions.

In essence, this thesis offers an overview and an estimation of previously overlooked experimental issues with proposed experiments on quantum gravity. By addressing these problems, this work partially paves the way for the possible experimental realization of measuring gravitationally induced entanglement, which ultimately advances the quest for a grand unifying theory of quantum gravity.

Bibliography

- [1] I. Newton, *Philosophiæ Naturalis Principia Mathematica* (England, 1687).
- [2] N. Maskelyne, “A proposal for measuring the attraction of some hill in this kingdom by astronomical observations”, *Philosophical Transactions of the Royal Society of London* **65**, 495–499 (1775) 10.1098/rstl.1775.0049.
- [3] R. D. Davies, “A Commemoration of Maskelyne at Schiehallion”, *Quarterly Journal of the Royal Astronomical Society* **26**, 289–294 (1985).
- [4] H. Cavendish, “Experiments to determine the density of the earth”, *Philosophical Transactions of the Royal Society of London* **88**, 469–526 (1798) 10.1098/rstl.1798.0022.
- [5] A. Einstein, “Die Grundlage der allgemeinen Relativitätstheorie”, *Annalen der Physik* **354**, 769–822 (1916) 10.1002/andp.19163540702.
- [6] K. Becker, *String theory and M-theory, A modern introduction*, edited by M. Becker and J. H. Schwarz, Includes bibliographical references and index. (Cambridge University Press, Cambridge, 2007), 739 pages.
- [7] A. Ashtekar, “New Variables for Classical and Quantum Gravity”, *Physical Review Letters* **57**, 2244–2247 (1986) 10.1103/physrevlett.57.2244.
- [8] J. Oppenheim, “A Postquantum Theory of Classical Gravity?”, *Physical Review X* **13**, 041040 (2023) 10.1103/physrevx.13.041040, arXiv:1811.03116 [hep-th].
- [9] D. Rickles and C. M. DeWitt, *The Role of Gravitation in Physics: Report from the 1957 Chapel Hill Conference*, en (Max-Planck-Gesellschaft zur Förderung der Wissenschaften, Berlin, Feb. 2011), 10.34663/9783945561294-00.
- [10] H. D. Zeh, “Feynman’s interpretation of quantum theory”, *The European Physical Journal H* **36**, 63–74 (2008) 10.1140/epjh/e2011-10035-2, arXiv:0804.3348.
- [11] N. H. Lindner and A. Peres, “Testing quantum superpositions of the gravitational field with Bose-Einstein condensates”, *Physical Review A* **71**, 024101 (2005) 10.1103/physreva.71.024101.
- [12] D. Kafri and J. M. Taylor, “A noise inequality for classical forces”, 10.48550/ARXIV.1311.4558 (2013) 10.48550/ARXIV.1311.4558, arXiv:1311.4558.
- [13] J. Schmöle, M. Dragosits, H. Hepach, and M. Aspelmeyer, “A micromechanical proof-of-principle experiment for measuring the gravitational force of milligram masses”, *Classical and Quantum Gravity* **33**, 125031 (2016) 10.1088/0264-9381/33/12/125031, arXiv:1602.07539 [physics.ins-det].

- [14] T. Krisnanda, M. Zuppardo, M. Paternostro, and T. Paterek, “Revealing Non-classicality of Inaccessible Objects”, *Physical Review Letters* **119**, 120402 (2016) 10.1103/physrevlett.119.120402, arXiv:1607.01140.
- [15] S. Bose, A. Mazumdar, G. W. Morley, H. Ulbricht, M. Toroš, M. Paternostro, A. Geraci, P. Barker, M. S. Kim, and G. Milburn, “A Spin Entanglement Witness for Quantum Gravity”, *Phys. Rev. Lett.* **119**, 240401 (2017) 10.1103/physrevlett.119.240401, arXiv:1707.06050.
- [16] C. Marletto and V. Vedral, “Gravitationally Induced Entanglement between Two Massive Particles is Sufficient Evidence of Quantum Effects in Gravity”, *Physical Review Letters* **119**, 240402 (2017) 10.1103/physrevlett.119.240402, arXiv:1707.06036.
- [17] T. Krisnanda, G. Y. Tham, M. Paternostro, and T. Paterek, “Observable quantum entanglement due to gravity”, *npj Quantum Information* **6**, 10.1038/s41534-020-0243-y (2019) 10.1038/s41534-020-0243-y, arXiv:1906.08808.
- [18] H. B. G. Casimir, “On the attraction between two perfectly conducting plates”, *Proc. Kon. Ned. Akad. Wet.* **51**, 793 (1948).
- [19] H. Chevalier, A. J. Paige, and M. S. Kim, “Witnessing the nonclassical nature of gravity in the presence of unknown interactions”, *Physical Review A* **102**, 022428 (2020) 10.1103/physreva.102.022428, arXiv:2005.13922.
- [20] J. S. Pedernales, G. W. Morley, and M. B. Plenio, “Motional Dynamical Decoupling for Matter-Wave Interferometry”, *Phy. Rev. Lett.* **125**, 023602 (2019) 10.1103/physrevlett.125.023602, arXiv:1906.00835.
- [21] C. Overstreet, P. Asenbaum, J. Curti, M. Kim, and M. A. Kasevich, “Observation of a gravitational Aharonov-Bohm effect”, *Science* **375**, 226–229 (2022) 10.1126/science.abl7152.
- [22] R. Colella, A. W. Overhauser, and S. A. Werner, “Observation of Gravitationally Induced Quantum Interference”, *Physical Review Letters* **34**, 1472–1474 (1975) 10.1103/physrevlett.34.1472.
- [23] L. Lami, J. S. Pedernales, and M. B. Plenio, “Testing the quantum nature of gravity without entanglement”, *Phys. Rev. X* **14**, 021022 (2023) 10.1103/physrevx.14.021022, arXiv:2302.03075.
- [24] R. Horodecki, P. Horodecki, M. Horodecki, and K. Horodecki, “Quantum entanglement”, *Rev. Mod. Phys.* **81**, 865–942 (2007) 10.1103/revmodphys.81.865, arXiv:quant-ph/0702225.
- [25] M. B. Plenio and S. Virmani, “An introduction to entanglement measures”, *Quantum Information & Computation* **7**, 1–51 (2005), arXiv:quant-ph/0504163.
- [26] M. J. W. Hall and M. Reginatto, “On two recent proposals for witnessing non-classical gravity”, *Journal of Physics A: Mathematical and Theoretical* **51**, 085303 (2017) 10.1088/1751-8121/aaa734, arXiv:1707.07974.

- [27] J. S. Pedernales and M. B. Plenio, “On the origin of force sensitivity in tests of quantum gravity with delocalised mechanical systems”, *Contemporary Physics* **64**, 147–163 (2023) 10.1080/00107514.2023.2286074, arXiv:2311.04745.
- [28] M. Reginatto and M. J. W. Hall, “Entangling quantum fields via a classical gravitational interaction”, *Journal of Physics: Conference Series* **1275**, 012039 (2019) 10.1088/1742-6596/1275/1/012039, arXiv:1809.04989 [gr-qc].
- [29] D. Carney, P. C. E. Stamp, and J. M. Taylor, “Tabletop experiments for quantum gravity: a user’s manual”, *Classical and Quantum Gravity* **36**, 034001 (2018) 10.1088/1361-6382/aaf9ca, arXiv:1807.11494.
- [30] M. Christodoulou, A. Di Biagio, M. Aspelmeyer, Č. Brukner, C. Rovelli, and R. Howl, “Locally mediated entanglement in linearised quantum gravity”, *Physical Review Letters* **130**, 100202 (2022) 10.1103/physrevlett.130.100202, arXiv:2202.03368.
- [31] Y. Y. Fein, P. Geyer, P. Zwick, F. Kiałka, S. Pedalino, M. Mayor, S. Gerlich, and M. Arndt, “Quantum superposition of molecules beyond 25 kDa”, *Nature Physics* **15**, 1242–1245 (2019) 10.1038/s41567-019-0663-9.
- [32] T. Westphal, H. Hepach, J. Pfaff, and M. Aspelmeyer, “Measurement of Gravitational Coupling between Millimeter-Sized Masses”, *Nature* **591**, 225–228 (2021) 10.1038/s41586-021-03250-7, arXiv:2009.09546.
- [33] H. B. G. Casimir and D. Polder, “The Influence of Retardation on the London-van der Waals Forces”, *Physical Review* **73**, 360–372 (1948) 10.1103/physrev.73.360.
- [34] L. Gurvits, “Classical deterministic complexity of Edmonds’ problem and Quantum Entanglement”, in *Proceedings of the thirty-fifth annual acm symposium on theory of computing*, Vol. 4, STOC03 (June 2003), pages 10–19, 10.1145/780542.780545, arXiv:quant-ph/0303055.
- [35] G. Vidal and R. F. Werner, “A computable measure of entanglement”, *Phys. Rev. A* **65**, 032314 (2001) 10.1103/physreva.65.032314, arXiv:quant-ph/0102117.
- [36] M. Plenio, “Logarithmic negativity: a full entanglement monotone that is not convex.”, *Physical Review Letters* **95**, 090503 (2005) 10.1103/PhysRevLett.95.090503, arXiv:quant-ph/0505071.
- [37] A. D. O’Connell, M. Hofheinz, M. Ansmann, R. C. Bialczak, M. Lenander, E. Lucero, M. Neeley, D. Sank, H. Wang, M. Weides, J. Wenner, J. M. Martinis, and A. N. Cleland, “Quantum ground state and single-phonon control of a mechanical resonator”, *Nature* **464**, 697–703 (2010) 10.1038/nature08967.
- [38] R. L. DeBiase, “Are Casimir Forces Conservative?”, *Physics Procedia* **38**, 18–33 (2012) 10.1016/j.phpro.2012.08.008.

- [39] B. Yi, U. Sinha, D. Home, A. Mazumdar, and S. Bose, “Massive spatial qubits: Testing macroscopic nonclassicality and Casimir entanglement”, *Physical Review Research* **5**, 033202 (2023) 10.1103/physrevresearch.5.033202, arXiv:2106.11906.
- [40] T. Emig, N. Graham, R. L. Jaffe, and M. Kardar, “Casimir forces between arbitrary compact objects”, *Phys. Rev. Lett.* **99**, 170403 (2007) 10.1103/physrevlett.99.170403, arXiv:0707.1862.
- [41] M. Aspelmeyer, *Quantum sources of gravity: the next frontier of macroscopic quantum physics*, <https://www.youtube.com/watch?v=0AVDrVY-rTw>, May 2024.
- [42] C. Gonzalez-Ballester, M. Aspelmeyer, L. Novotny, R. Quidant, and O. Romero-Isart, “Levitodynamics: levitation and control of microscopic objects in vacuum”, *Science* **374**, 10.1126/science.abg3027 (2021) 10.1126/science.abg3027, arXiv:2111.05215.
- [43] T. W. van de Kamp, R. J. Marshman, S. Bose, and A. Mazumdar, “Quantum Gravity Witness via Entanglement of Masses: Casimir Screening”, *Phys. Rev. A* **102**, 062807 (2020) 10.1103/physreva.102.062807, arXiv:2006.06931.
- [44] H. Rudolph, U. DeliĆ, M. Aspelmeyer, K. Hornberger, and B. A. Stickler, “Force-Gradient Sensing and Entanglement via Feedback Cooling of Interacting Nanoparticles”, *Physical Review Letters* **129**, 193602 (2022) 10.1103/physrevlett.129.193602, arXiv:2204.13684 [quant-ph].
- [45] F. London, “Zur Theorie und Systematik der Molekularkräfte”, *Zeitschrift für Physik* **63**, 245–279 (1930) 10.1007/bf01421741.
- [46] M. Bordag, U. Mohideen, and V. M. Mostepanenko, “New developments in the Casimir effect”, *Physics Reports* **353**, 1–205 (2001) 10.1016/s0370-1573(01)00015-1, arXiv:quant-ph/0106045 [quant-ph].
- [47] G. L. Klimchitskaya, U. Mohideen, and V. M. Mostepanenko, “The Casimir force between real materials: Experiment and theory”, *Reviews of Modern Physics* **81**, 1827–1885 (2009) 10.1103/revmodphys.81.1827, arXiv:0902.4022.
- [48] S. K. Lamoreaux, “The Casimir force: background, experiments, and applications”, *Reports on Progress in Physics* **68**, 201–236 (2004) 10.1088/0034-4885/68/1/r04.
- [49] M. Bordag, “Proceedings of the Fourth Workshop on Quantum Field Theory under the Influence of External Conditions”, in *The Casimir Effect 50 Years Later* (June 1999), pages 1–410, 10.1142/9789814527576.
- [50] T. H. Boyer, “Quantum Electromagnetic Zero-Point Energy of a Conducting Spherical Shell and the Casimir Model for a Charged Particle”, *Physical Review* **174**, 1764–1776 (1968) 10.1103/physrev.174.1764.

- [51] L. H. Ford, “Casimir Force between a Dielectric Sphere and a Wall: A Model for Amplification of Vacuum Fluctuations”, *Phys. Rev. A* **58**, 4279–4286 (1998) 10.1103/physreva.58.4279, arXiv:quant-ph/9804055.
- [52] E. M. Lifshitz, “The theory of molecular attractive forces between solids”, *Sov. Phys. JETP* **2**, 73–83 (1956) 10.1016/b978-0-08-036364-6.50031-4.
- [53] M. Hartmann, “Casimir effect in the plane-spheregeometry: Beyond the proximityforce approximation”, PhD thesis (Universität Augsburg, July 2018).
- [54] T. Emig, “Fluctuation induced quantum interactions between compact objects and a plane mirror”, *Journal of Statistical Mechanics: Theory and Experiment* **2008**, P04007 (2007) 10.1088/1742-5468/2008/04/p04007, arXiv:0712.2199.
- [55] A. Bulgac, P. Magierski, and A. Wirzba, “Scalar Casimir effect between Dirichlet spheres or a plate and a sphere”, *Physical Review D* **73**, 025007 (2006) 10.1103/physrevd.73.025007.
- [56] I. G. Pirozhenko and M. Bordag, “On the Casimir repulsion in sphere-plate geometry”, *Physical Review D* **87**, 085031 (2013) 10.1103/physrevd.87.085031, arXiv:1302.5290.
- [57] K. Perlin, “An image synthesizer”, *SIGGRAPH Comput. Graph.* **19**, 287–296 (1985) 10.1145/325165.325247.
- [58] H. C. Nguyen and F. Bernards, “Entanglement dynamics of two mesoscopic objects with gravitational interaction”, *The European Physical Journal D* **74**, 10.1140/epjd/e2020-10077-8 (2020) 10.1140/epjd/e2020-10077-8, arXiv:1906.11184.
- [59] K. F. Riley, *Mathematical methods for physics and engineering*, edited by M. P. Hobson and S. J. Bence, Third edition, Hier auch später erschienene, unveränderte Nachdrucke (Cambridge University Press, Cambridge, 2018), 1333 pages.
- [60] A. C. Berry, “The accuracy of the Gaussian approximation to the sum of independent variates”, *Transactions of the American Mathematical Society* **49**, 122–136 (1941) 10.1090/s0002-9947-1941-0003498-3.
- [61] S. Rijavec, M. Carlesso, A. Bassi, V. Vedral, and C. Marletto, “Decoherence effects in non-classicality tests of gravity”, *New Journal of Physics* **23**, 043040 (2020) 10.1088/1367-2630/abf3eb, arXiv:2012.06230.
- [62] K. C. Lee, M. R. Sprague, B. J. Sussman, J. Nunn, N. K. Langford, X.-M. Jin, T. Champion, P. Michelberger, K. F. Reim, D. England, D. Jaksch, and I. A. Walmsley, “Entangling Macroscopic Diamonds at Room Temperature”, *Science* **334**, 1253–1256 (2011) 10.1126/science.1211914.
- [63] M. Bild, M. Fadel, Y. Yang, U. von Lüpke, P. Martin, A. Bruno, and Y. Chu, “Schrödinger cat states of a 16-microgram mechanical oscillator”, *Science* **380**, 274–278 (2022) 10.1126/science.adf7553, arXiv:2211.00449.
- [64] C. Whittle, E. D. Hall, S. Dwyer, and et al., “Approaching the motional ground state of a 10-kg object”, *Science* **372**, 1333–1336 (2021) 10.1126/science.abh2634, arXiv:2102.12665.

- [65] D. Grass, J. Fesel, S. G. Hofer, N. Kiesel, and M. Aspelmeyer, “Optical trapping and control of nanoparticles inside evacuated hollow core photonic crystal fibers”, *Applied Physics Letters* **108**, 10.1063/1.4953025 (2016) 10.1063/1.4953025, arXiv:1603.09393.
- [66] B. R. Slezak, C. W. Lewandowski, J.-F. Hsu, and B. D’Urso, “Cooling the motion of a silica microsphere in a magneto-gravitational trap in ultra-high vacuum”, *New Journal of Physics* **20**, 063028 (2018) 10.1088/1367-2630/aacac1, arXiv:1802.03424 [quant-ph].
- [67] W. P. Schleich, “Waves à la WKB”, in *Quantum Optics in Phase Space* (John Wiley & Sons, Ltd, Berlin, Feb. 2001) Chap. 5, pages 153–169.
- [68] H. Zu, W. Dai, and A. T. A. M. de Waele, “Development of dilution refrigerators - A review”, *Cryogenics* **121**, 103390 (2022) 10.1016/j.cryogenics.2021.103390.
- [69] G. A. E. Vandenbosch, “The basic concepts determining electromagnetic shielding”, *American Journal of Physics* **90**, 672–681 (2022) 10.1119/5.0087295.
- [70] R. Gross and A. Marx, *Festkörperphysik*, 3., akt. Aufl, De Gruyter Studium (De Gruyter, Berlin, 2018), 11066 pages.
- [71] R. Berman, D. K. C. Macdonald, and F. E. Simon, “The thermal and electrical conductivity of copper at low temperatures”, *Proceedings of the Royal Society of London. Series A. Mathematical and Physical Sciences* **211**, 122–128 (1952) 10.1098/rspa.1952.0029.
- [72] J. Dutka, “On the Early History of Bessel Functions”, *Archive for History of Exact Sciences* **49**, 105–134 (1995).
- [73] S. S. Rao, *Vibration of Continuous Systems*, 2nd Edition (Wiley, Jan. 2019), 10.1002/9781119424284.
- [74] F. W. J. Olver, A. B. Olde Daalhuis, D. W. Lozier, B. I. Schneider, R. F. Boisvert, C. W. Clark, B. R. Miller, B. V. Saunders, H. S. Cohl, M. A. McClain, and eds., *NIST Digital Library of Mathematical Functions*, <https://dlmf.nist.gov/>, Release 1.2.2 of 2024-09-15, 2024.
- [75] M. O. E. Steiner, J. S. Pedernales, and M. B. Plenio, “Pentacene-Doped Naphthalene for Levitated Optomechanics”, 10.48550/ARXIV.2405.13869 (2024) 10.48550/ARXIV.2405.13869, arXiv:2405.13869 [quant-ph].
- [76] J. S. Pedernales, K. Streltsov, and M. B. Plenio, “Enhancing Gravitational Interaction between Quantum Systems by a Massive Mediator”, *Physical Review Letters* **128**, 110401 (2021) 10.1103/physrevlett.128.110401, arXiv:2104.14524.
- [77] L. Lorch and M. E. Muldoon, “Transcendentality of zeros of higher derivatives of functions involving Bessel functions”, *International Journal of Mathematics and Mathematical Sciences* **18**, 551–560 (1995) 10.1155/s0161171295000706.
- [78] P. Das, R. B. de Ouboter, and K. W. Taconis, “A Realization of a London-Clarke-Mendoza Type Refrigerator”, in Ninth international conference on low-temperature physics (1965), pages 1253–1255, 10.1007/978-1-4899-6443-4_133.

- [79] A. Serafini, *Quantum Continuous Variables: A Primer of Theoretical Methods*, 1st ed. (CRC Press, July 2017), 10.1201/9781315118727.
- [80] T. Weiss, M. Roda-Llodes, E. Torrontegui, M. Aspelmeyer, and O. Romero-Isart, “Large Quantum Delocalization of a Levitated Nanoparticle Using Optimal Control: Applications for Force Sensing and Entangling via Weak Forces”, *Physical Review Letters* **127**, 023601 (2020) 10.1103/physrevlett.127.023601, arXiv:2012.12260.
- [81] M. Schlosshauer, *Decoherence and the Quantum-To-Classical Transition*, 1st edition (Springer, Berlin, Heidelberg, July 2007), 10.1007/978-3-540-35775-9.
- [82] O. Romero-Isart, “Quantum superposition of massive objects and collapse models”, *Physical Review A* **84**, 052121 (2011) 10.1103/physreva.84.052121, arXiv:1110.4495.
- [83] Z. Xu, P. Ju, K. Shen, Y. Jin, Z. Jacob, and T. Li, “Observation of non-contact Casimir friction”, 10.48550/ARXIV.2403.06051 (2024) 10.48550/ARXIV.2403.06051, arXiv:2403.06051.
- [84] D. J. Griffiths, *Elektrodynamik, Eine Einführung*, edited by U. Schollwöck, 4th edition (Pearson, Hallbergmoos, 2018), 1711 pages.
- [85] S. Blanes, F. Casas, J. A. Oteo, and J. Ros, “The Magnus expansion and some of its applications”, *Physics Reports* **470**, 151–238 (2008) 10.1016/j.physrep.2008.11.001, arXiv:0810.5488 [math-ph].

A Ancillary calculations

A.1 Evolution under a gravitational Hamiltonian

In this section the time evolution of a system under Hamiltonian eq. (2.1) is calculated for two particles A and B (mass m) separated by L in a harmonic trap (frequency ω). A example from Ref. [29] is followed. The total Hamiltonian describing the dynamics is given by

$$\hat{H} = \sum_{i=A,B} \frac{\hat{p}_i^2}{2m} + \frac{1}{2}m\omega^2 \hat{x}_i^2 + \hat{H}_G \quad (\text{A.1})$$

where \hat{x} and \hat{p} are the position and momentum operators of the particle satisfying the canonical commutator relation $[\hat{x}_i, \hat{p}_j] = i\hbar\delta_{ij}$. Introducing ladder operators $\hat{x}_i = \sqrt{\hbar/2m\omega}(\hat{a}_i^\dagger + \hat{a}_i)$, $\hat{p}_i = \sqrt{\hbar m\omega/2}(\hat{a}_i^\dagger - \hat{a}_i)$, the Hamiltonian can be rewritten:

$$\hat{H} = \sum_{i=A,B} \hbar\omega \hat{a}_i^\dagger \hat{a}_i - \frac{Gm^2}{L^3} \left(\sqrt{\frac{\hbar}{2m\omega}} \right)^2 (\hat{a}_A \hat{a}_B + \hat{a}_A \hat{a}_B^\dagger + \hat{a}_A^\dagger \hat{a}_B + \hat{a}_A^\dagger \hat{a}_B^\dagger). \quad (\text{A.2})$$

Applying the rotating wave approximation, the term $\hat{a}_A \hat{a}_B + \hat{a}_A^\dagger \hat{a}_B^\dagger$ can be dropped. The effective Hamiltonian is therefore in the form

$$\hat{H}_{\text{eff}} = \sum_{i=A,B} \hbar\omega \hat{a}_i^\dagger \hat{a}_i - \hbar g (\hat{a}_A \hat{a}_B^\dagger + \hat{a}_A^\dagger \hat{a}_B) \quad (\text{A.3})$$

with coupling strength $g = Gm/\omega L^3$. A general biparty Fock state $|\psi_0\rangle = |kl\rangle$ with $k, l \in \mathbb{N}_0$ can be evolved in time under this hamiltonian, treating the gravitational interaction $H_G = -\hbar g(\hat{a}_1 \hat{a}_2^\dagger + \hat{a}_1^\dagger \hat{a}_2)$ as a perturbation. The resulting state $|\psi(t)\rangle$ after some time t is in the most general form given as

$$|\psi(t)\rangle = \sum_{i,j \geq 0} c_{i,j}(t) |i, j\rangle \quad (\text{A.4})$$

where the coefficients $c_{i,j}(t)$ are given by first order perturbation theory as

$$c_{i,j}(t) = c_{i,j}(t=0) - \frac{i}{\hbar} \int_0^t dt' \langle ij | \hat{H}_G | kl \rangle e^{-i(E_{kl} - E_{ij})t'/\hbar}. \quad (\text{A.5})$$

The exponent is given by the energy of the appropriate Fock states $E_{kl} - E_{ij} = \hbar\omega(k + l - (i + j))$ and the matrix element in the integrand can be calculated to

$$\langle ij | \hat{H}_G | kl \rangle = \begin{cases} -\hbar g & \text{if } i = k \pm 1 \text{ and } j = l \mp 1 \\ 0 & \text{otherwise} \end{cases}. \quad (\text{A.6})$$

The coefficients for $t = 0$ are trivially given from the initial state as

$$c_{i,j}(t = 0) = \begin{cases} 1 & \text{for } i, j = k, l \\ 0 & \text{otherwise} \end{cases}. \quad (\text{A.7})$$

For the non-zero states the energies in the exponent equate to zero and the evolved state is given by (up to a normalization)

$$|\psi(t)\rangle = |kl\rangle -igt|k-1, l+1\rangle -igt|k+1, l-1\rangle + \mathcal{O}(g^2). \quad (\text{A.8})$$

For $k = 1$ and $l = 0$, the evolved state is in the form (with normalization \mathcal{N})

$$|\psi(t)\rangle = \mathcal{N}(|10\rangle -igt|01\rangle + \mathcal{O}(g^2)) \quad (\text{A.9})$$

which is entangled with logarithmic negativity $E_N(|\psi(t)\rangle\langle\psi(t)|) \simeq 2tg/\log 2 + \mathcal{O}(g^2) \geq 0$.

A.2 Exemplary calculation of E_N

In this section, the logarithmic negativity E_N eq. (2.15) is exemplary calculated for the state eq. (2.7). The density matrix of this system is given by

$$\rho(t) = |\psi(t)\rangle\langle\psi(t)| = \frac{1}{4} \begin{pmatrix} 1 & e^{i\Delta\phi} & e^{i\Delta\phi} & 1 \\ e^{-i\Delta\phi} & 1 & 1 & e^{-i\Delta\phi} \\ e^{-i\Delta\phi} & 1 & 1 & e^{-i\Delta\phi} \\ 1 & e^{i\Delta\phi} & e^{i\Delta\phi} & 1 \end{pmatrix}. \quad (\text{A.10})$$

Consequently, the partially transposed density ρ^{Γ_B} is given by

$$\rho^{\Gamma_B}(t) = \frac{1}{4} \begin{pmatrix} 1 & e^{-i\Delta\phi} & e^{i\Delta\phi} & 1 \\ e^{i\Delta\phi} & 1 & 1 & e^{-i\Delta\phi} \\ e^{-i\Delta\phi} & 1 & 1 & e^{i\Delta\phi} \\ 1 & e^{i\Delta\phi} & e^{-i\Delta\phi} & 1 \end{pmatrix}. \quad (\text{A.11})$$

The eigenvalues were calculated using **Mathematica** and equate to

$$\left\{ \sin^2\left(\frac{\Delta\phi}{2}\right), \cos^2\left(\frac{\Delta\phi}{2}\right), \frac{\sin\Delta\phi}{2}, -\frac{\sin\Delta\phi}{2} \right\}$$

According to lemma 2.1, $\|\rho^{\Gamma_B}\|_1$ is given by the sum of the absolute eigenvalues, which is equal to $1 + |\sin\Delta\phi|$. The negativity as the absolute sum of all negative eigenvalues (demonstrated in proposition 2.2) equates to $\mathcal{N} = |\sin\Delta\phi|/2$. Both methods result in a logarithmic negativity of $E_N = \log_2(1 + |\sin\Delta\phi|)$.

A.3 Polarizability of a dielectric sphere

The polarizability α is defined via

$$\mathbf{E}_\infty \alpha = \mathbf{p}, \quad (\text{A.12})$$

where \mathbf{p} is the induced dipole moment and \mathbf{E}_∞ is the external electric field that induces the dipole moment. For a linear and uniform dielectric, it is given as $\mathbf{p} = \mathcal{V} \varepsilon_0 (\varepsilon_r - 1) \mathbf{E}_\text{in}$ [84, p. 220-226]. Here, \mathcal{V} is the volume of the object and \mathbf{E}_in is the electric field inside the dielectric. The electrostatic boundary conditions for the problem are given by

$$V_\text{in}|_{r=R} = V_\text{out}|_{r=R} \quad \text{and} \quad \varepsilon_r \varepsilon_0 \frac{\partial V_\text{in}}{\partial r} \Big|_{r=R} = \varepsilon_0 \frac{\partial V_\text{out}}{\partial r} \Big|_{r=R} \quad (\text{A.13})$$

and the electric potential outside of the sphere at $r \rightarrow \infty$ should be equal to the external dipole-inducing field $V_\text{out}|_{r \rightarrow \infty} = -\mathbf{E}_\infty \cdot \mathbf{r} = -E_\infty r \cos \theta$. The electric potential inside and outside the sphere can be calculated using the spherical decomposition of the general electric potential $V \propto 1/|\mathbf{r} - \mathbf{r}'|$ into Legendre Polynomials P_l [84, p. 188-190]:

$$V_\text{in}(r, \theta) = -E_\infty r \cos \theta + \sum_{l=0}^{\infty} A_l r^l P_l(\cos \theta), \quad (\text{A.14})$$

$$V_\text{out}(r, \theta) = -E_\infty r \cos \theta + \sum_{l=0}^{\infty} \frac{B_l}{r^{l+1}} P_l(\cos \theta). \quad (\text{A.15})$$

Applying both boundary conditions, it follows that [84, p. 249-251]

$$\begin{cases} A_l = B_l = 0 & \text{for } l \neq 1, \\ A_1 = -\frac{3}{\varepsilon_r + 2} E_\infty, \quad B_1 = \frac{\varepsilon_r - 1}{\varepsilon_r + 2} R^3 E_\infty \end{cases} \quad (\text{A.16})$$

and the resulting homogenous electric field $\mathbf{E}_\text{in} = -\nabla V_\text{in}$ inside the sphere is given as

$$\mathbf{E}_\text{in} = \frac{3}{\varepsilon_r + 2} \mathbf{E}_\infty. \quad (\text{A.17})$$

The field is shown on the right in ?? .The polarizability α of the sphere can be now be determined to

$$\alpha_\text{sphere} = 4\pi \varepsilon_0 R^3 \left(\frac{\varepsilon_r - 1}{\varepsilon_r + 2} \right). \quad (\text{A.18})$$

Depending on the definition, sometimes the factor $4\pi \varepsilon_r$ is dropped.

A.4 Blocking of the shield

Assume two spheres A and B with charge q_A and q_B separated by a distance $2L$ on the x -axis. A circular shield is placed perfectly in the center of the spheres orthogonal to

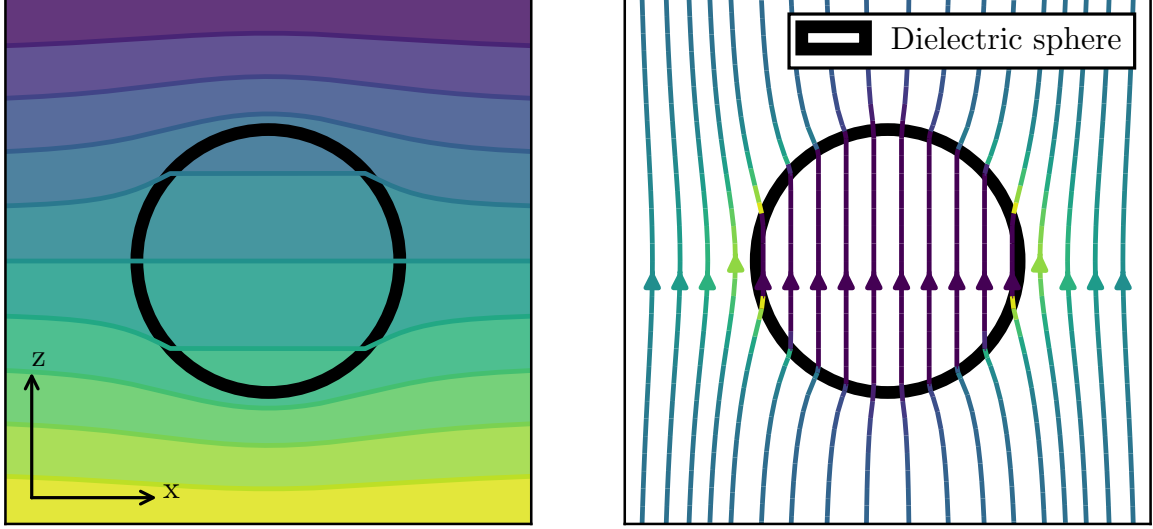


Figure A.1: **left:** Electric potential V of a dielectric sphere in an external electric field $\mathbf{E}_\infty \parallel \mathbf{e}_z$. **right:** The corresponding electric field lines inside and outside the dielectric sphere.

the direct connection between them. The magnitude of the field at a distance z in the direction \mathbf{e}_x from this connection line is given by

$$E_x(z) = \frac{L(q_A - q_B)}{4\pi\epsilon_0(L^2 + z^2)^{3/2}} \quad (\text{A.19})$$

The total flux the circular shield with radius r_s is given by

$$\Phi = \int_0^{r_s} dz \int_0^{2\pi} d\varphi E_x(z) = \frac{(q_A - q_B)}{2\epsilon_0} \left[1 - \frac{L}{\sqrt{L^2 + r_s^2}} \right]. \quad (\text{A.20})$$

Comparing the total flux for $r_s \rightarrow \infty$ with the flux through the shield, one can arrive at the charge-independent **effectiveness** η of the shield as

$$\eta = \frac{\Phi}{\Phi_\infty} = 1 - \frac{L}{\sqrt{L^2 + r_s^2}} \quad (\text{A.21})$$

and thus a shield with radius

$$r_s = L \sqrt{\frac{1 - (1 - \eta)^2}{(1 - \eta)^2}} \quad (\text{A.22})$$

will block a fraction η of the total field.

A.5 Thermal harmonic oscillator

The amplitude z of a single vibrational shield-mode (k, l) with frequency $\omega_{kl} \equiv \omega$ behaves like a quantum harmonic oscillator. The average amplitude $\langle z \rangle_n = 0$. The variance $(\Delta z)^2 = \langle z^2 \rangle - \langle z \rangle^2$ however is given by

$$(\Delta z)_n^2 = \langle z^2 \rangle_n = \frac{\hbar}{2m\omega}(1 + 2n). \quad (\text{A.23})$$

At a temperature T , the occupation of the modes is described by the boltzmann distribution:

$$\langle z^2 \rangle_T = \sum_{n=0}^{\infty} \frac{1}{Z} e^{-\beta E_n} \langle z^2 \rangle_n, \quad (\text{A.24})$$

where $\beta = 1/k_B T$, $E_n = \hbar\omega(n + 1/2)$ is the energy of mode n and

$$Z = \sum_{n=0}^{\infty} e^{-\beta E_n} = \frac{e^{-\beta \frac{\hbar\omega}{2}}}{1 - e^{-\beta \hbar\omega}} \quad (\text{A.25})$$

is the partition function. Using known series, the expression eq. (A.24) can be evaluated to

$$(\Delta z)_T^2 = \langle z^2 \rangle_T = \frac{\hbar}{2m\omega} \sum_{n=0}^{\infty} \frac{1}{Z} [e^{-\beta E_n} + 2ne^{-\beta E_n}] \quad (\text{A.26})$$

$$= \frac{\hbar}{2m\omega} \left[1 + \frac{2}{Z} \sum_{n=0}^{\infty} n e^{-\beta E_n} \right] \quad (\text{A.27})$$

$$= \frac{\hbar}{2m\omega} \left[1 + \frac{2e^{-\beta \hbar\omega}}{1 - e^{-\beta \hbar\omega}} \right] = \frac{\hbar}{2m\omega} \coth\left(\frac{\hbar\omega}{2k_B T}\right) \quad (\text{A.28})$$

B Primary calculations

B.1 Entanglement in different orientations

Expanding the separations $1/L^{(ij)}$ between the states $|\psi_A^{(i)}\rangle$ and $|\psi_B^{(j)}\rangle$ in second order in Δx and calculating the dynamic phases, the following represents the time-evolved state:

$$\rho_{\text{Phase}} = \frac{1}{4} \begin{pmatrix} 1 & e^{i(\phi_B + \phi_{AB})} & e^{-i(\phi_A - \phi_{AB})} & e^{-i(\phi_A - \phi_B)} \\ & 1 & e^{-i(\phi_A + \phi_B)} & e^{-i(\phi_A + \phi_{AB})} \\ & \text{c.c} & 1 & e^{i(\phi_B - \phi_{AB})} \\ & & & 1 \end{pmatrix} \quad (\text{B.1})$$

with the substitutions

$$\phi_A = g_{\text{Grav}} \frac{\Delta x_A \sin \alpha}{4L^2}, \quad \phi_B = g_{\text{Grav}} \frac{\Delta x_B \sin \beta}{4L^2}, \quad (\text{B.2})$$

$$\phi_{AB} = g_{\text{Grav}} \frac{\Delta x_A \Delta x_B}{8L^3} \left(\frac{1}{2} \cos \alpha \cos \beta - \sin \alpha \sin \beta \right) \quad (\text{B.3})$$

and the gravitational coupling strength

$$g_{\text{Grav}} = \frac{GM_A M_B t}{\hbar}. \quad (\text{B.4})$$

Eigenvalues of ρ^Γ are

$$\left\{ \sin^2 \left(\frac{\phi_{AB}}{2} \right), \cos^2 \left(\frac{\phi_{AB}}{2} \right), \frac{\sin(\phi_{AB})}{2}, -\frac{\sin(\phi_{AB})}{2} \right\} \quad (\text{B.5})$$

and thus the logarithmic negativity is given by the sum of negative eigenvalues as

$$E_N = \log_2 \left\{ 1 + \left| \sin \left(\frac{GM_A M_B \Delta x_A \Delta x_B t}{8\hbar L^3} \left[\sin \alpha \sin \beta - \frac{1}{2} \cos \alpha \cos \beta \right] \right) \right| \right\}. \quad (\text{B.6})$$

Due to Casimir interactions between the particles and the shield, in first order only the additional term ($\delta = \alpha, \beta$)

$$\phi_{\text{Cas., A(B)}} = \frac{c\pi^3}{720} \left(\frac{\varepsilon_r - 1}{\varepsilon_r + 1} \right) \varphi(\varepsilon_r) R \frac{2\Delta x_{A(B)} \sin \delta}{(L - R - d/2)^3} t \quad (\text{B.7})$$

is added to the phase $\phi_{A(B)}$, leaving the resulting logarithmic negativity unchanged.

B.2 Density matrix with stochastic placement variations

Expanding the separations $1/(\mathcal{L}_{A(B)}^{(i)})^2$ for the PFA from eq. (4.7) in first order in $\theta_{A(B)}$ and $L_{A(B)}$ (here exemplary for mass $A^{(1)}$):

$$\begin{aligned} \frac{1}{(\mathcal{L}_A^{(1)})^2} &\approx \frac{4}{(d-2L+2R)^2} + \frac{8\Delta x_{A(B)} \sin \delta}{(d-2L+2R)^3} + \theta_{A(B)} \left(\frac{8\Delta x_{A(B)} \cos \delta}{(d-2L+2R)^3} \right) \\ &+ L_{A(B)} \left(\frac{16}{(d-2L+2R)^3} + \frac{48\Delta x_{A(B)} \sin \delta}{(d-2L+2R)^4} \right) + \theta_{A(B)} L_{A(B)} \frac{48\Delta x_{A(B)} \cos \delta}{(d-2L+2R)^4} \quad (\text{B.8}) \end{aligned}$$

Similar results can be obtained for expanding the gravitational couplings $1/L^{(ij)}$ from eq. (4.10):

$$\begin{aligned} \frac{1}{L^{(11)}} &\approx \frac{1}{2L} + \frac{\Delta x_B \sin \beta - \Delta x_A \sin \alpha}{8L^2} - \theta_A \frac{\Delta x_A \cos \alpha}{8L^2} + \theta_B \frac{\Delta x_B \cos \beta}{8L^2} \\ &+ L_A \left(-\frac{1}{4L^2} + \frac{\Delta x_A \sin \alpha - \Delta x_B \sin \beta}{8L^3} \right) + L_B \left(-\frac{1}{4L^2} + \frac{\Delta x_A \sin \alpha - \Delta x_B \sin \beta}{8L^3} \right) \\ &+ L_A \theta_A \frac{\Delta x_A \cos \alpha}{8L^3} - L_A \theta_B \frac{\Delta x_B \cos \beta}{8L^3} + L_B \theta_A \frac{\Delta x_A \cos \alpha}{8L^3} - L_B \theta_B \frac{\Delta x_B \cos \beta}{8L^3} \\ &+ L_A L_B \left(\frac{2}{4L^3} + \frac{3\Delta x_B \sin \beta - 3\Delta x_A \sin \alpha}{16L^4} \right) \\ &- L_A L_B \theta_A \frac{3\Delta x_A \cos \alpha}{16L^4} + L_A L_B \theta_B \frac{3\Delta x_B \cos \beta}{16L^4} \quad (\text{B.9}) \end{aligned}$$

The resulting average over $\theta_{A(B)}$ and $L_{A(B)}$ can be computed by

$$\int_{-\infty}^{\infty} d\theta_A d\theta_B dL_A dL_B p(\theta_A) p(\theta_B) p(L_A) p(L_B) e^{i\phi} \quad (\text{B.10})$$

where $p(\cdot)$ is a gaussian probability distribution in the form of

$$p(x) = \frac{1}{\sqrt{2\pi}\Delta x} e^{-\frac{x^2}{2(\Delta x)^2}} \quad (\text{B.11})$$

and ϕ is the accumulated dynamic phase dependent on the two series expansions above. The mixed terms consisting of combinations of θ and L can be neglected in first order because in the final result, they appear in the form of (notation: $\Delta A, \Delta B$ for either $\Delta\theta$ or ΔL ; a, b are constants)

$$\sim \exp \left\{ -\frac{a^2(\Delta A)^2}{2b^2(\Delta A)^2(\Delta B)^2 + 2} \right\} \xrightarrow{\Delta A, \Delta B \ll 1} 1. \quad (\text{B.12})$$

Each averaged element of the density matrix can therefore be analytically calculated using

$$\prod_{\Delta A = \{\Delta\theta_{A(B)}, \Delta L_{A(B)}\}_{-\infty}^{\infty}} \int dA \frac{1}{\sqrt{2\pi}\Delta A} e^{-\frac{A^2}{2(\Delta A)^2}} e^{i\xi A} e^{i\phi} = \prod_{\Delta A} e^{-\frac{\xi^2(\Delta A)^2}{2}} e^{i\phi}. \quad (\text{B.13})$$

The resulting averaged density matrices are given by the following for variations in the angle:

$$\langle \rho_\theta \rangle = \begin{pmatrix} 1 & e^{-\xi_B^2 \frac{(\Delta\theta_B)^2}{2} t^2} & e^{-\xi_A^2 \frac{(\Delta\theta_A)^2}{2} t^2} & e^{-\xi_A^2 \frac{(\Delta\theta_A)^2}{2} t^2} e^{-\xi_B^2 \frac{(\Delta\theta_B)^2}{2} t^2} \\ & 1 & e^{-\xi_A^2 \frac{(\Delta\theta_A)^2}{2} t^2} e^{-\xi_B^2 \frac{(\Delta\theta_B)^2}{2} t^2} & e^{-\xi_A^2 \frac{(\Delta\theta_A)^2}{2} t^2} \\ & & 1 & e^{-\xi_B^2 \frac{(\Delta\theta_B)^2}{2} t^2} \\ \text{c.c} & & & 1 \end{pmatrix} \quad (\text{B.14})$$

with the abbreviations ($\delta = \alpha, \beta$)

$$\xi_{A(B)} = \left(\frac{c\pi^3}{720} \left(\frac{\varepsilon_r - 1}{\varepsilon_r + 1} \right) \varphi(\varepsilon_r) R \frac{2\Delta x_{A(B)} \cos \delta}{(L - R - d/2)^3} + \frac{GM_A M_B}{\hbar} \frac{\Delta x_{A(B)} \cos \delta}{4L^2} \right) \quad (\text{B.15})$$

Similar results for variations in the particle-shield separation L can be obtained:

$$\langle \rho_L \rangle = \begin{pmatrix} 1 & e^{-\chi_B^2 \frac{(\Delta L_A)^2}{2} t^2} e^{-(\zeta_B + \chi_B)^2 \frac{(\Delta L_B)^2}{2} t^2} & e^{-(\zeta_A + \chi_A)^2 \frac{(\Delta L_A)^2}{2} t^2} e^{-\chi_A^2 \frac{(\Delta L_B)^2}{2} t^2} & \dots \\ & 1 & e^{-(\chi_A + \zeta_A)^2 \frac{(\Delta L_A)^2}{2} t^2} e^{-(\chi_B + \zeta_B)^2 \frac{(\Delta L_B)^2}{2} t^2} & \dots \\ & & 1 & \dots \\ \text{c.c} & & & \dots \\ & \dots & e^{-(\chi_A + \zeta_A)^2 \frac{(\Delta L_A)^2}{2} t^2} e^{-(\chi_B + \zeta_B)^2 \frac{(\Delta L_B)^2}{2} t^2} & \dots \\ & \dots & e^{-(\zeta_A + \chi_A)^2 \frac{(\Delta L_A)^2}{2} t^2} e^{-\chi_A^2 \frac{(\Delta L_B)^2}{2} t^2} & \dots \\ & \dots & e^{-\chi_B^2 \frac{(\Delta L_A)^2}{2} t^2} e^{-(\zeta_B + \chi_B)^2 \frac{(\Delta L_B)^2}{2} t^2} & \dots \\ & & 1 & \dots \end{pmatrix} \quad (\text{B.16})$$

with

$$\chi_{A(B)} = \frac{GM_A M_B}{\hbar} \frac{\Delta x_{A(B)} \sin \delta}{4L^3} \quad (\text{B.17})$$

$$\zeta_{A(B)} = \frac{c\pi^3}{720} \left(\frac{\varepsilon_r - 1}{\varepsilon_r + 1} \right) \varphi(\varepsilon_r) R \frac{6\Delta x_{A(B)} \sin \delta}{(L - R - d/s)^4} \quad (\text{B.18})$$

The combined mean density matrix is therefore given by

$$\langle \rho \rangle = \rho_{\text{Phase}} \odot \langle \rho_\theta \rangle \odot \langle \rho_L \rangle \quad (\text{B.19})$$

where the symbol \odot represents the element-wise matrix product (Hadamard product). In the special case where $\Delta\theta_A = \Delta\theta_B$ and $\Delta L_A = \Delta L_B$ as well as where both particles are identical, i.e. $\Delta x_A = \Delta x_B$ and $M_A = M_B$ and $\alpha = \pm\beta$, the logarithmic negativity can be obtained analytically. Using the approximation $\chi_{A(B)} \ll \zeta_{A(B)}$, which is justified for all separations $R < L \lesssim 9.7 \text{ m}$.

$$\langle \rho \rangle = \rho_{\text{Phases}} \odot \begin{pmatrix} 1 & e^{-\gamma} & e^{-\gamma} & e^{-2\gamma} \\ & 1 & e^{-2\gamma} & e^{-\gamma} \\ & & 1 & e^{-\gamma} \\ \text{c.c} & & & 1 \end{pmatrix} \quad (\text{B.20})$$

with

$$\gamma = \left(\xi^2 \frac{(\Delta\theta)^2}{2} + \zeta^2 \frac{(\Delta L)^2}{2} \right) t^2 \quad (\text{B.21})$$

The logarithmic negativity is given by (ϕ_{AB} from eq. (B.3))

$$E_N = \max \left\{ 0, \log_2 \left(e^{-\gamma} (\cosh \gamma + |\sin \phi_{AB}|) \right) \right\} \quad (\text{B.22})$$

$$= \log_2 \left\{ \frac{1}{2} e^{-\gamma} (|\sin \phi_{AB} - \sinh \gamma| + |\sin \phi_{AB} + \sinh \gamma| + 2 \cosh \gamma) \right\}. \quad (\text{B.23})$$

For general combinations of $\Delta L_A, \Delta L_B, \Delta\theta_A, \Delta\theta_B$ and for results without any approximations, the logarithmic negativity was computed numerically.

B.3 Density matrix for particles in front a vibrating plate

The separations between the shield and the Particle state $A(B)_i$ in the parallel configuration are given by

$$d_{A(B)}^i = L \pm_{A(B)} z \left(|u| \mp_i |\nabla u| \frac{\Delta x}{2} \right) \quad (\text{B.24})$$

where the first \pm distinguishes between particle A and B and the second one between $i = 1$ and $i = 2$. The gravitational interaction is given as before in chapter 2. After averaging over z (normally distributed around $\langle z \rangle = 0$ and std. Δz) the resulting density matrix is now given by

$$\langle \rho \rangle = \frac{1}{4} \begin{pmatrix} 1 & e^{i\Delta\phi} e^{-\frac{1}{2}(\xi_{\text{Cas}})^2(\Delta z)^2} & e^{i\Delta\phi} e^{-\frac{1}{2}(\xi_{\text{Cas}})^2(\Delta z)^2} & 1 \\ & 1 & e^{-\frac{1}{2}(2\xi_{\text{Cas}})^2(\Delta z)^2} & e^{-i\Delta\phi} e^{-\frac{1}{2}(\xi_{\text{Cas}})^2(\Delta z)^2} \\ & & 1 & e^{-i\Delta\phi} e^{-\frac{1}{2}(\xi_{\text{Cas}})^2(\Delta z)^2} \\ \text{c.c} & & & 1 \end{pmatrix} \quad (\text{B.25})$$

with

$$\Delta\phi = \frac{GM_A M_B}{\hbar} \left(\frac{1}{4L^2} - \frac{1}{\sqrt{2L + (\Delta x)^2}} \right) t \quad (\text{B.26})$$

$$\xi_{\text{Cas}} = \begin{cases} \frac{c\pi^3 R}{720} \left(\frac{\varepsilon_r - 1}{\varepsilon_r + 1} \right) \varphi(\varepsilon_r) \cdot \frac{2|\nabla u| \Delta x}{L^3} t & \text{in the PFA for } L/R \approx 1 \\ \frac{3cR^3}{8\pi} \left(\frac{\varepsilon_r - 1}{\varepsilon_r + 2} \right) \frac{4|\nabla u| \Delta x}{L^5} t & \text{in the LSL for } L/R \gg 1 \end{cases} \quad (\text{B.27})$$

which is only dependent on the gradient of the shape $|\nabla u|$. The logarithmic negativity is given by

$$E_N(\langle \rho \rangle) = \log_2 \left\{ \frac{1}{4} \left(3 + e^{-4\gamma} + \sqrt{(1 - e^{-4\gamma})^2 + 16e^{-2\gamma} \sin^2 \Delta\phi} \right) \right\} \quad (\text{B.28})$$

with

$$\gamma = \frac{1}{2} (\xi_{\text{Cas}})^2 (\Delta z)^2. \quad (\text{B.29})$$

It follows, that for large γ and thus $(\Delta z)_{\text{crit}} \sim 1/\xi_{\text{Cas}}$, no entanglement is observable.

B.4 Time evolution of two particles in front of a thermal plate

The time evolution operator $\hat{U} = e^{-i\hat{H}t/\hbar}$ of the hamiltonian eq. (5.29) can be calculated in the interaction picture using the “Magnus expansion” [85]. In the following calculations, the direct gravitational interactions between the two particles are ignored as they don’t depend on the shield vibrations at all. The final evolution due to these couplings were already studied in chapter 4 and can just be added in the end. The interaction picture hamiltonian in the $\{|\psi_A^1\psi_B^1\rangle, |\psi_A^1\psi_B^2\rangle, |\psi_A^2\psi_B^1\rangle, |\psi_A^2\psi_B^2\rangle\}$ -basis is given by

$$\hat{H}_{\text{int}} = \sum_{m \in \{(k,l)\}} \begin{pmatrix} g_{A,m}^1 + g_{B,m}^1 & & & \\ & g_{A,m}^1 + g_{B,m}^2 & & \\ & & g_{A,m}^2 + g_{B,m}^1 & \\ & & & g_{A,m}^2 + g_{B,m}^2 \end{pmatrix} (\hat{a}e^{-i\omega_m t} + \hat{a}^\dagger e^{i\omega_m t}) \quad (\text{B.30})$$

The operator at the beginning is referred to as \hat{G} in the following. The time evolution in the Magnus expansion here given by [85]

$$\hat{U}(t) = \exp\left\{-\frac{i}{\hbar} \int_0^t dt_1 \hat{H}_{\text{int}}(t) - \frac{1}{2\hbar^2} \int_0^t dt_1 \int_0^{t_1} dt_2 [\hat{H}_{\text{int}}(t_1), \hat{H}_{\text{int}}(t_2)]\right\}. \quad (\text{B.31})$$

All higher order terms vanish, so this is an exact result. After substitution, the result is given by

$$\hat{U}(t) = \exp\left\{\hat{G}(f_1 \hat{a}^\dagger - f_1^* \hat{a}) + i\hat{G}^2 f_2\right\} \quad (\text{B.32})$$

$$= \hat{D}\left(f_1(g_{A,m}^1 + g_{B,m}^1)\right) \exp\left\{if_2(g_{A,m}^1 + g_{B,m}^1)^2\right\} |\psi_A^1\psi_B^1\rangle\langle\psi_A^1\psi_B^1| + \dots \quad (\text{B.33})$$

with

$$f_1 = \frac{(1 - e^{i\omega_m t})}{\hbar\omega_m} \quad \text{and} \quad f_2 = \frac{t\omega_m - \sin(t\omega_m)}{\hbar^2\omega_m^2} \quad (\text{B.34})$$

and the displacement operator $\hat{D}(\alpha) = \exp\{\alpha\hat{a}^\dagger - \alpha^*\hat{a}\}$. The evolved state $\rho(t) = \hat{U}(t)\rho_0\hat{U}^\dagger(t)$ is now given by

$$\begin{aligned} \rho(t) = & \bigotimes_{m \in \{(k,l)\}} \hat{D}\left(f_1(g_A^1 + g_B^1)\right) \rho_{\text{th},m} \hat{D}^\dagger\left(f_1(g_A^1 + g_B^1)\right) \otimes \frac{1}{4} |\psi_A^1\psi_B^1\rangle\langle\psi_A^1\psi_B^1| \\ & + \hat{D}\left(f_1(g_A^1 + g_B^1)\right) \rho_{\text{th},m} \hat{D}^\dagger\left(f_1(g_A^1 + g_B^2)\right) \otimes \frac{1}{4} e^{if_2(g_A^1 + g_B^1)^2} |\psi_A^1\psi_B^1\rangle\langle\psi_A^1\psi_B^2| e^{-if_2(g_A^1 + g_B^2)^2} \\ & + \dots \\ & + \hat{D}\left(f_1(g_A^2 + g_B^2)\right) \rho_{\text{th},m} \hat{D}^\dagger\left(f_1(g_A^2 + g_B^1)\right) \otimes \frac{1}{4} e^{if_2(g_A^2 + g_B^2)^2} |\psi_A^2\psi_B^2\rangle\langle\psi_A^2\psi_B^1| e^{-if_2(g_A^2 + g_B^1)^2} \\ & + \hat{D}\left(f_1(g_A^2 + g_B^2)\right) \rho_{\text{th},m} \hat{D}^\dagger\left(f_1(g_A^2 + g_B^2)\right) \otimes \frac{1}{4} |\psi_A^2\psi_B^2\rangle\langle\psi_A^2\psi_B^2| \end{aligned} \quad (\text{B.35})$$

B Primary calculations

We are interested in the evolution of the two-particle system. This is given by tracing out the thermal shield $\rho_{\text{sys.}} = \text{tr}_{\text{th}} \{\rho(t)\}$. Using $\text{tr}\{A \otimes B\} = \text{tr}\{A\} \text{tr}\{B\}$, it follows:

$$\rho_{\text{sys.}} = \frac{1}{4} \begin{pmatrix} 1 & \Pi_m \text{tr} \left\{ \hat{D}(f_1(g_A^1 + g_B^1)) \rho_{\text{th},m} \hat{D}^\dagger(f_1(g_A^1 + g_B^2)) \right\} e^{if_2((g_A^1 + g_B^1)^2 - (g_A^1 + g_B^2)^2)} & \dots \\ \vdots & \ddots & \end{pmatrix} \quad (\text{B.36})$$

To calculate $\text{tr}\{\hat{D}(\zeta_i) \rho_{\text{th}} \hat{D}^\dagger(\zeta_j)\}$, we expand ρ_{th} into coherent states [75]

$$\rho_{\text{th}} = \int d\alpha^2 \frac{1}{\bar{n}\pi} e^{-\frac{|\alpha|^2}{\bar{n}}} |\alpha\rangle\langle\alpha| \quad (\text{B.37})$$

and calculate the required trace [75]:

$$\text{tr}\{\hat{D}(\zeta_i) \rho_{\text{th}} \hat{D}^\dagger(\zeta_j)\} = \exp\left\{ \phi - |\Delta\zeta|^2 \left(\frac{1}{2} + \bar{n} \right) \right\} \quad (\text{B.38})$$

where $\Delta\zeta = \zeta_i - \zeta_j$ and $\phi = (\zeta_j^* \zeta_i - \zeta_j \zeta_i^*)/2 = 0$. The final decoherence elements of the evolved state therefore all have the form

$$e^{-\gamma_{1,2}} = \exp\left\{ - \sum_m \left| (g_{A,m}^1 + g_{B,m}^1) - (g_{A,m}^1 + g_{B,m}^2) \right|^2 f_1 f_1^* \left(\frac{1}{2} + \bar{n}_m \right) \right\} \quad (\text{B.39})$$

C Additional figures

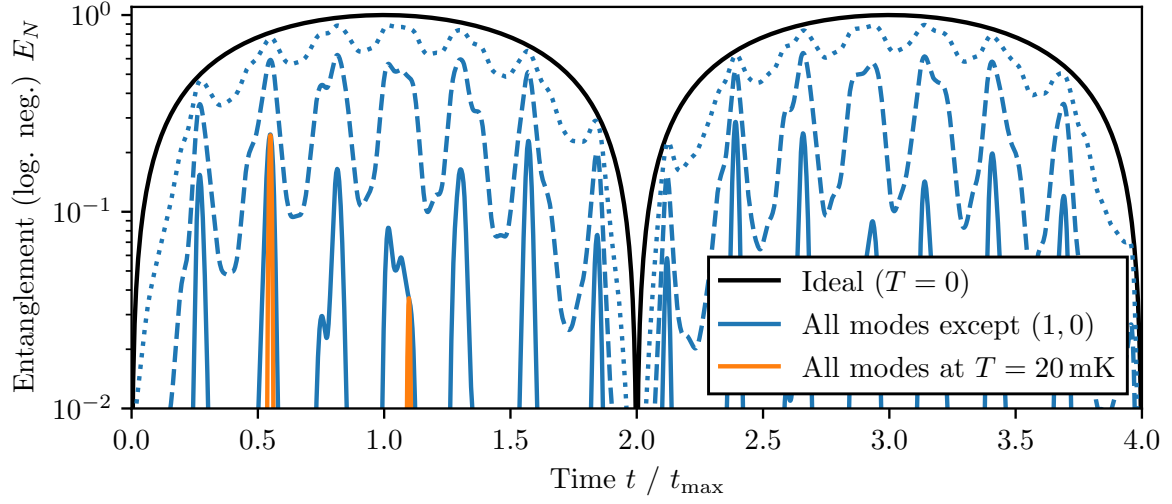


Figure C.1: Similar to fig. 5.7 at $T = 20$ mK for a smaller shield with $r_s = 5$ mm at a separation of $L = 2R = 20 \mu\text{m}$, where the particle is placed at the worst-case position in front of the shield, where the effects of the mode $(1, 0)$ are maximized.

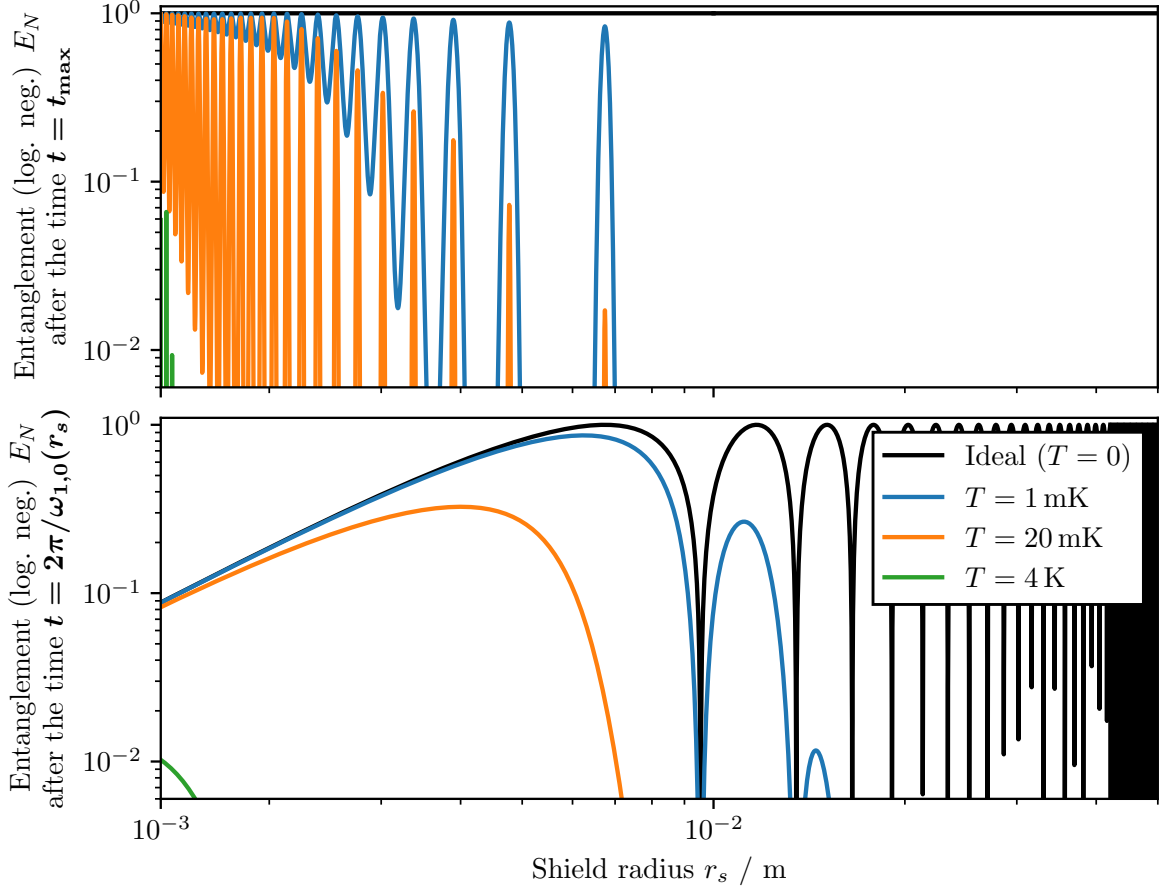


Figure C.2: Generated entanglement after **(top)** a time $t_{\max} = 258$ ms and after **(bottom)** a time $2\pi/\omega_{1,0}(r_s)$ for different shield radii r_s . The plotted concept is similar to fig. 5.8. A smaller shield Parameters from table 4.1 were taken. The artifacts at around $r_s \approx 5 \times 10^{-2}$ m in the bottom figure are due to numeric instabilities.